NUMERICAL SIMULATION BASED ANALYSIS OF ROAD VEHICLE AERODYNAMIC FLOWS

by

Chunhui Zhang

A dissertation submitted to the faculty of
The University of North Carolina at Charlotte
in partial fulfillment of the requirements
for the degree of Doctor of Philosophy in
Mechanical Engineering

Charlotte

2018

Approved by:

_____
Dr. Mesbah Uddin

_____
Dr. Peter Tkacik

_____
Dr. Saiful Bari

_____
Dr. Babak Parkhideh

_____
Dr. Harrison Campbell

ABSTRACT

CHUNHUI ZHANG. Numerical Simulation Based Analysis of Road Vehicle Aerodynamic Flows. (Under the direction of DR. MESBAH UDDIN)

Computational Fluid Dynamics (CFD) is currently viewed as one of the major tools for investigating aerodynamics of road vehicles. In spite of its well-documented limitations in predicting flows involving complex geometries and flow separations, the RANS (Reynolds Averaged Navier-Stokes) approach is still a widely used turbulence modeling methodology in motorsports/automotive industries due to its cost-effectiveness and fast turnaround time. In the past, automotive research and development efforts showed an intensive focus on the external vehicle aerodynamics for improved parasitic drag efficiency. However, as the opportunities of attaining aerodynamic advantage by pure manipulation vehicle?s external body-shape diminish, the industry turns to other areas of the vehicle for further aerodynamic efficiency improvement. One such area is the underhood airflow management, which is challenging for both experimental and analytical approaches due to the complexity and compactness of modern vehicle underhood compartments. Thereby, 3D CFD analyses appear to be a cost-effective alternative to investigate the underhood airflow characteristics during a vehicle's early design stage. Subsequently, one aspect of this thesis involves computational studies using the RANS approach to investigate the role of underhood airflow features on the radiator performance and cooling drag. Additionally, analysis of the impact of the front grille opening size and underhood passive aerodynamic devices on the cooling drag and radiator performance are presented. All of these simulations are based on full vehicle CFD simulations carried out using a detailed realistic model of Hyundai Veloster. It is demonstrated that by properly managing the cooling airflow, simultaneous improvement of radiator performance and total vehicle drag reduction can be achieved.

However, existing literature suggests that, for automotive flows, RANS turbulence models often fail to capture the detailed flow features or even the integral aerodynamic quantities, and subsequently sometimes are used to assess the magnitude and direction of a trend. Moreover, even for such purposes, notable disagreements often exist between results predicted by different RANS models. Thanks to fast advances in computer technology, increasing popularity has been seen in the use of the hybrid LES/RANS (Large Eddy Simulation/Reynolds Averaged Navier-Stokes) approaches which have demonstrated the high potential of being more accurate and informative than the RANS approaches. Whilst evaluations of RANS and hybrid LES/RANS models, known as the DES (Detached Eddy Simulation), on various applications are abundant in literature, such evaluations on full-car models are rare. To further the investigations on-road vehicle aerodynamic simulation approaches, the prediction veracity of four RANS models which are widely used in industry, i.e., the realizable $k-\epsilon$, AKN $k-\epsilon$, SST $k-\omega$, and V2F models, are evaluated for a full-scale passenger vehicle with two different front-end configurations. The RANS simulated flow-fields are then compared against results from two hybrid LES/RANS approaches to highlight the predictive differences between different CFD simulation methodologies. It is found that the DES approach is superior in predicting the flow-field, but is not guaranteed to predict better correlated integral quantities. Consequently, this study explores the possibility of improving the prediction veracity of the SST $k-\omega$ model, the most promising variant of the RANS approach, by investigating the influence of a few selected model closure coefficients on the CFD predictions. This involves identifying the effect of each individual model parameter on the prediction first, and then formulating the optimized combination of the model closure coefficient values that yields the best correlation with the experiment. This procedure is applied to four different test objects: NACA 4412 airfoil at 12 degree angle of attack, the 25 and 35 degree slant angle Ahmed body, and a full-scale passenger road vehicle. Although

some closure coefficients do not influence the CFD results much, the predictions are very sensitive to the choice of certain model constants irrespective of the test object geometry. The study also shows that it is possible to formulate a combination of closure model coefficients that can produce very well correlated CFD predictions of the overall flow-field.

ACKNOWLEDGEMENTS

I would like to first thank my academic advisor, Dr. Mesbah Uddin, who guided me with patience and inspired me with creative thinking. His hard-working attitude and aspiration for academic research made me understand deeply what it takes to be successful. Dr. Uddin not only taught me how to solve challenging research problems but also helped me to think in a positive way and interact with others more properly. There was no doubt that the past five years was a long and stressful journey. However, I am grateful that I had a mentor like Mesbah, who encouraged and improved me along the way.

I would like to second thank my dissertation committee members I have had the honor to work with, Dr. Tkacik, Dr. Bari, Dr. Parkhideh and Dr. Campbell, for their dedication and commitment in high-level educations.

I'd like to thank UNC Charlotte MOSAIC Computing and URC group for providing me reliable and adequate computational resources for my researches which were often quite computationally costly.

I would also like to thank my peers and colleagues in the lab, and in the race shop, George, Brett, Chen, Sudan, Adit, Christian, Patrick, Spencer, not to name all but a few, for their companion, support, and correcting my English grammar errors. We had so much fun working together.

Finally, to my parents, whom I have spent less than one months within the past 5 years. Thank you for standing behind me for everything. I can't wait for you to come here to visit me.

TABLE OF CONTENTS

LIST OF FIGURES

LIST OF TABLES

CHAPTER 1: INTRODUCTION

Global automotive manufacturers are facing increasing challenges for road vehicle designs, due to the pressure from government regulations aiming to reduce greenhouse gas emissions and the demand from consumers for improved quality and durability without any compromise to innovative and aesthetic designs. Many of these design challenges are mainly influenced by the complex air flows over and through the vehicle, such as aerodynamic efficiency, underhood aerothermal management, soiling and water management, wind noise reduction, and cabin comfort, etc. Not too long ago, road vehicle aerodynamics were mainly investigated by road testing and wind tunnel experiments only. While the obvious advantage of road testing is that the actual vehicle is tested on an actual track, there are a number of disadvantages, e.g. only limited equipment can be mounted on board, difficulty in comparing two vehicles, measurement repeatability, and uncontrolled environments. On the other hand, the wind tunnel experiments can simulate a wide range of road conditions with highly controlled environments (see Figure 1.1). However, wind tunnel tests are very expensive and time-consuming due to the operation cost, the requirement of building prototypes, and limited capability of visualizing complex 3D flow structures for full-scale production vehicles, especially in the underhood compartment. Fortunately, thanks to the fast development in computer hardware and numerical methodology of solving governing equations for flow around complex body shapes, computational fluid dynamics (CFD) has emerged as a complementary alternative not only for road vehicle external aerodynamic applications but also for many others involving complex fluid flows and thermal phenomenon. Existing literature contains a vast amount of works related to automotive flows, however, thorough investigations of full-scale pas-

Figure 1.1: Smoke visualization in a wind tunnel testing [1].

senger vehicle external aerodynamics are rather rare due to the proprietary nature of the data. This study will present a numerical simulation based analysis of full-scale passenger road vehicle aerodynamic flows, including the underhood flows.

1.1 Underhood Airflow Management

Over the past several decades, we have seen a significant reduction in the parasitic drag of road vehicles. While the external aerodynamics aspect of this effort has been researched intensively and well understood, the underhood airflow management still requires further in-depth understanding, in spite of the fact that the rapid development in both experimental and numerical techniques has resulted in a vast number of studies involving vehicle underhood flow. The literature contains such a wide variety of works in this area that the due diligence will not be done by citing just one or two references. However, a good starting point is the vehicle aerodynamics col-

lections published annually by the Society of Automotive Engineers (SAE). Other notable references include: the doctoral dissertation of Littlewood [5], master's thesis of Sawyer [6], review papers by Altaf et al. [7] and Patten et al. [8], to cite but a few.

Several factors render the underhood airflow management of modern cars challenging. These include the presence of a number of additional heat sources, such as the supercharger or turbocharger, the requirement of heat-shielding of electronic components, enhanced interior climate control, and, most importantly, the demand for a more compact design. The prime objective of airflow and thermal management within the underhood environment is to ensure proper cooling of the engine with the least amount of power consumption and aerodynamic resistance. The cooling of the engine is mainly achieved by making sure that adequate airflow passes through the front-end module. The front-end module typically consists of a condenser, a radiator, and a fan module, and is called the CRFM for short. Some modern vehicles also have a turbocharger intercooler. However, excessive cooling airflow may increase the drag of the vehicle. Thus, the desired design of the CRFM should provide an optimum performance of the cooling system and contribute to the vehicle's parasitic drag reduction simultaneously.

The airflow through the CRFM is driven by two sources: (1) the fan suction, and (2) the ram air generated by the movement of the vehicle. These two sources usually work at different vehicle speeds. The fan suction behind the radiator is the main driving force for the airflow at low vehicle speeds. Subsequently, when the vehicle speed is below a certain threshold, the negative static pressure generated by the electric fan may exceed the positive static pressure between the front grille opening and condenser core. This may cause a portion of the hot air from the engine bay to recirculate to the plenum through the bypass channel. This undesired phenomenon is known as the underhood hot air recirculation. This hot air recirculation would be detrimental to the performance of the A/C system. Eliminating this bypass channel

could not only minimize the hot air recirculation, but also improve the underhood cooling efficiency. Existing literature contains a large number of works showing that an air-duct design could reduce the hot air recirculation significantly, c.f. Song et al. [9].

In general, there are two factors affecting the performance of the cooling system: (1) the mass flow rate through the radiator inlet, and (2) the flow distribution over the radiator inlet surface. The mass flow rate and flow distribution depend on the grille opening size, position, and the underhood resistance. The primary requirement for the underhood airflow management is to ensure sufficient airflow passing through the radiator, and, thus, make sure that the engine will not overheat. However, excessive airflow in the underhood increases the cooling drag. Therefore, the challenge of the underhood airflow management is to find the balance. As suggested by several works, front-end sealing and introduction of an air-duct are seen to be two effective ways of improving both airflow uniformity over and mass flow rate through the radiator surface [10, 11, 12]. Additionally, Saab et al. [13] suggested that reducing the front grille opening reduces both cooling and total drag.

The complexity and compactness of modern vehicle underhood compartment make the experimental and analytical approaches of optimal airflow management rather challenging. Thereby, 3D CFD analysis appears to be a cost-effective plausible alternative to investigate the underhood airflow characteristics during a vehicle's early design stage. In this study, the effects of the air-duct geometry and size of the grille opening on the radiator cooling performance and cooling drag at different operating conditions are presented in this paper using a 3D CFD approach. The investigation involves several design iterations of air-duct geometry and front grille opening. The results are assessed based on several important flow parameters associated with the cooling airflow, such as the airflow uniformity, total mass flow rate through the radiator and front grille opening, and total vehicle drag.

1.2 Computational Fluid Dynamics Challenges

One of the core challenges for CFD is how to simulate turbulence, especially for industrial flows. Turbulence is the most complicated fluid motion, which makes even its precise physical and mathematical definition difficult. Nevertheless, turbulence is commonly described as a three-dimensional, time-dependent, irregular and nonlinear flow phenomenon, which is dissipated and momentum exchanged by small-scale fluctuations. The smallest scales are called Kolmogorov microscales as defined in Equation 1.1, 1.2 and 1.3, where η is the Kolmogorov length scale, τ_η is the Kolmogorov time scale, u_η is the Kolmogorov velocity scale, ν is the kinematic viscosity and ϵ is the average rate of dissipation of turbulent kinetic energy per unit mass [14]. The smallest length scale for a typical automotive flow can be the order of 0.1 millimeters, estimated by $\eta/l \approx Re_l^{-3/4}$ where l can be taken as the vehicle length and Re_l as the free stream Reynolds number. On the other hand, turbulence extracts energy from the mean flow through large scale fluctuations. The largest length scale could be the order of the characteristic length of the object, such as the vehicle length for a typical automotive flow.

$$\eta = (\frac{\nu^3}{\epsilon})^{1/4} \tag{1.1}$$

$$\tau_\eta = (\frac{\nu}{\epsilon})^{1/2} \tag{1.2}$$

$$u_\eta = (\nu\epsilon)^{1/4} \tag{1.3}$$

The complex three dimensional motion of a fluid can be described by a system of partial differential equations (PDE) that represent mathematical statements of the conversation laws of physics, i.e. conversation of mass, momentum, and energy.

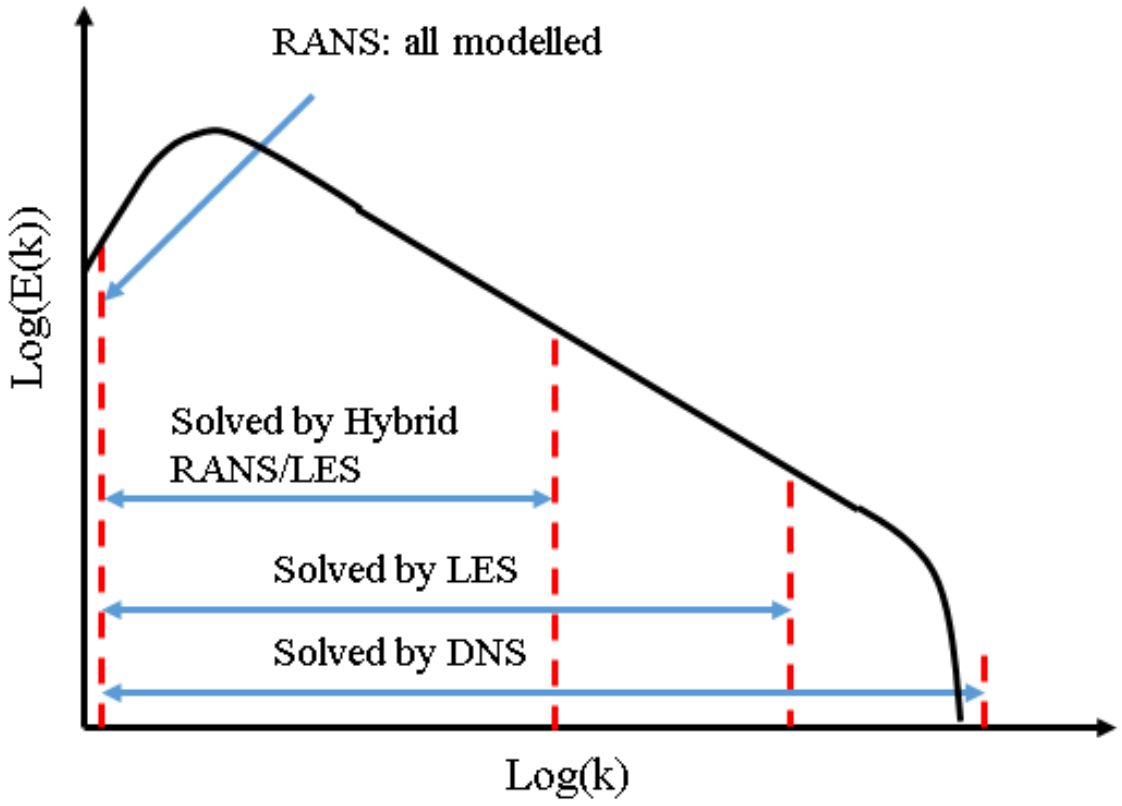

Figure 1.2: Turbulence energy spectrum, where k is the wavenumber which is the inverse of length scale and $E(k)$ is the turbulent kinetic energy. The figure has been redrawn based on [2].

Those PDEs are the governing equations for fluid dynamics, in which the mass and non-linear momentum conservation equations are called the Navier-Stokes equations. Despite their wide range of practical uses in industries and academia, it has not yet been proven that in three dimensions their solutions always exist, or that if they do exist, then they are smooth. Therefore, in industrial applications, for the modeling of turbulence based off the governing equations, physical reasoning and empirical observations are required. Depending on how the details of turbulent scales are simulated (see Figure 1.2), turbulence modeling can be categorized into four groups, i.e. Direct Numerical Simulation (DNS), Large Eddy Simulation (LES), Reynolds-Averaged Navier Stokes (RANS), and Hybrid LES/RANS.

1.2.1 The Governing Equations

Due to the scope of this study, i.e. road vehicle aerodynamics, only the governing equations that are related to automotive flows will be introduced. The road vehicle aerodynamic flows are at low Mach number, thus can be considered as incompressible (as Mach number $M < 0.3$). Further, road vehicle external aerodynamics are often conducted under isothermal conditions. Therefore, the description of energy conservation equations is excluded in this study. The governing equations of mass and momentum conservation for incompressible flow can be written as Equation 1.4 and Equation 1.5 using the Einstein notation

$$\frac{\partial u_i}{\partial x_i} = 0 \tag{1.4}$$

$$\frac{\partial u_i}{\partial t} + u_j \frac{\partial u_i}{\partial x_j} = -\frac{1}{\rho}\frac{\partial p}{\partial x_i} + \nu \frac{\partial^2 u_i}{\partial x_i \partial x_j} + f_i \tag{1.5}$$

where f_i is the vector representing all external forces.

1.2.2 Direct Numerical Simulation (DNS)

As the name implies, DNS solves the full three-dimensional, time-dependent Navier-Stokes equations numerically without any turbulence model, which means that the whole range of spatial and temporal scales of the turbulence must be resolved. As mentioned above, the smallest turbulent length and time scales are called Kolmogorov microscales and can be estimated by $\eta \sim Re_l^{-3/4}$ and $\tau_\eta \sim Re_l^{-1/2}$ respectively [15]. Therefore, the cell size in each direction of the numerical domain and the time step should decrease exponentially to the free stream Reynolds number Re_l. It is also worth mentioning that in order to maintain the numerical stability of the DNS algorithm, the time step is always smaller than the Kolmogorov micro-timescale [16]. Until the 1970's the DNS approach was impossible to be used due to the fact that com-

puter systems at that time could not meet the requirement of memory and speed to accommodate the needed resolution for the small-scale turbulent fluctuations. Even today, the applicability of DNS is limited to simple flows at low to moderate Reynolds numbers. One of the current largest scientific DNS was performed by Lee et al. [17] for turbulent channel flow at a friction Reynolds number $Re_\tau \approx 5200$. Certainly, DNS is not implementable for automotive flows. Nevertheless, DNS is still very useful for the investigation of turbulence mechanisms, the improvement, calibration, and development of turbulent models.

1.2.3 Reynolds-Averaged Navier Stokes (RANS) Models

In contrast to the DNS approach, the RANS approach models the entire turbulence spectrum as demonstrated in Figure 1.2. Due to the scope of this study, we will restrict our attention to single-phase, incompressible flow with constant laminar viscosity.

RANS equations are derived by time-averaging the governing equations for the turbulent fluid motion using a mathematical technique called the Reynolds decomposition which can separate the expectation value of a quantity from its fluctuations. For example, the instantaneous velocity u could be decomposed into its time-averaged component $\bar{u}$ and fluctuating component u' as shown in Equation 1.6.

$$u(x,y,z,t) = \overline{u(x,y,z)} + u^{'}(x,y,z,t) \tag{1.6}$$

The time-averaged mean velocity is defined as:

$$\overline{u(x,y,z)} = \lim_{t\to\infty} \frac{1}{\Delta t} \int_{t_1}^{t_1+\Delta t} u(x,y,z,t)dt \quad t_1 \leq \Delta t \leq t_2 \tag{1.7}$$

where t_1 is the time scale of the rapid fluctuations and t_2 the time scale of slow motion (time-dependent mean value).

The RANS equations thus can be derived by applying the Reynolds decomposition technique to Equations 1.4 - 1.5. The detailed mathematical process will not be

covered in this study; however, it is worth mentioning that one of the properties of the Reynolds averaging is that the mean of the fluctuating quantity is equal to zero ($\overline{u'} = 0$). Thus,

$$\frac{\partial \bar{u_i}}{\partial x_i} = 0 \tag{1.8}$$

$$\frac{\partial \bar{u_i}}{\partial t} + \bar{u_j}\frac{\partial \bar{u_i}}{\partial x_j} + \overline{u_j{}'\frac{\partial u_i{}'}{\partial x_j}} = \bar{f_i} - \frac{1}{\rho}\frac{\partial \bar{p}}{\partial x_i} + \nu\frac{\partial^2 \bar{u_i}}{\partial x_i \partial x_j} \tag{1.9}$$

With further manipulations and rearrangement, the momentum equation can be written as,

$$\rho\frac{\partial \bar{u_i}}{\partial t} + \rho\bar{u_j}\frac{\partial \bar{u_i}}{\partial x_j} = \rho\bar{f_i} + \frac{\partial}{\partial x_j}[-\bar{p}\delta_{ij} + 2\mu\bar{S_{ij}} - \rho\overline{u_i{}'u_j{}'}] \tag{1.10}$$

Further, most automotive flows are treated as steady state and iso-thermal process with a constant density ρ, the time dependent terms can be eliminated from time integration and the density ρ can be rearranged. This yields,

$$\bar{u_j}\frac{\partial \bar{u_i}}{\partial x_j} = \bar{f_i} + \frac{\partial}{\partial x_j}[-\frac{1}{\rho}\bar{p}\delta_{ij} + 2\nu\bar{S_{ij}} - \overline{u_i{}'u_j{}'}] \tag{1.11}$$

where δ_{ij} stands for the Kronecker delta, and S_{ij} is the mean rate of strain tensor defined as,

$$\bar{S_{ij}} = \frac{1}{2}(\frac{\partial \bar{u_i}}{\partial x_j} + \frac{\partial \bar{u_j}}{\partial x_i}) \tag{1.12}$$

Comparing Equation 1.11 and Equation 1.5, it can be seen that the RANS momentum equations have the same structure as that of the Navier-Stokes equations except the additional term $\overline{u_i{}'u_j{}'}$, which is called the Reynolds-stress tensor:

$$\tau_{ij} = \overline{u_i{}'u_j{}'} \tag{1.13}$$

The Reynolds-stress tensor is a symmetric tensor with six independent components. It can be seen from Equations 1.8 and 1.11 that there are more unknown quantities (pressure, three velocity components and six Reynolds stresses) than the number of the available equations (1 for continuity and 3 for RANS equations). This results into the so-called "closure" problem of the system of RANS equations. Since only the Reynolds-stress τ_{ij} contains the fluctuating quantities, the "closure" problem can be reduced to the modeling of the Reynolds-stresses in terms of mean-flow quantities.

The most popular approach to address the "closure" problem is the Boussinesq eddy-viscosity hypothesis [18]. It is based on an analogy between the molecular motion (collision and momentum exchange of discrete particles) and turbulent motion (assumed as a continuum), in order to correlate Reynolds stresses to the rate of the mean motion. Thus, by analogy with the molecular viscosity (a property of the fluid), turbulence is often described by a concept called "eddy" viscosity (a local property of the fluid). The Reynolds-stresses can be modeled as follows [19]:

$$\tau_{ij} = -\overline{u_i{}' u_j{}'} = 2\nu_t \bar{S_{ij}} - \frac{2}{3} k \delta_{ij} \tag{1.14}$$

$$k = \frac{1}{2} \overline{u_i{}' u_i{}'} \tag{1.15}$$

where k is the turbulence kinetic energy and ν_t is the turbulent viscosity. Unlike the molecular viscosity, the turbulent viscosity is not constant and may vary significantly from different flows and different points in the same flow. Substituting Equation 1.14 into Equation 1.11 with some manipulations leads to:

$$\bar{u_j} \frac{\partial \bar{u_i}}{\partial x_j} = -\frac{1}{\rho} \frac{\partial \bar{p}}{\partial x_i} + \frac{\partial}{\partial x_j} [(\nu + \nu_t) \frac{\partial \bar{u_i}}{\partial x_j}] + \bar{f_i} \tag{1.16}$$

RANS turbulence models based on the Boussinesq hypothesis are named as eddy viscosity models (EVMs). Traditionally, common and widely used RANS models are linear-eddy-viscosity models that can be divided into four main categories: (a)

algebraic (zero-equation) models, (b) half equation models, (c) one-equation models, and (d) two-equation models, not to mention that there are a number of less commonly used three and four equation EVMs. However, with increased computational powers, the former two approaches are currently mostly deprecated, and the latter two are more widely used. Some of the most commonly used RANS models will be introduced in the following section.

Another approach to resolve the "closure" problem is called the Reynolds Stress Transport (RST) models. RSTs are also known as second-moment closure models which directly calculate the individual components of the Reynolds stress tensor by solving their modeled governing equations. Due to the scope of this study, RST models will not be covered in further detail.

1.2.4 Large Eddy Simulation (LES)

The computational cost of performing DNS is tremendously high due to the requirement to resolve all the small scales at small time-step. On the other hand, RANS models are cost-effective but contain errors due to the modeling of the whole range of the turbulent spectrum. LES, which resolves directly the larger scales of the turbulence everywhere in the flow domain while models smaller scale motions, is a compromise between DNS and RANS. The LES technique is believed to be more accurate and informative than the RANS approaches. One justification is that the modeling error in the LES is less due to less of the turbulence is modeled. Furthermore, it is hypothesized that the smaller eddies are homogeneous and isotropic, i.e. self-similar, and thus simpler and more universal models can be formulated. Moreover, in contrast to the RANS equations, the LES equations are obtained by a spatial filtering rather than a time averaging process, thus LES is an inherently transient technique. However, the computational cost of the LES approach, although less than DNS, is still prohibitively for complex geometry at high Reynolds number. Until now, LES is still not affordable for most automotive flows and, thus, the details will not

be covered.

1.2.5 Detached Eddy Simulation (DES)

Several hybrid LES/RANS schemes have been introduced in order to achieve a better balance between the computational cost and accuracy for complex industrial applications. One of the successful hybrid schemes is the DES approach. DES is a hybrid modeling approach which combines the best of both RANS and LES: a RANS simulation in the boundary layers and a LES in the unsteady separated regions. To achieve this, DES models are constructed so that boundary layers and irrotational flow regions are solved using a base RANS closure model, however, if the grid is fine enough, a LES model in detached flow regions will be emulated [20]. Currently, there are mainly three base RANS models can be incorporated with the DES modeling approach, i.e. Spalart-Allmaras, Elliptic Blending K-Epsilon and SST $k-\omega$. The SST $k-\omega$ DES will be covered in the following section since it is the most widely used one for automotive flows.

1.3 Turbulence Models Evaluated for Full-scale Passenger Vehicle

Whilst evaluations of RANS and hybrid LES/RANS models on various applications are abundant in literature, such evaluations on full-car models are rare. In this study, four widely used RANS models in the automotive industry, i.e., the realizable $k-\epsilon$ two-layer, AKN $k-\epsilon$ Low-Reynolds, SST $k-\omega$, and V2F model will be evaluated on a full-scale passenger vehicle with two different front-end configurations. In addition, both cases will be run with two hybrid LES/RANS models to assess the difference of their predictions from RANS models. These include:

- RANS models
  - Realizable $k-\epsilon$ model (RKE) [21]
  - AKN (Abe-Kondoh-Nagano) Low-Re $k-\epsilon$ model (AKN) [22]
  - V2F $k-\epsilon$ model (V2F) [23]

  - SST $k-\omega$ model (SST) [24, 25]

- DES variants

  - Delayed Detached Eddy Simulation (DDES) [26]
  - Improved Delayed Detached Eddy Simulation (IDDES) [27]

RKE, AKN, and V2F are formulated based on the standard $k-\epsilon$ model. One of the main flaws of the standard $k-\epsilon$ model is that it may predict an anomalously large growth of turbulent kinetic energy in the stagnation regions. The usual explanation for the stagnation point anomaly is that the linear eddy viscosity formulation gives an erroneous difference in normal stress. The stagnation anomaly can be ameliorated by imposing the "realizability" constrain on the normal stresses [28, 29]. All the three $k-\epsilon$ models investigated in this study included the realizability constraint. While AKN and V2F implement the realizability through turbulent time scale, RKE enforces the realizability by damping functions.

One of the main differences between these three $k-\epsilon$ models is the way they are applied in the viscous-affected layer (including the viscous sub-layer and the buffer layer). AKN uses the low-Reynolds number approach by applying damping functions to some of the coefficients in the model. RKE adopts a two-layer approach [30], which solves for turbulent kinetic energy k but prescribes turbulent dissipation rate ϵ algebraically with distance from the wall in the viscosity dominated near-wall flow regions. On the other hand, the V2F model is valid up to the solid walls. It is designed to handle wall effects in turbulent boundary layers and to accommodate non-local effects [23, 31].

Another widely used two-equation model is the standard $k-\omega$ of Wilcox [32, 33]. However, a well-known flaw of the standard $k-\omega$ model is its sensitivity to free-stream/inlet conditions. Menter [24] addressed this problem in the SST model. The SST model effectively blends a $k-\epsilon$ model in the far-field with a $k-\omega$ model near

the wall. Thus, SST does not have the problem of sensitivity to free-stream/inlet conditions and is valid up to the wall. A modification is also made to the definition of the eddy-viscosity, which accounts for the effect of the transport of the principal turbulent shear stress [24].

Besides RANS approaches which model all scales, another approach to model turbulence is called the scale-resolving simulation which resolves the large scales of turbulence and models the small-scale motions. A common scale-resolving simulation is called the Large Eddy Simulation (LES). The problem with LES is that it is still too computationally costly for automotive flows. Detached Eddy Simulation (DES) is a hybrid modeling approach which combines the best of both RANS and LES: a RANS simulation in the boundary layers and a LES in the unsteady separated regions. Two variants of the DES were investigated in this study: DDES and IDDES. The DDES model incorporates a delay factor that enhances the ability of the model to distinguish between the LES and RANS regions on meshes where spatial refinement could give rise to ambiguous behavior. The IDDES approach allows RANS to be used in a much thinner near-wall region, in which the wall distance is much smaller than the boundary-layer thickness. In this study, the base RANS model used in these two DES variants is SST $k-\omega$.

1.4 Fine-tuning the SST $k-\omega$ Model for Improved Prediction of Automotive Flows

Transient Scale Resolved Simulations, such as the Detached Eddy Simulation, are currently seen to be the preferred modeling approach over the steady-state Reynolds Averaged Navier-Stokes (RANS) simulations due to the former's perceived capability of providing more realistic flow field predictions. However, the latter approach is still a widely used methodology in road vehicle aerodynamic developments because of its faster turn-around time and cost-effectiveness. However, RANS models generally fail to produce well-correlated predictions. Studies reveal that a good correlation with

experiment cannot be achieved by simply refining the mesh when using RANS models. As such, this study explores the possibility of improving the prediction veracity by investigating the influence of a few selected model closure coefficients on the CFD prediction.

Both of $k-\epsilon$ and $k-\omega$ models belong to the two-equation eddy-viscosity RANS category. The two-equation models were developed mainly on the basis of dimensional analysis. The postulation of transport equations of the two-equation RANS models involves unknown double and triple correlations. Those unknowns have been replaced with algebraic expressions involving known turbulence and mean-flow properties by introducing closure coefficients. For example, the $k-\omega$ model has six coefficients, viz., α, β_0, β^*, σ, σ^* and σ_{d0}. Therefore, the two-equation RANS models are not exact. Consequently, the values of the closure coefficients were set by assuring agreement with observed properties of turbulence from canonical flows. For instance, the ratio of β^* to β_0 was established by applying the $k-\omega$ model to decaying homogeneous, isotropic turbulence.

Considering the way that the values of closure coefficients of the two-equation RANS models were determined, it is not surprising that the RANS models often fail to correctly predict automotive flows which feature complex geometry and exhibit massive flow separations. Furthermore, even the transient DES models, for computational realizability, adopt the RANS simplification in the regions very close to solid walls. Due to that the SST model combines the best of both $k-\epsilon$ and $k-\omega$ models and it can be incorporated into the DES approach. We are motivated to investigate the possibility of improving the prediction of automotive flows by tuning the SST model closure coefficients through a systematic evaluation of the sensitivities of five important closure coefficients, viz., β^*, $\sigma_{\omega 1}$, $\sigma_{\omega 2}$, σ_{k1}, and σ_{k2}.

1.5 CFD Tools

In general, a typical CFD analysis involves three steps: (1) preprocessing, (2) running the simulation, and (3) post-processing and result analysis. The primary preprocessing operations in this study included cleaning the CAD and then manual surface meshing of the cleaned CAD to ensure that all intricate geometry details were not lost during an automated meshing process. This was achieved by using a commercial software ANSA, by Beta CAE Systems. The geometry cleaning process also involved making some simplifications to the vehicle model by removing components that do not have any significant interaction with the airflow, like the vehicle's interior components. The resultant surface mesh was exported in NASTRAN format to be imported by the simulation program, again a commercial finite volume CFD code Star-CCM+ by CD-ADAPCO in which the surface re-meshing, volume meshing, simulation and post-processing operations were carried out.

In Star-CCM+, the finite volume method is used for the spatial and temporal discretization of the governing equations. The integral form of the conservation equations of mass and momentum are solved by the segregated flow solver in a sequential manner, i.e. the non-linear governing equations are solved iteratively one after the other for the solution variables such as the three velocity components and the pressure. The pressure-velocity coupling is achieved with a predictor-corrector approach called SIMPLE (Semi-Implicit Method for Pressure-Linked Equations). For RANS models, the discretization scheme for computing the convection flux on a cell face is Hybrid MUSCL (Monotonic Upwind Scheme for Conservation Laws) third-order/central-differencing; for DES variants, the discretization scheme is Hybrid/BCD (Hybrid second-order upwind/bounded-central). A second-order upwind scheme is used for computing the convection flux on a cell face for each turbulence model solver. An interested reader is directed to the Star-CCM+ user manual for further details.

1.6 Motivation

The demand for better fuel economy pushed by both consumer and Environmental Protection Agency (EPA), made OEMs to put more effort into other areas besides vehicle external aerodynamics. As one of these areas, underhood airflow management has taken an important role in the new road vehicle design process, due to the combination of growing engine power demands, utilization of sophisticated under-hood and underbody devices, and emission regulations. The complexity of the underhood compartment makes both the experimental and analytical approaches difficult. Therefore, 3D CFD simulation has become a cost-effective alternative for underhood airflow investigation. For underhood airflow management, existing works demonstrated two main benefits of incorporating an air-duct in the vehicle cooling system. Firstly, the air duct improves both the airflow rate through and flow uniformity over the radiator by streamlining the flow and partially sealing-off the CRFM at high vehicle speeds, and secondly, it reduces the hot air recirculation at vehicle idle conditions. For road vehicles, these benefits could lead to an implementation of a smaller radiator, and reduction of the total drag, thus could improve the fuel efficiency. However, very few works have been done on the comparison of different air-duct designs for a full-scale vehicle model. In this backdrop, the author was motivated to perform a 3D CFD study of the effects of the air-duct geometry and size of the grille opening on the radiator cooling performance and cooling drag at different operating conditions. The investigation involves several design iterations of air-duct geometry and front grille opening. The results are assessed based on several important flow parameters associated with the cooling airflow, such as the airflow uniformity, total mass flow rate through the radiator and front grille opening, and total vehicle drag.

The turbulence model used to conduct the underhood airflow management study was a RANS model, i.e. Realizable $k - \epsilon$. Although well-correlated drag coefficient prediction was achieved, the author acknowledged that RANS models generally often

fail to predict flow features correctly. Therefore, the author was motivated to evaluate the performance of some commonly used RANS models in automotive industries and compare their prediction differences with higher-order hybrid LES/RANS models. Whilst evaluations of RANS and hybrid LES/RANS models on various applications are abundant in literature, such evaluations on full-car models are rare. In this study, four widely used RANS models in the automotive industry, i.e., the realizable $k-\epsilon$ two-layer, AKN $k-\epsilon$ Low-Reynolds, SST $k-\omega$, and V2F model was evaluated on a full-scale passenger vehicle with two different front-end configurations. In addition, both cases were run with two hybrid LES/RANS models to assess the difference of their predictions with that from RANS models.

From the turbulence models evaluation work, the author found that the cost of DES models are still quite high, rough 10 times higher than RANS approaches, and they are not always guaranteed to predict better-correlated drag values. Thus, the author is motivated to improve the performance of the SST $k-\omega$ model on predictions of automotive flow by fine-tuning some closure coefficients of its transport equations. Among the investigated RANS models, the reason to study SST $k-\omega$ model is due to that the SST model combines the best of both $k-\epsilon$ and $k-\omega$ models and it can be incorporated into the DES approach. Thus, the author investigated the possibility of improving the prediction of automotive flows by tuning the SST model closure coefficients where the sensitivity of five important closure coefficients, viz., β^*, $\sigma_{\omega 1}$, $\sigma_{\omega 2}$, σ_{k1}, and σ_{k2} were investigated.

1.7 Objectives

The main goal of this dissertation is to contribute to the CFD simulation based analysis of road vehicle aerodynamic flows. CFD simulation of road vehicle aerodynamics is such a broad area, the author could only cover a small part of it. The three objectives are:

1. Reduce cooling drag and improve cooling performance of the radiator simultane-

ously for a model of Hyundai Veloster by performing a 3D CFD study of the influence of underhood flow features on the cooling and external aero behavior of the car.

2. Evaluate the turbulence modeling effects on the CFD predictions of flow details over a full-scale passenger road vehicle.

3. Improve the performance of the SST $k-\omega$ model on predictions of automotive flow by fine-tuning closure coefficients of modeled transport equations.

1.8 Dissertation Outline

This dissertation is composed of three articles and organized as follows,

Chapter 2: Full vehicle CFD investigations on the influence of front-end configuration on radiator performance and cooling drag, (published in *Applied Thermal Engineering* vol. 30, pp. 1328-1340, 2018 [37])

Chapter 3: Investigation of the Turbulence Modeling Effects on the CFD Predictions of Flow over a Passenger Road Vehicle (will be submitted to *Computers & Fluids*)

Chapter 4: On Fine Tuning the SST $k-\omega$ Turbulence Model Closure Coefficients for Improved Prediction of Automotive External Flows (Accepted for publication by the ASME 2018 International Mechanical Engineering Congress and Exposition; recommended for journal publication)

Chapter 5: Conclusion

CHAPTER 2: Full Vehicle CFD Investigations on the Influence of Front-end Configuration on Radiator Performance and Cooling Drag

2.1 Abstract

Proper underhood airflow management of road vehicles has two distinct objectives, viz. ensure the required cooling performance of the heat exchangers, and minimize the cooling drag component of the total vehicle drag. From the radiator performance perspective, there are distinct concerns according to the vehicle speeds. At highway speeds, the flow rate and flow-distributions over the radiator surface are the major operating parameters influencing the performance of a radiator. However, at low vehicle speeds, a phenomenon detrimental to the A/C system performance, called the underhood hot air recirculation, may occur. The cooling airflow not only causes drag directly, the interaction of under-body flow with other vehicle components may lead to more interference drag. This paper presents computational studies to investigate underhood airflow features associated with radiator performance and cooling drag. Additionally, analysis of the impact of the front grille opening size and underhood passive aerodynamic devices on the cooling drag and radiator performance are presented based on full vehicle CFD simulations carried out using a model of Hyundai Veloster. It is demonstrated in this study that by properly manipulating the cooling airflow pattern, simultaneous improvement of radiator performance and total vehicle drag can be achieved.

2.2 Introduction

During the last two decades, the aerodynamic drag reduction has become a very important issue for the automakers. This is due to Environmental Protection Agency

regulations aiming at reducing greenhouse gas emission plus the demands for fuel-efficient vehicles from the customers. As a result, we have seen a significant reduction in the parasitic drag of road vehicles. While the external aerodynamics aspect of this effort has been researched intensively and well understood, the underhood airflow management still requires further in-depth understanding, in spite of the fact that the rapid development in both experimental and numerical techniques has resulted in a vast number of studies involving vehicle underhood flow. The literature contains such a wide variety of works in this area that the due diligence will not be done by citing just one or two references. However, a good starting point is the vehicle aerodynamics collections published annually by the Society of Automotive Engineers (SAE). Other notable references include: the doctoral dissertation of Littlewood [5], master's thesis of Sawyer [6], review papers by Altaf et al. [7] and Patten et al. [8], to cite but a few.

Several factors render the underhood airflow management of modern cars challenging. These include the presence of a number of additional heat sources, such as the supercharger or turbocharger, the requirement of heat-shielding of electronic components, enhanced interior climate control, and, most importantly, the demand for a more compact design. The prime objective of airflow and thermal management within the underhood environment is to ensure proper cooling of the engine with least power consumption and aerodynamic resistance. The cooling of the engine is mainly achieved by making sure that adequate airflow passes through the front end module. The front end module typically consists of a condenser, a radiator, and a fan module, and is called the CRFM for short. Some modern vehicles also have a turbocharger intercooler. However, excessive cooling airflow may increase the drag of the vehicle. Thus, the desired design of the CRFM should provide an optimum performance of the cooling system and contribute to the vehicle's parasitic drag reduction simultaneously.

The airflow through the CRFM is driven by two sources: (1) the fan suction, and

(2) the ram air generated by the movement of the vehicle. These two sources usually work at different vehicle speeds. The fan suction behind the radiator is the main driving force for the airflow at low vehicle speeds. Subsequently, when the vehicle speed is below a certain threshold, the negative static pressure generated by the electric fan may exceed the positive static pressure between the front grille opening and condenser core. This may cause a portion of the hot air from the engine bay to recirculate to the plenum through the bypass channel. This undesired phenomenon is known as the underhood hot air recirculation. This hot air recirculation would be detrimental to the performance of the A/C system. Eliminating this bypass channel could not only minimize the hot air recirculation, but also improve the underhood cooling efficiency. Existing literature contains a large number of works showing that an air-duct design could reduce the hot air recirculation significantly, c.f. Song et al. [9].

In general, there are two factors affecting the performance of the cooling system: (1) the mass flow rate through the radiator inlet, and (2) the flow distribution over the radiator inlet surface. The mass flow rate and flow distribution depend on the grille opening size, position, and the underhood resistance. The primary requirement for the underhood airflow management is to ensure sufficient airflow passing through the radiator, and, thus, make sure that the engine won't overheat. However, excessive airflow in the underhood increases the cooling drag. Therefore, the challenge of the underhood airflow management is to find the balance. As suggested by several works, front end sealing, and introduction of air-duct are seen to be the two effective ways of improving both airflow uniformity over and mass flow rate through the radiator surface [10, 11, 12]. Additionally, Saab et al. [13] suggested that reducing the front grille opening reduces both cooling and total drag.

The complexity and compactness of modern vehicle underhood compartment make the experimental and analytical approaches of optimal airflow management rather

challenging. Thereby, 3D CFD analysis appears to be a cost-effective plausible alternative to investigate the underhood airflow characteristics during a vehicle's early design stage. A vast body of work related to the underhood airflow CFD investigations can be found in the literature; however, only a handful of these, which have a direct relevance to the current work, are cited here. Additionally, the use of active grille shutter as a drag reducing device is widespread in industry, however, as this is outside the scope of this paper, discussions pertaining to this device is avoided.

Analytical approaches and experiments on simplified underhood model were widely used a decade ago, when CFD simulations of full vehicle model with detailed underhood components were too costly and beyond the capability of the available computational resources. The work of Barnard [38] is most relevant to the present study where he formulated empirical expressions for calculating the aerodynamic drag due to the cooling airflow. Chometon and Gillieron [39] discussed a method for estimating the heat transfer performance of the cooling system during cold aerodynamic tests in a wind tunnel. Additionally, Gillieron and Chometon [40] presented an analytical approach, based on an integral balance of momentum method, to identify the parameters which contribute to the cooling air drag of road vehicles. Ivanic and Gillieron [41] furthered this study by proposing two models of increasing complexity. Several suggestions on how to reduce the cooling drag were presented. More recently, Tesch et al. [42] introduced a new formulation of the cooling drag where they separated the drag contributions from internal losses, the inlets and outlets areas, and the interference effects. They showed that the interference drag has a large effect on the aerodynamic drag which strongly depends on the outlet location of the cooling air duct. Williams et al. [43] derived a mathematical representation of the pressure recovery/loss of the front-end subsystem. They showed that the effect of a non-uniform flow on heat exchanger pressure loss could be significant.

Typically, cooling drag is defined as the difference between the total drag of a

vehicle with cooling airflow and the total drag of the mock-up model in which the airflow inlets are closed; see equation 2.4 for definition. However, for real cars, the cooling drag measurements are generally lower than would be expected from free stream momentum (or ram drag) considerations. Williams [44] suggested that the primary reason for this is the reduction in spillage drag. Wickern et al. [45] discussed the mechanism of the cooling drag reducing interferences associated with the vehicle wheels and the effect of ground simulation. They showed that the cooling drag reducing the effect of the inlet spillage drag is strongly associated with the presence of wheels, and the cooling drag is higher with rotating wheels compared to the stationary wheels. With a focus on the surface pressure of the vehicle, Baeder et al. [46] investigated the cooling-air interference effects using experimental, numerical and analytical methods. They observed that when the cooling-air inlet is open, the pressure rises around the inlet while the pressure around the outlet drops.

As stated earlier, one of the primary goals of underhood airflow management is to reduce the cooling drag. Some researches focused on the influence of the engine bay design on the cooling drag. Christoffersen et al. [47] presented a study on the influence of the engine bay packaging density and layout on the exterior aerodynamics of a vehicle. They found that a reduction in overall drag could be achieved by exiting the cooling airflow at the rearmost part of the front wheel housings. D'Hondt et al. [48] carried out a systematic analytical, experimental and numerical work investigating the effect of air flow rate through the engine compartment on the aerodynamic drag. Some other works focused on the front end components too. Kuthada and Wiedemann [49] analyzed the cooling airflow system of a full scale production car using an integrated approach of numerical and experimental methods. They showed that the front end region contributes most to the total drag changes due to the cooling airflow and the flow leaked around the radiator core is the major contributor. A generic vehicle model with a detailed underhood was designed by FKFS to lay the foundation for a common

investigation model. Wittmeier and Kuthada [50] described the model in details, and presented first results from both CFD and wind tunnel measurements in quarter scale. They showed that although the size of the upper grille is larger, only 40% of the cooling air enters through it, and a reduction in both cooling drag and airflow rate is observed when closing either one of the grilles. These results indicate that both the size and position of the grille opening impact the cooling airflow characteristics.

Manna and Kushwah [51] carried out 3D CFD analyses to optimize the underhood airflow by incorporating improved sealing and making fan shroud modifications by adding speed-flaps and vanes. They showed that these modifications can maximize the airflow at high vehicle speeds while still satisfying the condensing needs of the A/C system by maintaining sufficient airflow with low hot air recirculation at idling conditions. Jahani and Beigmoradi [52] investigated the effect of vehicle front end geometry changes including the whole bonnet, grille and bumper using 3D CFD simulations. They showed that local modifications, such as the inclusion of air-guide, flap and anti-recycler can lead to more than 10% improvement in cooling flow rate, as well as, improvement of the flow uniformity over the radiator surface. A similar work was presented by Regin [53] too.

The modern vehicles underhood has become increasingly crowded with multiple heat sources. Thus, another important aspect of underhood research is the thermal management. Khaled et al. [54] analyzed the vehicle underhood flow experimentally for three functioning points, i.e. the constant-speed driving phase, the slowdown phase, and the thermal soak phase. Their work can serve as a comprehensive database for validating numerical codes and a better understanding of the physical phenomena in the underhood compartment. Furthermore, to better understand the rule of heat radiation in underhood thermal management, they developed a method to measure separately the convective and radiative heat fluxes in an automotive underhood compartment [55, 56]. In addition, Khaled et al. [57] presented a review of underhood

aero-thermal management. They evaluated the qualitative impact of each individual component on the aero-thermal environment of the underhood and classified different components into three orders of impact. Based on the impact orders, they designed and built a new simplified automobile body for the purpose of aero-thermal analyses. Mao [58] conducted an underhood thermal analysis of a heavy-duty truck using CFD combined with thermal analysis tools. This study only included several important underhood components with a total of 9.5 million volume cells. Their findings help to determine the operating point of the cooling fan, the core size of the heat exchangers, and the thickness of heat shields for a heavy-duty truck. Kim [59] developed a 3D CFD program to analyze the performance of the vehicle cooling system. A simplified vehicle model with only front end part and around 5 million cells was used in this study. Good agreements were found between simulation and experimental test. Although simplified geometry model can provide insight and guide for underhood aero-thermal management, the authors believe that a full-scale vehicle model with detailed underhood components should be investigated in order to better understand the underhood aero-thermal phenomenon.

The works cited above demonstrated two main benefits of incorporating an air-duct in the vehicle cooling system. Firstly, the air duct improves both the airflow rate through and flow uniformity over the radiator by streamlining the flow and partially sealing-off the CRFM at high vehicle speeds, and secondly, it reduces the hot air recirculation at vehicle idle conditions. For road vehicles, these benefits could lead to an implementation of a smaller radiator, and reduction of the total drag, thus could improve the fuel efficiency. However, very few works have been done on the comparison of different air-duct designs for a full-scale vehicle model. In this backdrop, the effects of the air-duct geometry and size of the grille opening on the radiator cooling performance and cooling drag at different operating conditions are presented in this paper using a 3D CFD approach. The investigation involves

several design iterations of air-duct geometry and front grille opening. The results are assessed based on several important flow parameters associated with the cooling airflow, such as the airflow uniformity, total mass flow rate through the radiator and front grille opening, and total vehicle drag.

2.3 Theoretical Background

The radiator protects the engine from overheating by transferring heat from hot coolant that flows through it to the airflow blown over it. Thus, its performance largely depends on the mass flow of air and the flow-distribution or flow-uniformity over the radiator surface. However, due to the influences of the front grille opening, license plate, the bumper reinforcement upstream and the cooling fan and fan-shroud downstream, the flow distribution over the radiator upstream surface is not uniform in most vehicles. The uniformity of airflow can be quantified by a parameter called the uniformity index γ, which can be defined as:

$$\gamma = 1 - \frac{\sigma}{\overline{u}} \tag{2.1}$$

where $\overline{u}$ is the superficial normal velocity. The variance of the airflow distribution σ is defined as:

$$\sigma^2 = \frac{\sum_i^N (u_i - \overline{u})^2 \times \|a_i\|}{\sum_i^N \|a_i\|} \tag{2.2}$$

The superficial normal velocity $\overline{u}$ is defined as:

$$\overline{u} = \frac{\sum_i^N u_i \times a_i}{\sum_i^N \|a_i\|} \tag{2.3}$$

Where N is the total number of faces on the radiator upstream surface, i is the face index, a is the face area and u is the velocity.

Some previous studies assessed that, for full-scale production vehicles, the cooling

flow accounts for as much as 10% of the total drag of the vehicle (see Baedar et al. [46]) at the highway speed. The cooling flow through the underhood is pressure driven, with a high pressure at the grille opening due to the stagnation at the front and a low pressure region around the exits. After passing through the inlets, the cooling airflow loses energy and momentum due to the presence of underhood components in combination with the interference effects of the exiting air and surrounding flows. These losses cause an increase of the total drag of the vehicle, termed as the cooling drag, which is the difference between the total drag of a vehicle with cooling airflow and the total drag of the mock-up model in which the airflow inlets are closed. Thus, the cooling drag coefficient C_D^C is defined as:

$$C_D^C = C_D^{CA} - C_D^M \tag{2.4}$$

where C_D^{CA} stands for the vehicle drag coefficient with cooling airflow, and C_D^M is the drag coefficient of the mock-up model without the cooling airflow. Although the above definition is widely accepted in the automotive industries to measure the cooling induced drag, its limitations have been well understood due to the complexities of interference with the surrounding flows.

2.4 Simulation Details

A full scale Hyundai Veloster, as shown in Figure 2.1 , was used as the vehicle model in this study. In general, a typical CFD analysis involves three steps: (1) Pre-processing, (2) Running the simulation, and (3) Post-processing and result analysis. The primary preprocessing operations in this study included cleaning the CAD and then manual surface meshing of the cleaned CAD to ensure that all intricate geometry details were not lost during an automated meshing process. This was achieved using a commercial software ANSA, version 15.02 by Beta CAE Systems. The geometry cleaning process also involved making some simplifications to the vehicle model by

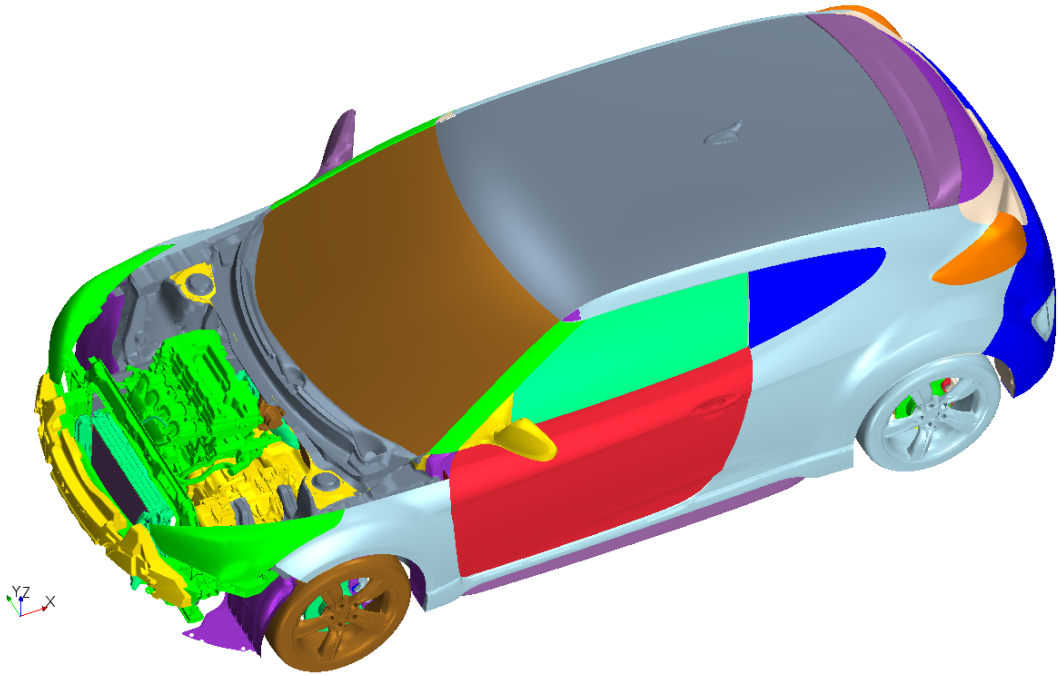

Figure 2.1: Full vehicle model with detailed underhood components.

removing components that do not have any significant interaction with the airflow, like the vehicle's interior components. The resultant surface mesh was exported in NASTRAN format to be imported by the simulation program, again a commercial finite volume CFD code Star-CCM+ version 10.04 by CD-ADAPCO in which the surface re-meshing, volume meshing, simulation and post-processing operations were carried out.

2.4.1 Coordinates System

In this paper x, z, and y axes represent the streamwise, vertical and lateral directions respectively, see Figure 2.1. The symbols U, V and W represent the streamwise, lateral and normal components of the mean velocity respectively. A subscripted symbol, such as U_i would represent the streamwise velocity U corresponding to the case i (the details of the cases studied can be seen in the proceeding section).

2.4.2 Cases Studied

In order to characterize the features of the underhood airflow, and to achieve a simultaneous improvement in cooling performance and reduction in cooling drag, a total of six cases with two air-duct and front grille-opening configurations were studied in this investigation. The cases considered included two different orientations of the CRFM as well; one vertical, and the other slightly inclined. The primary reason for inclining the CRFM is to enhance the effectiveness of the air-duct by directing more airflow towards the upper part of the radiator. The two different air-duct designs considered included one with a narrow 5 degree opening and the other with a wide 35 degree opening as shown in Figure 2.2 . The two grille-opening configurations include a baseline grille-opening, and a partially sealed-off grille-opening where both the left-most and the right-most segment of the grille were taped off. The grille-opening configurations and the CRFM orientations are shown in Figure 2.3.

The six cases investigated can be summarized as:

(a) Case 1: the baseline model with a vertical radiator and no air-duct,

(b) Case 2: the mock-up model used to determine the cooling drag per Eq. 2.4 which is similar to the baseline model except that the front grille openings are completely sealed off,

(c) Cases 3 – 6: include a 9 degree inclined CRFM with different air-duct designs and grille-opening configurations:

- Case 3: contains narrow air-duct with a 5 degree opening with the baseline grille-opening, i.e. no side-sealing,
- Case 4: same as case 3, but with both left- and right-most part of the grille-opening sealed off,

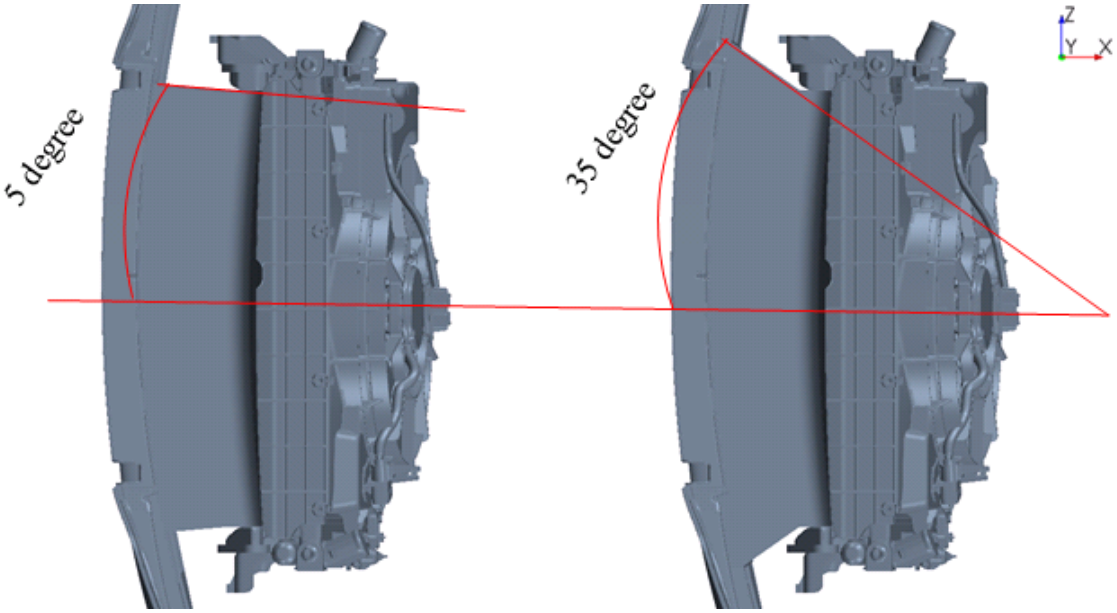

Figure 2.2: The narrow and wide air-duct designs. (Left) the narrow air-duct with 5 degree opening as used in cases 3 and 4. (Right) the wide air-duct with 35 degree opening as used in cases 5 and 6.

- Case 5: include a wide air-duct with a 35 degree opening with the baseline grille-opening, i.e. no side-sealing,
- Case 6: same as case 5, but with both left- and right-most part of the grille-opening sealed off.

2.4.3 Mesh Settings

The imported model in NASTRAN format was remeshed using surface remesher model in Star-CCM+. The surface wrapper and gap closure operations were then invoked in Star-CCM+ to generate a closed or so called *water-tight* geometry by closing small gaps. Sufficient care had been exercised so that this process produced a high quality surface mesh with no observable alteration of the original starting surface-mesh. The volume mesh was then generated using the trimmer mesh model along with the prism-layer mesh model. The trimmer produces predominantly hexahedral cells, while the prism-layer mesh model produces prismatic-cells over the CAD surface

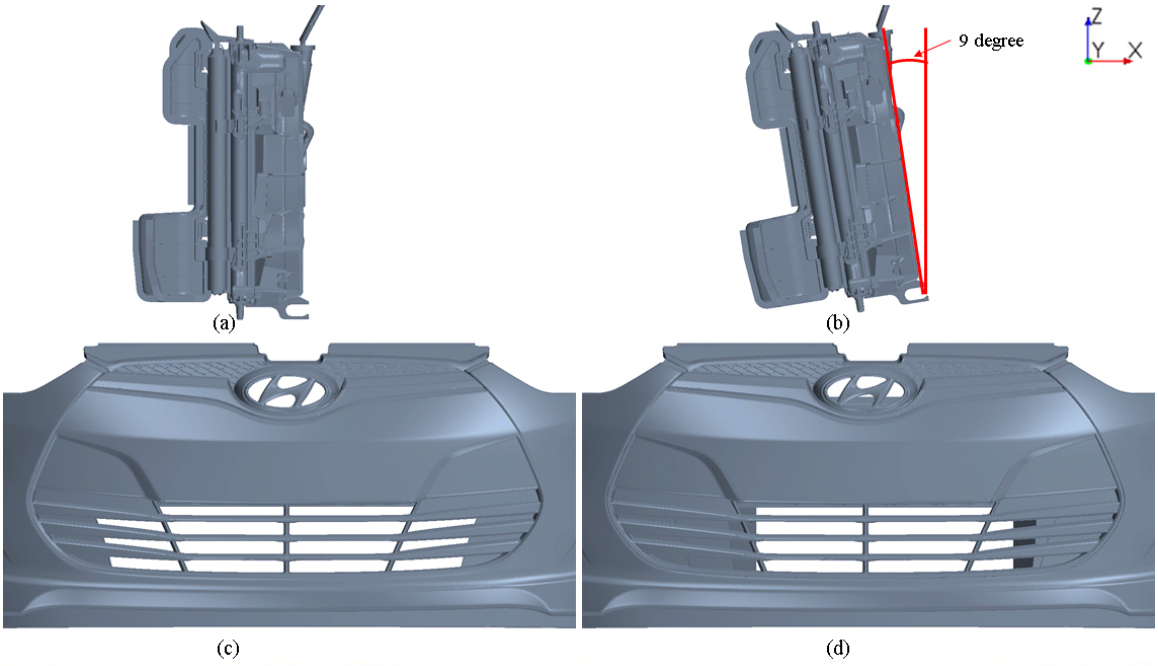

Figure 2.3: Front-end geometry details. (a): the vertical CRFM without air-duct used in cases 1 and 2; (b): the 9 degree inclined CRFM used in cases 3-6; (c): the grille-opening used in cases 1, 3 and 5; (d) the grille opening with both side-grille-openings sealed off as in case 6. Note that case 4 is similar to case 6, but with a narrower 5 degree air-duct.

to maintain a high quality discretization of the wall-regions of solid objects; these prismatic cells ensure that the boundary layer over any wall is properly captured. The location of the wall-node is critical as the effectiveness of some of the physics models used in the simulation setup greatly depends on the value of this node. Volume sources were used to refine the mesh in the vicinity of the model and in critical areas like the wake of the body; these volume sources are also used to ensure a smooth transition from finer cells to coarser cells. The other objective of using volume sources is to create an optimum simulation that produces reliable results in a cost effective way.

Setting up of the final parameters for the mesh settings is a trial and error process where various combinations of the mesh parameters, the total height of the prism layer, number of prism layers, the first-node wall-distance, and the size of the finest core grid, were tried. This was done to make sure, firstly, that the resultant mesh conforms with the requirements of the chosen physics models and, secondly, the predicted macroscopic quantities like the drag coefficient become independent of the mesh refinement. This procedure resulted in the selection of the following mesh parameters: (a) the prismatic cells layer total thickness of 10 mm, (b) 12 prism layers, (c) the first node height of 0.03 mm for the critical front end components, and (d) core mesh cell sizes from 4 mm around the CRFM to 20 mm around other part of the model. This resulted in a simulation with around 100 million cells, in which only 0.004% of the cells show volume change less than 1e-4 and minimum face quality less than 0.8. Identical mesh settings were applied to all the cases investigated. The final mesh of the cross section through the central plane of the vehicle is displayed in Figure 2.4. The mesh around CRFM is shown in Figure 2.5, in which the red line represents a horizontal plane going through the middle of lowest grille opening.

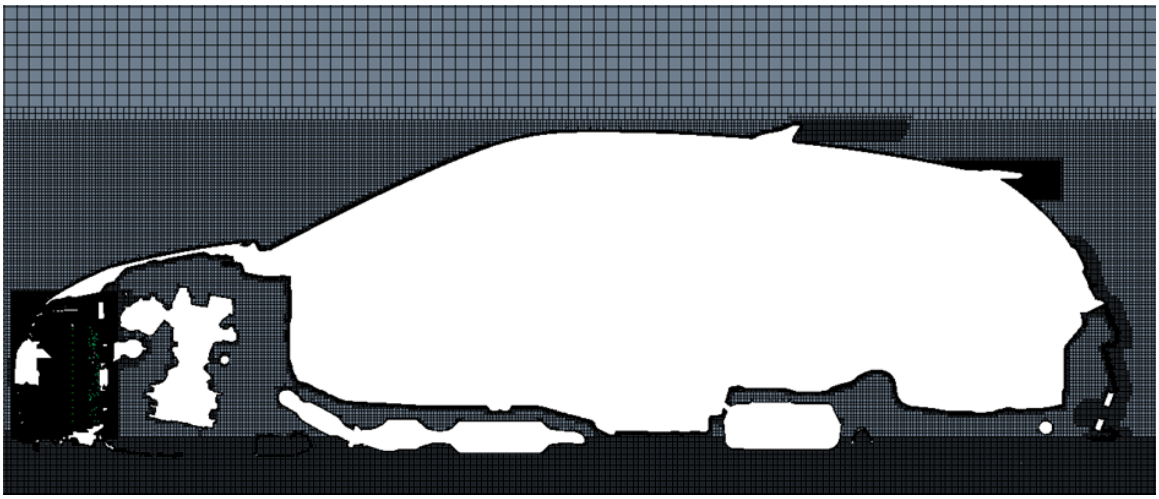

Figure 2.4: Mesh on the central plane of the vehicle ($y = 0$).

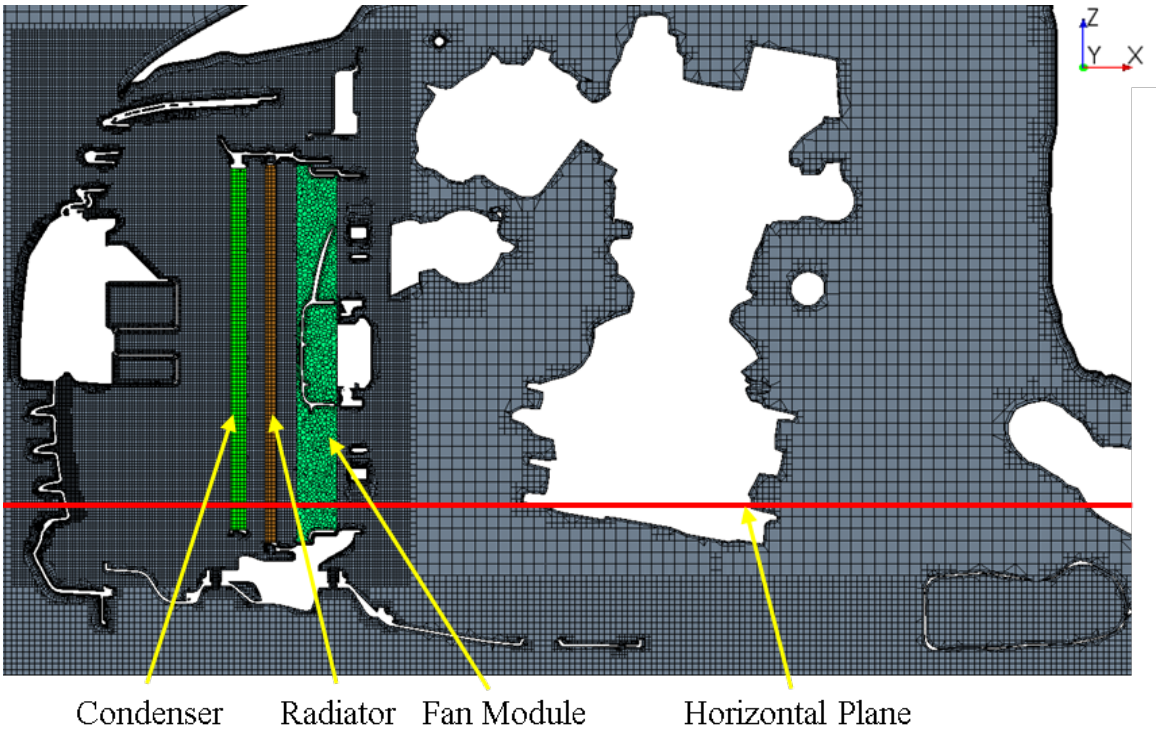

Figure 2.5: Closeup view of the mesh around the CRFM.

2.4.4 Boundary and Operating Conditions

All the vehicle models were simulated in a rectangular virtual wind tunnel as displayed in Figure 2.6. The length, height and the width of the tunnel were $26L$, $10L$, and $10L$ respectively, where L represents the overall length of the car. A velocity inlet was placed $5L$ upstream from the front-end of the vehicle while a pressure outlet boundary was placed $20L$ downstream from the rear of the vehicle. Non-slip moving wall boundary condition was applied on the ground with the tangential speed same as the air-speed. The top and side walls were modeled as zero-gradient planes.

To fully evaluate the performance of the radiator, both idle and highway speeds were investigated in this study. Sometimes, at highway speeds, some OEMs turn the fan off. Subsequently, we have the following three operating conditions to investigate:

1. Idle condition with fan rotation speed of 2000 rpm,
2. Highway speed of 70 mph or 112.7 km/hr (31.3 m/s) with fan rotation speed of 2000 rpm, and
3. Highway speed of 70 mph (31.3 m/s) with fan stationary.

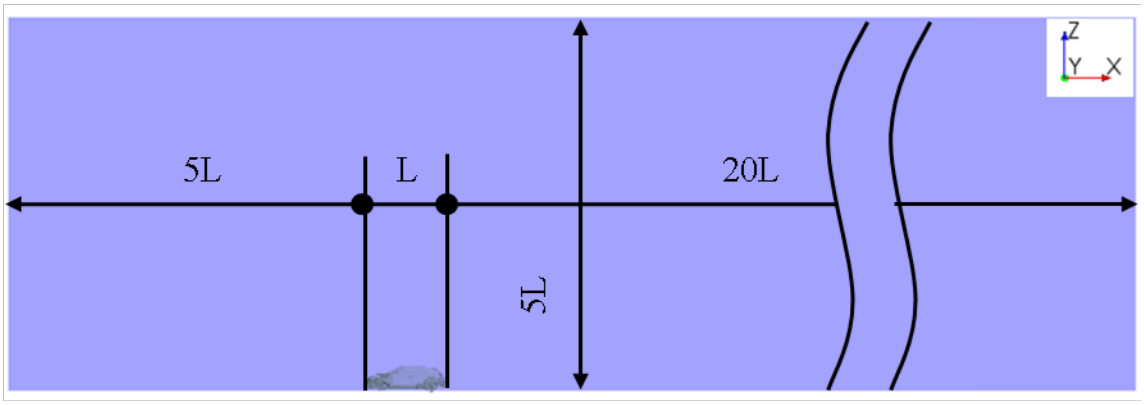

Figure 2.6: Computational domain.

2.4.5 Physics Setup

As outlined earlier, the main goal of this study is to improve the cooling performance of the radiator and reduce cooling drag by manipulating the underhood airflow. In order to achieve this objective, steady-state Reynolds Averaged Navier-Stokes (RANS) simulations were run using the Realizable $k-\varepsilon$ turbulence model of Shih et al. [21] in conjunction with the two-layers all y^+ wall-treatment approach. This model has been widely used in automotive industries. Generally speaking, the $k-\varepsilon$ models perform well for external flow problems around complex geometries. The wall treatment approach is expected to produce the most reliable results within the buffer region where $1 < y^+ < 30$. The y^+ values on the external surfaces of the vehicle in all the cases were mostly less than 5 as can be seen in Figure 2.7.

The cooling fan rotation was modeled using the Moving Reference Frame (MRF) method which is widely used for modeling rotating components in the steady-state analysis. In this approach, a separate region enclosing the entire rotation region must be defined, and a rotating reference frame is assigned to that region. Therefore, a constant grid flux will be generated in the appropriate conservation equations. This grid flux is calculated based on the properties of the reference frame rather than the local motion of the cell vertices. The position of cell vertices does not change in the MRF region. The MRF approach could provide realistic results of the pressure jump across the fan and swirl components generated by the fan rotation without the need of experimental data as input. The condenser and radiator were also modeled as separate regions, in which they were modeled as porous media where the pressure drop is defined as a function of velocity which was obtained from experimental tests. These three regions are displayed in Figure 2.5. The wheel rotation was modeled by setting the tangential velocity specification as the local rotation rate.

Since the mock-up case was used to calculate cooling drag as per Eq. 2.4, it was only run at highway speed conditions. All other cases were run with all three operating

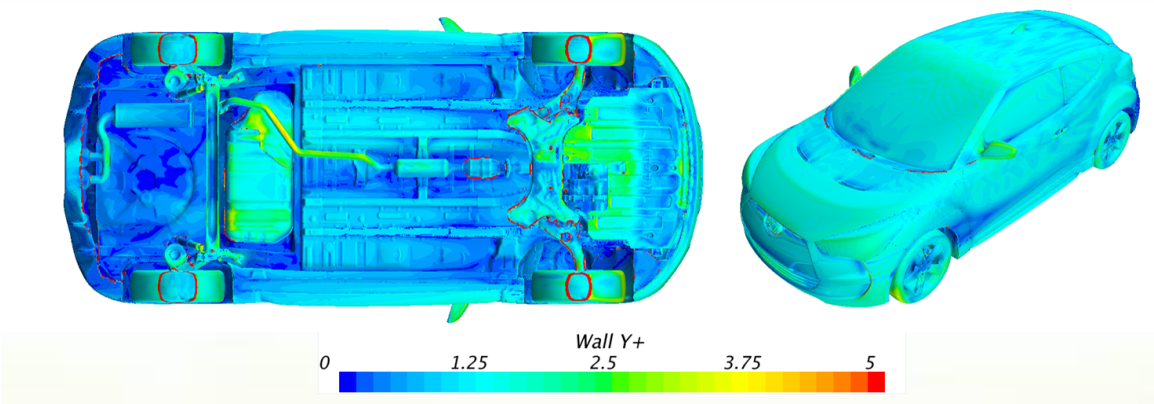

Figure 2.7: Wall y^+ value on the external surfaces of the vehicle.

conditions. Thus, there were 17 simulations carried out in total.

2.5 Results and Analysis

All of the simulations were run on a cluster with 96 computing cores where each simulation took around 30 hours to be completed. Results were analyzed to determine the best air-duct case in terms of radiator performance and drag coefficient. Due to the proprietary nature of the data, the drag coefficient values presented in this paper were normalized in such a way that the drag coefficient, C_D of the baseline car (case 1) matches with the one available in the public domain. Data downloaded from the website Edmunds.com, "Features & Specs 2014 Hyundai Veloster", https://www.edmunds.com/hyundai/veloster/2014/features-specs/, accessed June 19, 2017, indicates that the drag coefficient of a 2014 Hyundai Veloster is 0.320.

2.5.1 Inclined CRFM in Air-dcut Cases

In the initial design stage of this vehicle model, the baseline case had a vertical CRFM as seen in Figure 2.3 (a). In addition, the front grille opening aligned mainly with the bottom part of the CRFM. One can easily speculate that with this front end configuration, most of the ram airflow is likely to flow towards the bottom part of the radiator, making the upper part of the radiator less efficient. As can be seen from the CFD analysis of the baseline case in Figure 2.8, ram airflow blows directly

to the bottom part of the CRFM, which likely provides more than sufficient cooling air to that area of the radiator. However, for the top part of the CRFM, while a high velocity airflow stream is deflected upward, this stream is almost parallel to the radiator surface, which makes the velocity normal to the radiator surface very low (see the area marked by the red rectangle). To improve the efficiency of the cooling airflow, a number of competing designs were considered. One common approach is to introduce a passive aerodynamic device, an air-duct between the front grille opening and the CRFM. However, as can be seen in Figure 2.8, this compact vehicle model has very little room between the bumper beam reinforcement and the condenser core making the gap between the upper part of the air-duct and the CRFM very tight. This may render the air-duct configuration even less efficient than the baseline one. To overcome this potential drawback, the space between the air-duct and upper part of the condenser needs to be increased. Considering the space limitations around the CRFM (see Figure 2.9, left), the only possible approach is to incline the CRFM by keeping the top fixed and moving the bottom rearward (see Figure 2.9, right). As such, all air-duct cases have an air-duct between the front grille opening and an inclined CRFM. To demonstrate the effectiveness of such a design, the delta streamwise velocity between case 6, with an air-duct, and the baseline case 1, ($\Delta U_{6,1} \equiv U_{\text{Case 6}} - U_{\text{Case 1}}$) is presented [1] in Figure 2.10 . It is evident that the velocity in the upper part of the radiator increased significantly when compared with the baseline case. The impact of this improved design on the cooling airflow, and the comparison between different air-duct and grille opening designs will be discussed next.

[1] In this paper, the notation A_{m} will imply the value of a flow property A obtained from the case m; the notation $\Delta A_{\text{m,n}}$ will imply the difference in the values of the flow property A obtained from cases m and n, i.e. $\Delta A_{\text{m,n}} \equiv A_{\text{m}} - A_{\text{n}}$.

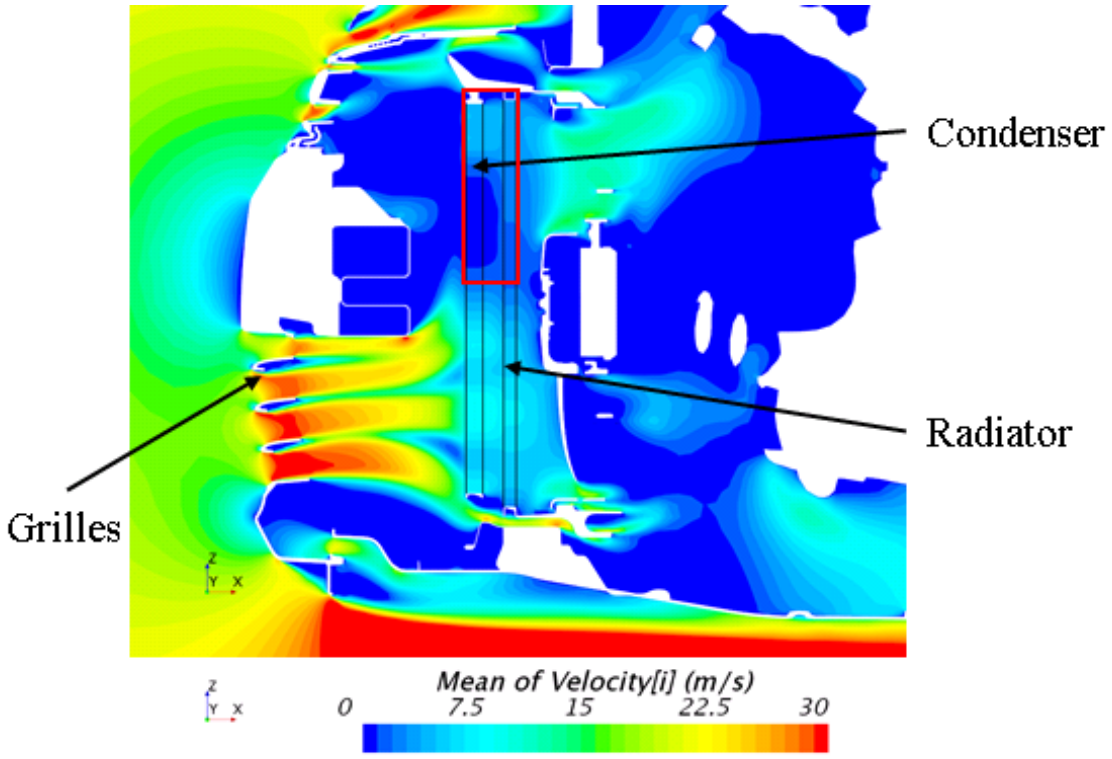

Figure 2.8: Stream-wise velocity on the central plane through the CRFM at highway speed with fan off configuration for the baseline case.

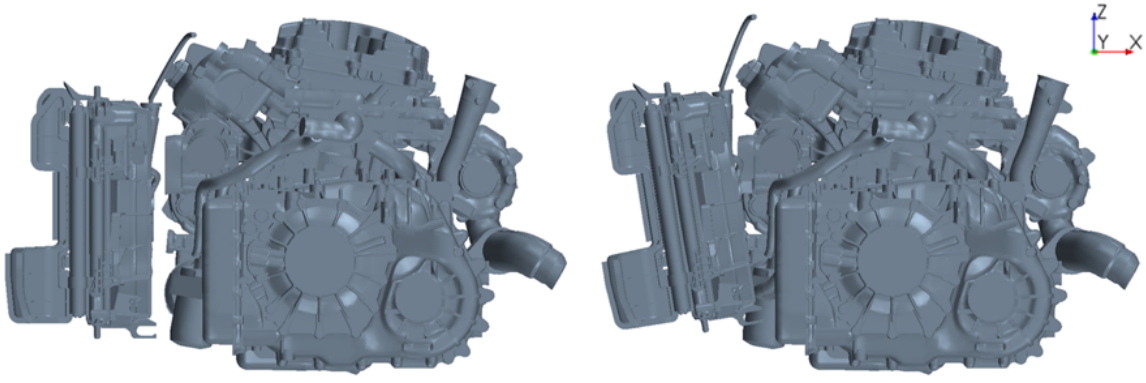

Figure 2.9: Side views of the CRFM and the engine block. Left: Case 1 with a vertical baseline CRFM; Right: Case 6 with a 9 degree inclined CRFM. See section 3.2 for a summary of differences between the two cases.

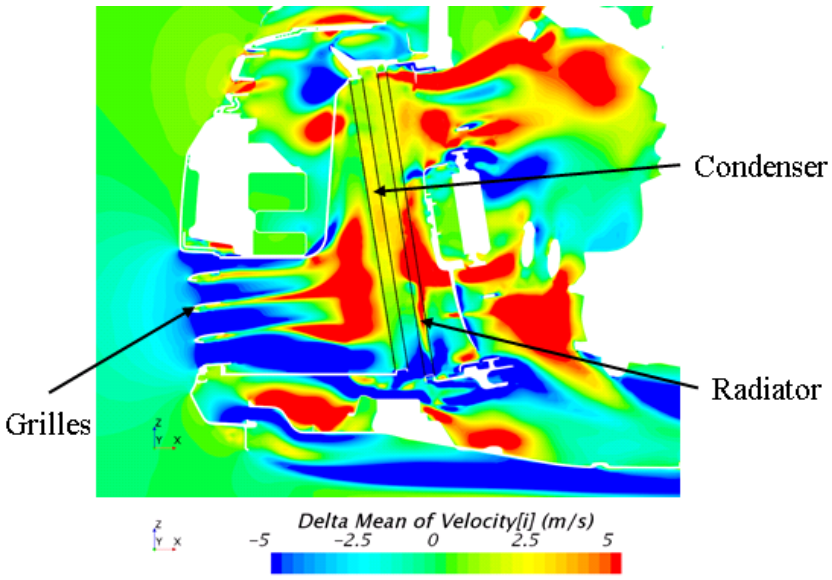

Figure 2.10: Delta streamwise velocity ($\Delta U_{6,1}$) on the central plane through the CRFM at highway speed with fan off configuration; see the footnote 1 for the definition of Delta streamwise velocity $\Delta U_{6,1}$.

2.5.2 Expected Radiator Performance

As stated earlier, the effectiveness of a radiator depends primarily on three parameters, i.e. the mass of airflow, the airflow uniformity and the airflow temperature (referring to hot air recirculation phenomenon in vehicle idle condition). Typically, at highway speeds, while the mass of airflow entering the underhood area is often more than sufficient, the actual amount and uniformity of the airflow passing the radiator are often quite low. The excessive airflow entering through the front grille opening will add to the cooling drag, hence the total vehicle drag. The quality of the airflow, namely the amount and uniformity, passing through the radiator may lower its performance and efficiency. Thus, one of the challenges for underhood airflow management at highway speeds is to increase the airflow rate and uniformity through the radiator without increasing the total airflow in the underhood area. To achieve this objective, airflow through both the grille opening and radiator inlet were investigated in this study. At low vehicle speeds or idle condition, since the only main driving source for

cooling airflow is the cooling fan behind the radiator, the main challenge becomes to deliver sufficient airflow through the radiator and minimize the hot air recirculation phenomenon at the same time. In this study, the challenges at both highway speeds and idle conditions were investigated, and a solution is proposed which satisfies the requirements of both driving conditions.

2.5.2.1 Underhood Flow at Highway Speed

The air flow rate ($\dot{Q}$) in m^3/hr through the front grille opening and radiator inlet at highway speed for all cases except for the mock-up case (case 2) are tabulated in Table 2.1. For better apprehension, the absolute value of the volume flow rate is tabulated for the baseline case or case 1 only ($\dot{Q}_1$), while the air flow rates corresponding to cases 3–6 are presented relative to the case 1. Following the definition given in footnote 1 these flow rates are expressed as $\Delta\dot{Q}_{n,1}$ where n stands for the case number. At both *fan off* and *fan on* conditions, the introduction of the air duct causes a significant increase in airflow through the radiator inlet in spite of an even larger decrease in airflow through the grille opening. This shows a remarkable effectiveness of the air-duct in delivering a larger volume cooling flow to the CRFM. Case 4, the narrow air-duct case with side-grilles sealed off, shows the highest decrease of 41% and 32.8% of flow through the front end at fan off and fan on conditions respectively. For flow through the radiator, case 6 with a sealed grille and 35 degree air-duct, gives the best result at both fan on and off conditions with approximately 34% and 22.5% air flow increases respectively. Two further observations are: (a) while fan suction can increase the airflow through the front grille opening and radiation inlet, it does not affect the conclusion drawn for each case, (b) side-grilles sealing can reduce the airflow through the grille opening, and it also causes a slightly higher airflow through the radiator inlet. The latter can be seen by comparing cases 3 and 5 (with side-grilles open) with cases 4 and 6 (with side-grilles sealed off) respectively.

One needs to have an understanding of the flow-field characteristics corresponding

Table 2.1: Cooling air flow rates in (m^3/hr) through the front grille opening and radiator at highway speed (70 mph) corresponding to cases 1, and 3–6. Note that the volume flow rates for cases 3–6 are relative to case 1.

	Fan Condition	$\dot{Q}_1$	$\Delta\dot{Q}_{3,1}$	$\Delta\dot{Q}_{4,1}$	$\Delta\dot{Q}_{5,1}$	$\Delta\dot{Q}_{6,1}$
At grille opening	Fan off	5760	-1274	-2362	-1648	-2294
	Fan on	5913	-883	-1937	-1206	-1835
At radiator inlet	Fan off	2107	595	680	612	731
	Fan on	2939	527	578	578	663

to the baseline configuration in order to properly analyze the influence of the air-duct and front-end sealing on the underhood flow. For that matter, the baseline case streamwise mean velocity, U, through the middle of the lowest grille opening (see red line in Figure 2.5) is shown in Figure 2.11. It can be seen that a high velocity stream enters through the front grille opening which slows down very fast before going through the CRFM. In addition, a good portion of the high velocity stream enters the underhood area, but does not serve the purpose of cooling as it does not pass through the CRFM; this overflow air is likely to cause more cooling drag.

In order to visualize how the air-duct and front-end sealing impact the underhood flow-field, contours of $\Delta U_{m,1}$, where U and m are the mean streamwise velocity and case number respectively, on a $x-y$ plane through the middle of the lowest grille are shown in Figure 2.12; please refer to the red line in Figure 2.5 for the location of this plane with respect to the vehicle geometry. Note that in these figures, the blue and red colors indicate respectively whether the flow is slower or faster compared to the baseline case. Clearly, as also noted in Table 2.1, there is a significant decrease in flow through the grille opening for air-duct cases as demonstrated by the large deep blue regions. This decrease is possibly due to the fact that the air-duct restricts the volume of spillage/leakage air flow. As indicated by large red regions in front of the condenser, all of the air-duct cases show noticeably increased airflow through the heat-exchangers

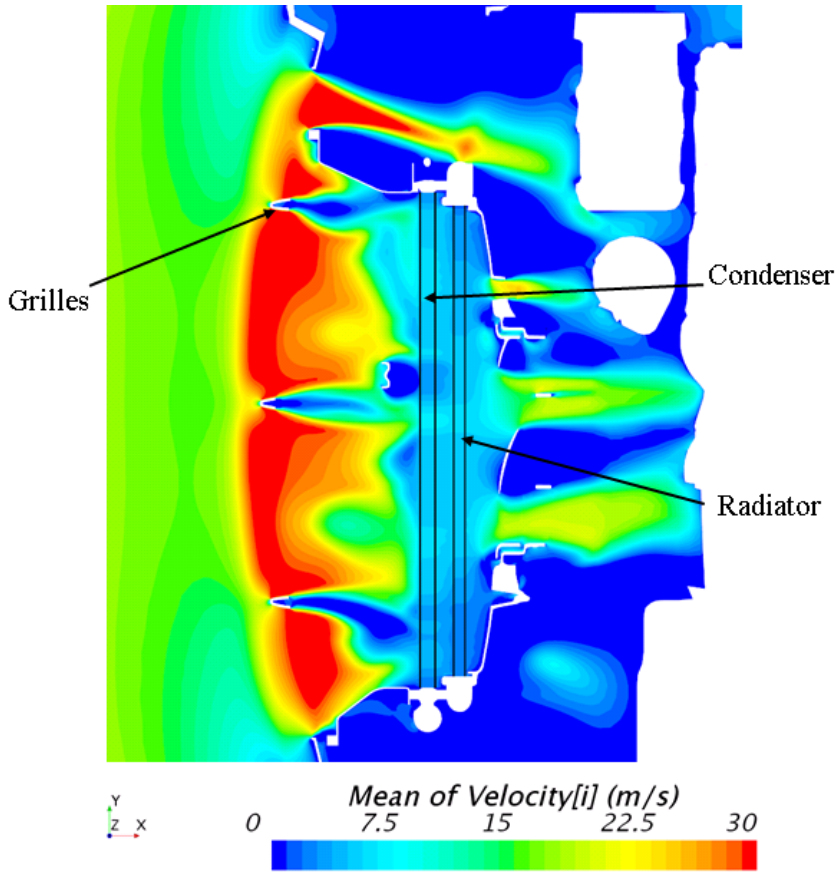

Figure 2.11: Stream-wise velocity (U) distribution on a plane through the middle of the lowest grille for case 1 at highway speed and fan off condition; see the red line in Figure 2.5 for the location of the plane.

(HX). However, the honeycomb structures inside the radiator and condenser limit the maximum flow through the HX. The combined effect is a reduction in the total airflow entering the underhood region through the grille-opening. For cases with side-grilles open, while a lower velocity at the air-duct entrance is achieved, there are still high velocity streams going through both sides of the grille opening; see images (a) and (c). On the other hand, for cases with side-grilles sealed off, not only the velocity at the air-duct entrance is further decreased, excessive airflow entering through both sides of the grille opening is also eliminated as can be seen in images (b) and (d). In summary, the air-duct can increase airflow through the radiator and reduce the airflow through the grille opening at highway speeds simultaneously, and the effectiveness is best achieved with a wider air-duct as evidenced from the results of Case 6.

2.5.2.2 Airflow Distribution over the Radiator Upstream Surface

The presence of the bumper reinforcement and other front-end structural components often makes the air-flow past the grille-opening highly non-uniform. As shown by Kubokura et al. [11], the heat rejection performance of a radiator with non-uniform airflow could be 10% lower than that with an ideal uniform airflow even though the average velocity is the same. Therefore, in addition to ensuring a sufficient airflow to the CRFM, the airflow uniformity should also be given attention too. For the vehicle model used in this study, only one grille opening aligns with the bottom part of the CRFM. Thus, one may speculate that for the baseline model, the situation of airflow non-uniformity could be fairly severe. While it is shown that the air-duct can help to deliver a larger volume of air to the CRFM, one can expect that it will also improve the airflow uniformity at the radiator inlet since it directs more airflow to the upper part of the radiator as can be seen in Figure 2.10. To verify this quantitatively, an analysis of the airflow distribution at the radiator inlet surface was conducted by using the parameter uniformity index γ (see Eq. 2.1 - 2.3). Since the CRFM is inclined in all air-duct cases, to make a meaningful comparison with the baseline case, a local

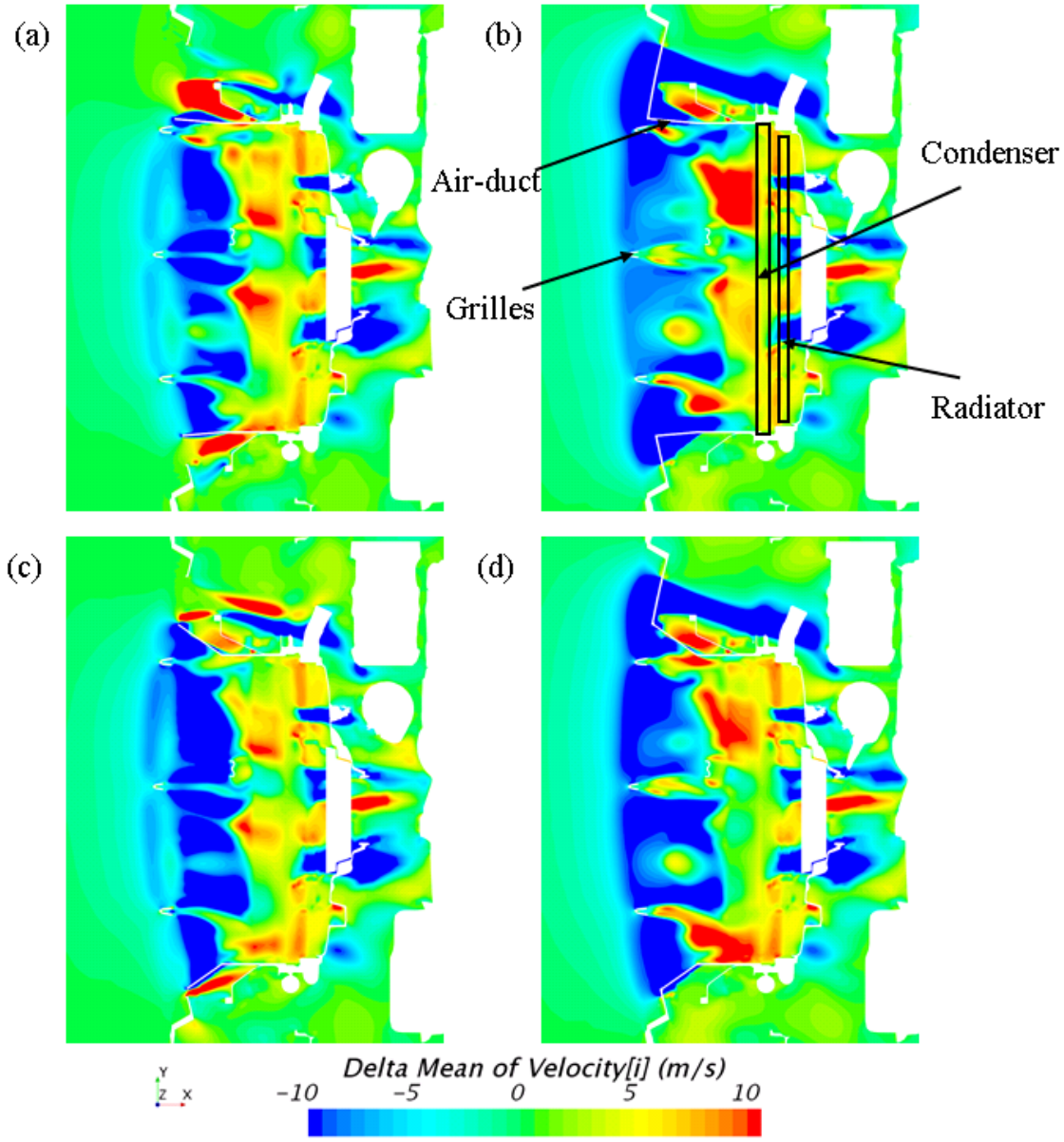

Figure 2.12: Distribution of delta streamwise velocity $\Delta U_{m,1}$ on a $x-y$ plane through the middle of the lowest grille at highway speed and fan off condition; images (a) - (d) represent cases 3-6 respectively.

coordinate system aligning with the edges of the radiator was used to calculate the uniformity index.

Table 2.2 shows the airflow uniformity index over the radiator inlet surface for all cases at all three operating conditions, viz. fan on and off at 70 mph, and fan on at idle. Note that while the uniformity index for the baseline case γ_1 is given as an absolute value, the uniformity indices for the rest of the cases are presented as relative to the case 1, i.e as $\gamma_{m,1} \equiv \gamma_m - \gamma_1$. At the highway speed, all of the air-duct cases show significant improvement of the uniformity index when compared to the baseline case at both fan operating conditions. Interestingly, by comparing cases 3 and 4 with cases 5 and 6, it can be concluded that open side-grilles provide better uniformity indices compared to the sealed-off ones. This is in contrast to the results of airflow rate through the radiator inlet, which show that the cases with side-grilles sealed off perform better. This implies that the cold-flow analysis based prediction of HX performance will be rather inconclusive. However, comparing cases 4 and 6 in terms of both air-flow volume and uniformity, it is clear that a wider air-duct would result in a better HX performance. In addition, fan operation generally increases the uniformity index for all cases. Secondly, for the idle condition, a slight decrease in uniformity index is observed in all air-duct cases. This is likely due to the fact that the airflow can be driven to the upper part of the radiator directly from the surrounding in the baseline case. However, for the air-duct cases, the airflow through the radiator must come only from the air-duct entrance which aligns with the bottom part of the radiator only. However, without considering the hot air recirculation phenomenon, which is a common problem at low speed and idle condition, it is too early to draw any conclusion here. Further discussion will be presented in the next subsection.

To help understand how the air-duct improves the flow uniformity over the radiator surface, streamwise velocity distributions on the radiator inlet surface at the highway speed with both fan off and on conditions for the baseline case are shown in Figure

Table 2.2: Tabulated values of airflow uniformity index γ over the radiator inlet surface.

Operating Conditions	γ_1	$\Delta\gamma_{3,1}$	$\Delta\gamma_{4,1}$	$\Delta\gamma_{5,1}$	$\Delta\gamma_{6,1}$
70 mph Fan off	0.338	0.113	0.076	0.109	0.094
70 mph Fan on	0.458	0.084	0.052	0.09	0.074
Idle Fan on	0.584	-0.037	-0.050	-0.015	-0.024

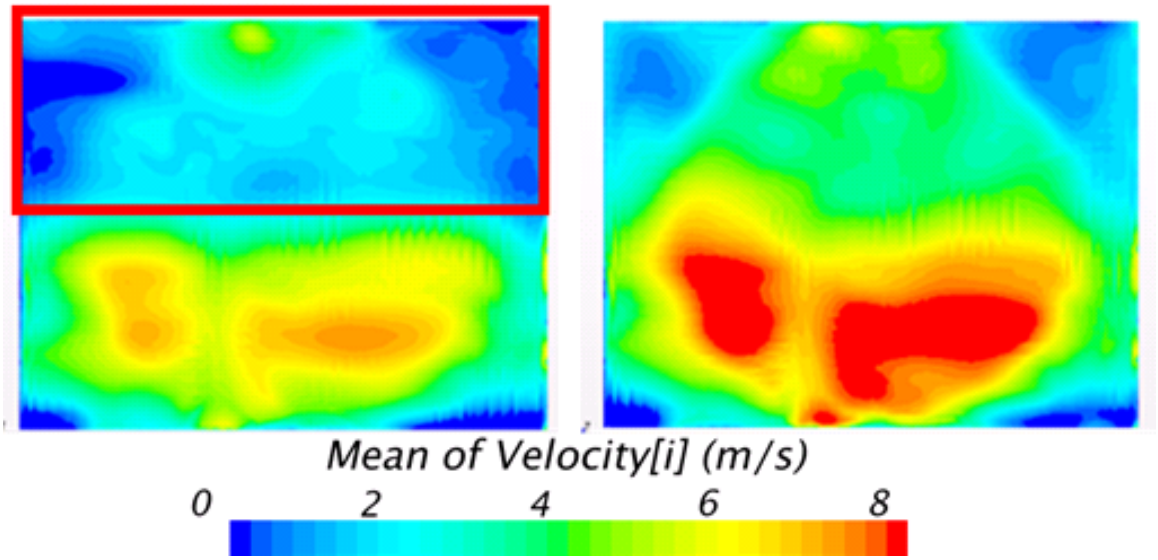

Figure 2.13: Baseline case streamwise mean velocity distributions on the radiator inlet surface at 70 mph with fan off (left) and fan on (right) conditions.

2.13. The left image shows that the velocity on the upper part of the radiator is very low (marked with a red rectangle). Figure 2.13 (right) shows that the fan operation improves both the flow rate and flow distribution, which is consistent with the quantitative analyses. Contour images of the delta streamwise velocity distribution ($\Delta U_{m,1}$) on the radiator inlet surface for all air-duct cases are shown in Figure 2.14 at highway speed for both fan operating conditions. While little difference can be seen between the air-duct cases at either fan condition, clear improvements, especially on the upper part of the radiator, can be observed in all air-duct cases when compared with the baseline case.

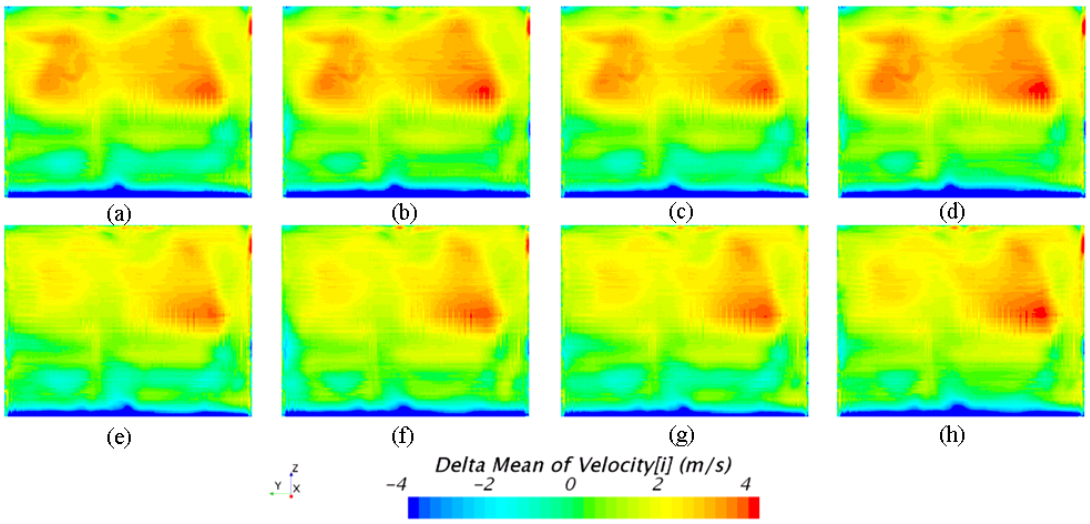

Figure 2.14: Contours of Delta streamwise velocity relative to the baseline case, $\Delta U_{m,1}$, over the radiator inlet surface at 70 mph with fan off (top) and on (bottom) conditions; from left to right, the images represent cases 3–6 respectively.

2.5.2.3 Underhood Hot Air Recirculation at Vehicle Idle Condition

Vehicles are generally driven at very low speeds on urban roads during the peak hours. These vehicles are subject to frequent stops at traffic lights, and they often stay idle for long periods of time in heavy traffic. At such conditions, the cooling fan behind the radiator drives the airflow through the CRFM. This operation will decrease the pressure upstream of the fan which could bring in a certain amount of hot air from the engine bay to the plenum through the bypass channels. This phenomenon is called the *underhood hot air recirculation*, which would be detrimental to the performance of the A/C system. Moreover, this problem could be quite severe under certain circumstances, such as during hot summer days when the ambient air temperature is very high. The airflow rate through both the front grille and radiator at vehicle idle condition is listed in Table 2.3. Like Table 2.1, only the airflow rate for case 1 is expressed in the absolute unit (m^3/hr) while the rest are expressed relative to the case 1, i.e. $\Delta\dot{Q}_{m,1}$. For the baseline case, the airflow through the radiator inlet

Table 2.3: Airflow (m^3/hr) through the front grille opening and radiator during idling.

	$\dot{Q}_1$	$\Delta\dot{Q}_{3,1}$	$\Delta\dot{Q}_{4,1}$	$\Delta\dot{Q}_{5,1}$	$\Delta\dot{Q}_{6,1}$
Grille opening	612	510	561	544	612
Radiator inlet	1529	-85	-119	-34	-68

is more than double of that through the grille opening. This implies that 60% of the cooling airflow through the radiator is actually hot air recirculated from the engine bay. In contrast, for all the air-duct cases, while the flow rate at radiator inlet is slightly lower when compared with the baseline case, the airflow through the radiator inlet is only slightly higher than that through the grille opening. For example, in case 6, the volume flow rate at the grille-opening and radiator are 1224 and 1461 m^3/hr respectively. This means that less than 20% hot air recirculation; nevertheless, the air-duct cases shows approximately a hundred percent improvement in fresh airflow at the grille-opening. To verify this further, velocity fields on a plane through the top part of the CRFM are shown in Figure 2.15 for cases 1 and 6. Hot air recirculation can be clearly seen on the left image which represents baseline case (see areas marked by a red ellipse), while the right image shows that the recirculated airflow is blocked by the air-duct. Subsequently, even though the baseline case shows better results in terms of the airflow rate at the radiator inlet and flow uniformity over it, the heat rejection performance of the radiator is likely to be worse for this case.

2.5.3 Cooling Drag Assessment

Normalized cooling and total drag coefficients at vehicle speed 70 mph for all cases investigated with both fan on and off conditions are shown in Table 2.4. Like the previous tables, only the coefficients corresponding to the baseline case are expressed as absolute values, while those corresponding to cases 3–6 are expressed relative to case 1. Clearly, all of the air-duct cases cause significant reductions in both cooling and total drag. The drag reduction could come from two primary factors. Firstly, the air-ducts causes significantly less airflow entering the underhood area, with case

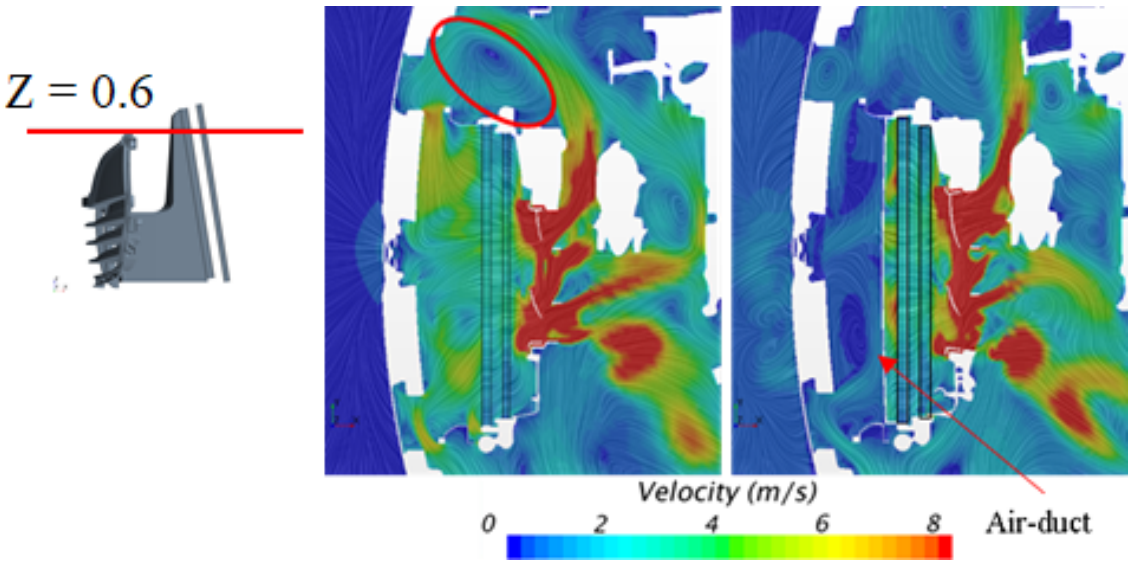

Figure 2.15: Flow distribution on $Z = 0.6$ m plane; left: case 1; right: case 6.

4 having the highest drop of 41% in airflow volume. This reduction in cooling airflow volume would certainly help to reduce the cooling drag, hence the total vehicle drag. Secondly, as a result of less airflow entering the underhood area in air-duct cases, we speculate that there will be less airflow exiting to wheelhouse and under-body, which may lead to less interference drag. To verify this speculation, two underhood plane sections, one behind the engine block and the other behind the front wheel (see Figure 2.16), were selected to measure the airflow rate for case 1 and 6. The computed airflow rates on these two plane sections are presented in Table 2.5. As can be seen, case 6 (with air-duct) gives significantly less airflow at both plane sections when compared to the baseline case. As speculated before, by removing excessive flow entering the underhood area, cases with side-grilles sealed, case 4 and 6, have lower drag values than cases with side-grilles open, case 3 and 5, respectively. While case 4, with a narrow opening air-duct, performs best at the fan-off condition, case 6, with a wide opening air-duct, shows the best performance for the fan-on condition.

It has been confirmed by several works that the cooling flow is strongly affected by the wheel rotation ([45]). The streamwise velocity U distribution on a plane at

Table 2.4: Cooling drag and total drag coefficients at vehicle speed 70 mph (see footnote 1 for the definition of notation).

	Fan Condition	Case 1	$\Delta_{3,1}$	$\Delta_{4,1}$	$\Delta_{5,1}$	$\Delta_{6,1}$
Total drag coefficient	Fan off	0.326	-0.016	-0.024	-0.015	-0.020
	Fan on	0.320	-0.017	-0.021	-0.016	-0.026
Cooling drag coefficient	Fan off	0.035	-0.016	-0.024	-0.015	-0.020
	Fan on	0.031	-0.017	-0.021	-0.016	-0.026

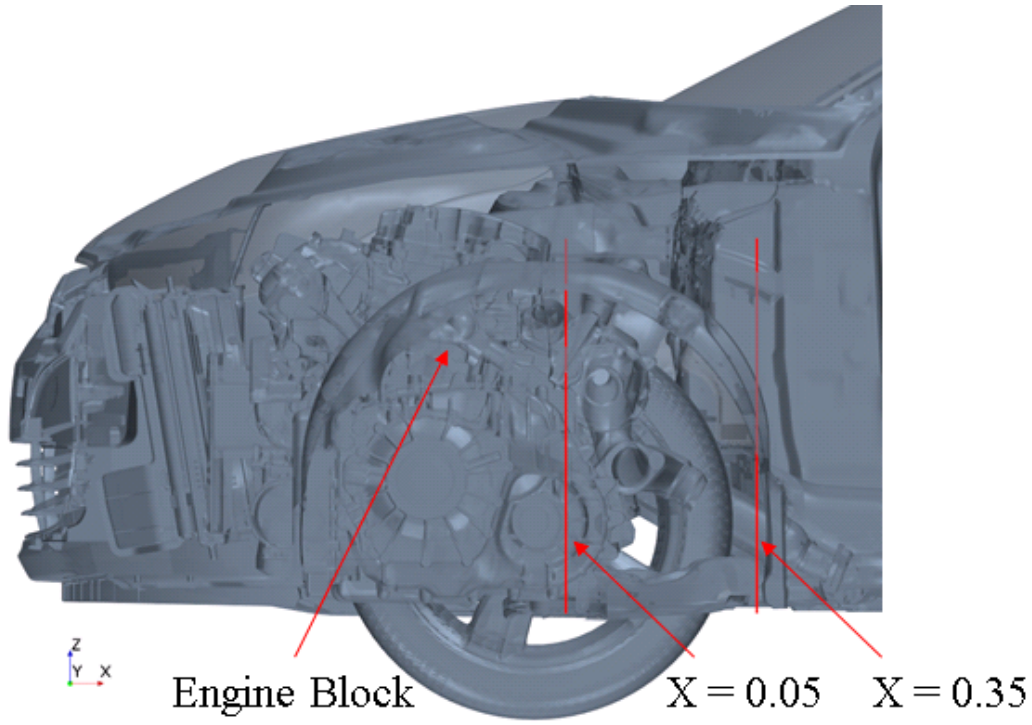

Figure 2.16: Plane sections for measuring underhood airflow volume rate.

Table 2.5: Cooling air flow rates in (m^3/hr) through two underhood plane sections (see Figure 2.16) for case 1 and 6 at highway speed (70 mph) fan off condition.

Airflow rate	$\dot{Q}_1$	$\Delta\dot{Q}_{6,1}$
At X = 0.05	4545	-1770
At X = 0.35	3558	-945

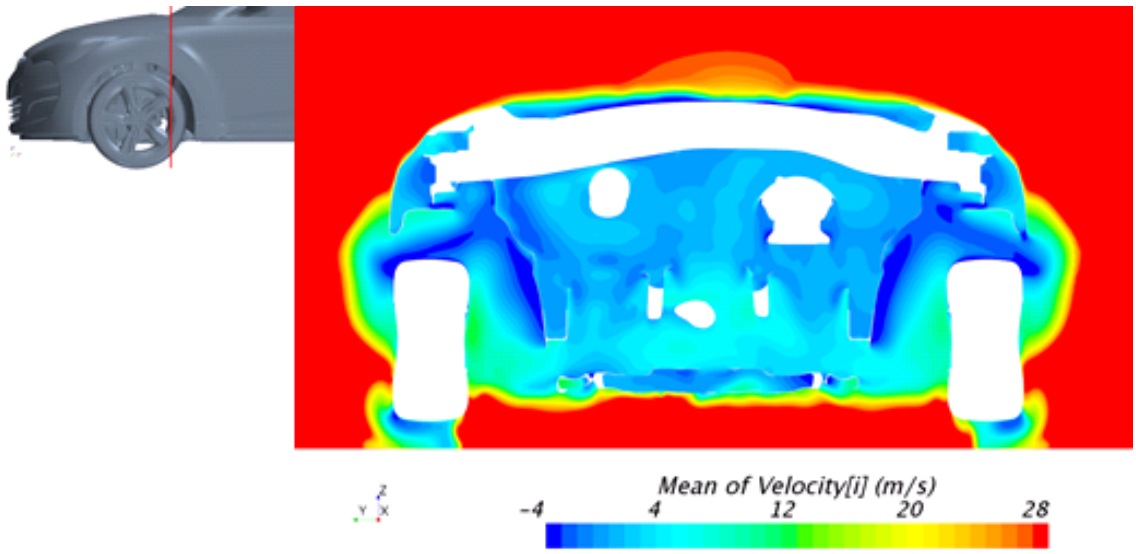

Figure 2.17: Distribution of streamwise velocity (U) on plane $x = 0.215$ for case 1 at vehicle speed 70 mph and fan off condition.

$x = 0.215$ (front wheel center is at $x = 0$) at 70 mph and fan off condition for case 1 is shown in Figure 2.17, noticeable reverse flow can be seen in the wheel housing region. The delta streamwise velocity $\Delta U_{6,1}$ for case 6 is shown in Figure 2.18, the red color around the wheel housing region indicates less severe reverse flow. This might be due to less airflow going into underhood in air-duct cases. Consequently, the cooling drag is reduced in air-duct cases.

To help understand the development of the total vehicle drag, the accumulated drag coefficient plots for cases 1, 2 and 6 at vehicle speed 70 mph and fan off condition, are shown in Figure 2.19. Clearly, all the cases show a similar trend beyond the cowl area implying that the difference in the total drag is mainly caused by the cooling flow. The higher initial drag for case 2 is due to a larger front stagnation region caused by the closed-off grille opening. However, as there is no or negligible underhood flow, the cooling interference drag is zero, and hence we see a gradual decrease in the accumulated drag. The same argument can be used to explain why the case 6 with side grilles-sealed off shows initially a higher accumulated drag which gradually

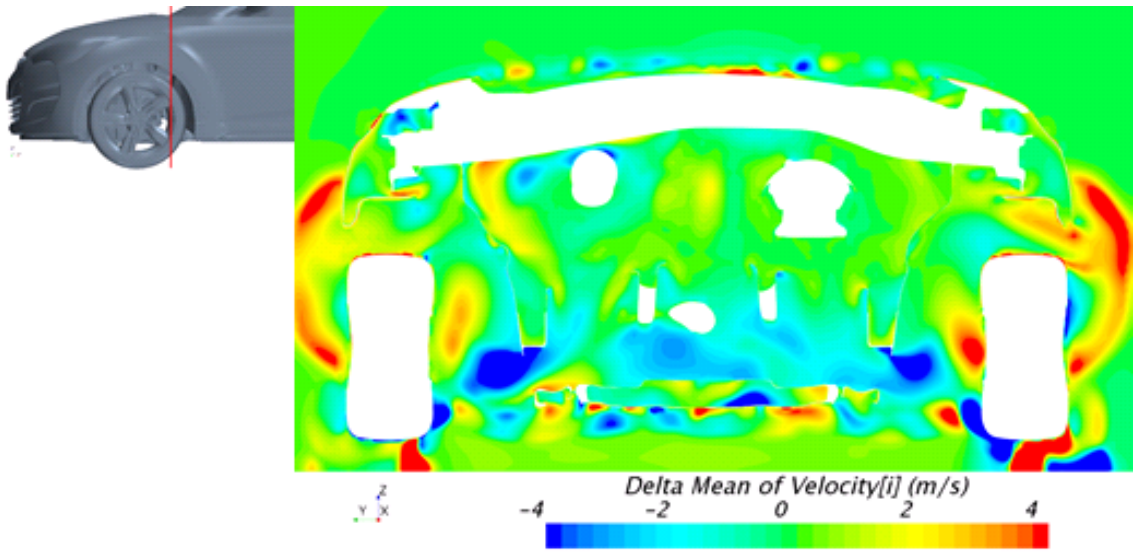

Figure 2.18: Distribution of delta streamwise velocity ($\Delta U_{6,1}$) on plane $x = 0.215$ for case 6 at vehicle speed 70 mph and fan off condition.

tapers off.

As a final note, the authors recognize that simulating the highway driving fan operation scenario for a real passenger vehicle in CFD is very challenging as, during this drive cycle, the fan is normally neither stationary nor rotating at 2000 rpm, rather the cooling fan is in a windmilling situation.

Based on both the radiator performance and cooling drag assessment, case 6 (35 degree air-duct with grille-sides sealed) is the best design in terms of improving radiator performance and reducing cooling drag.

2.6 Conclusion

Aerodynamic analyses of radiator performance and cooling drag for a real full-scale car with various front-end configurations were conducted using 3D CFD simulations. Quantitative analysis and flow visualization based explanations for observed phenomena are presented to show how passive aerodynamic devices and front-end modifications can improve a road vehicle's aero-thermal performance.

It has been shown that a vertical CRFM for the investigated car configuration has

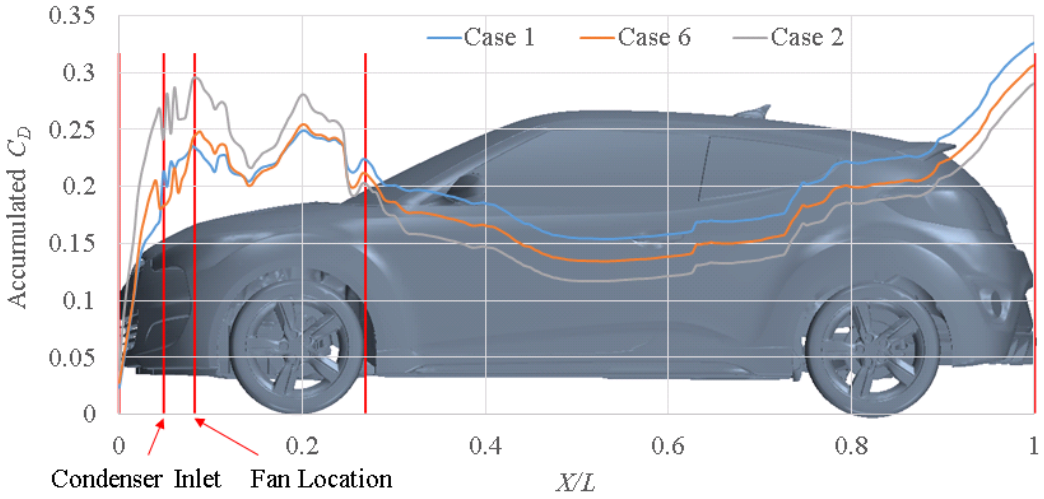

Figure 2.19: Accumulated drag coefficient plots for case 1, 2 and 6 at vehicle speed 70 mph and fan off condition. Where L represents the overall vehicle length.

a poor radiator performance and high cooling drag. However, we have demonstrated that the underhood airflow can be optimized by introducing an air-duct, in combination with an altered orientation of the CRFM and modified grille openings. This configuration results in a superior performance at both highway speeds and idle conditions. Specifically, at highway speed, an air-duct design can improve the cooling performance of the radiator by increasing the flow rate and airflow uniformity over the upstream surface. In addition, a wider air-duct performs better than a narrow one under this condition. At vehicle idle condition, the air-duct can attenuate the hot-air recirculation problem significantly, which could result in a notable improvement of heat exchanger performance, primarily that of the condenser. Moreover, the air-duct design also can reduce the cooling drag, hence the total vehicle drag, due to significantly lesser airflow entering the underhood area. Further, by reducing the excessive airflow that does not contribute to the cooling purpose, the sealed-off side-grilles could reduce the cooling drag even more. Consequently, a combination of side-grille sealing with a wide air-duct can achieve a notable improvement of the underhood airflow management, in terms of both the radiator performance and ve-

hicle total drag, and, thus, will improve the overall fuel economy. However, we have recognized that the cold-flow based CFD simulations can be inconclusive for radiator performance as some designs can show an increase in volume flow rate, but a decrease in flow uniformity and vice versa implying that aerodynamic analysis with heat transfer needs to be carried out before making the final design call.

CHAPTER 3: Investigation of the Turbulence Modeling Effects on the CFD Predictions of Flow over a Passenger Road Vehicle

3.1 Abstract

Computational Fluid Dynamics (CFD) has now become one of the main tools for investigating the aerodynamics of road vehicle in both industries and academia. In practice, RANS (Reynolds Averaged Navier-Stokes) approaches are still widely used turbulence models in automotive industries, due to their acceptable accuracy and affordable computational resource cost for predicting flows involving complex geometries. However, it is well known that for automotive flows, RANS turbulence models often fail to capture the absolute flow features or even integral flow quantities, instead, they are used to assess the magnitude and direction of a trend. Moreover, even for such purpose, notable disagreements often exist between results predicted by different RANS models. Thanks to fast advances in computer technology, increasing popularity has been seen in the use of the hybrid LES/RANS (Large Eddy Simulation/Reynolds Averaged Navier-Stokes) approaches which have demonstrated the high potential of being more accurate and informative than RANS approaches. Whilst evaluations of RANS and hybrid LES/RANS models on various applications are abundant in literature, such evaluations on full-car models are relatively fewer. In this study, four widely used RANS models in the automotive industry, i.e., the realizable $k-\epsilon$ two-layer, AKN $k-\epsilon$ Low-Reynolds, SST $k-\omega$, and V2F model will be evaluated on a full-scale passenger vehicle with two different front-end configurations. In addition, both cases will be run with two DES models to assess the differences between the flow predictions obtained using these two approaches.

3.2 Introduction

CFD has played an important role in the early design stages of modern-day vehicles. In practice, RANS modeling still remains as a widely used approach in automotive industries, due to its acceptable accuracy, affordable cost, and fast turnaround time. However, due to the well-known drawbacks of RANS models for predicting complex separated flows, the DES, and its variants have started to gain popularity. As demonstrated by many researchers [60, 61, 62], DES models generally offer an advantage over RANS models in predicting the flow field and integral quantities. Unfortunately, they still could not correctly capture flow details and cost significantly more computational resources. For example, for a DrivAer vehicle, the DES simulation is 17 times more expensive than the RANS computation [61].

In RANS approaches, the entire turbulence spectrum is approximated through a set of transport equations to solve the time-averaged mean flow field. These equations were established during the past several decades based on empiricism, mathematical analysis, and physical reasoning of the key mechanisms observed in canonical flows. RANS models have enjoyed remarkable success in various industrial applications. However, the inability of RANS models to correctly predict complex separated flows has motivated researchers to develop and apply higher-order models in industrial applications. One promising model is the DES approach. DES is a hybrid modeling approach which combines the best of both RANS and LES: a RANS simulation in the boundary layers and a LES in the unsteady separated regions.

One problem of the DES approach is the spurious buffer layer between the RANS and LES regions [63, 64]. Spalart et al. [65] proposed Delayed Detached Eddy Simulation (DDES) to prevent DES from a too early switch to LES mode. Another modification is called Improved Delayed Detached Eddy Simulation (IDDES) proposed by Shur et al. [27]. IDDES allows RANS to be used in a much thinner near-wall region and could provide some WMLES (Wall-modelled LES) capabilities to the DES

formulation.

The literature contains a vast amount of works on the evaluation of RANS and DES models for various flow configurations. Due to the scope of this study, only validation studies related to automotive flows will be introduced in this paper.

Due to the complexity and proprietary nature of the works associated with production passenger vehicles, the evaluations of turbulence models on full-scale vehicles are rare. Instead, researchers have mainly focused on simplified, generic car geometries, such as the Ahmed body and the more recently introduced DrivAer model. The Ahmed body was introduced in 1984 to analyze the key flow field features of ground vehicles [66]. Ahmed body comprises a flat front with rounded corners and a sharp slanted rear upper surface with various angles. Since ground vehicles can be viewed as bluff bodies moving in the close vicinity of the road, the broad aerodynamic features of the Ahmed body resembles a ground vehicle, e.g. the flow separation on the rear window or the wake structure behind the body. Ahmed body has been extensively studied by using both experimental and numerical methods. Until recently, it has been the most widely used subject for evaluation works on turbulence models related to automotive flows.

For the Ahmed body, the main model variable is the rear slant angle. The flow patterns on the rear slant and behind the body vary as the slant angle changes. A vast amount of works have investigated the influence of the slant angle on the flow patterns. It was first shown by Ahmed et al. [66] in his introduction work of the Ahmed body that 30 degree is the critical slant angle at which the topology of the flow is suddenly altered and the drag is reduced noticeably. Above this angle, the flow fully separates over the slant starting from its sharp edge due to the strong adverse pressure gradient between the slant and the roof. For such configurations, RANS models succeed in predicting the correct separation region and give good agreement with the experimental data [61]. Below the critical angle, especially at 25 degree, the

flow is most complex. The flow still separates from the slant but the pressure gradient between the slant area and the side walls is still strong enough to generate streamwise counter-rotating vortices at the lateral slant edges. These vortices induce a downward motion over the slant, mainly in the downstream part of the slant. Consequently, the flow which partially detached from the upstream part of the slant can reattach further downstream, thus a confined recirculation zone is formed over the rear slant. Moreover, the wake structures, which are dominated by the interactions between the separation zone and strong counter-rotating vortices, become very complex in this configuration. These vortices are also responsible for the high induced drag. The 25 degree slant angle is the most extensively studied since it still poses a significant challenge for the numerical simulations. As demonstrated by [67, 68, 69, 70], the majority of RANS models fail to predict the flow field correctly. They either predict no separation, or they can not predict the correct size of the separation zone. This is even challenging for higher order models such as LES and hybrid LES/RANS [71]. For even smaller slant angles, i.e. smaller than 12 degree, the flow is fully attached on the rear slant and only separates over the rear end of the body. For such simple flow patterns, most RANS models again perform very well in terms of both integrated quantities and flow structures [72]. To sum up, for the Ahmed car body the performance of various turbulence models, especially RANS models, is highly influenced by the geometry and flow topology present. This raises the potential uncertainty in predicting automotive flows when using numerical approaches, especially RANS approaches.

More recently, a new realistic generic car model called DrivAer model was proposed by the Institute of Aerodynamics and Fluid Mechanics of the Technical University of Munich (TUM), in cooperation with BMW and Audi AG. The DrivAer model consists of three typical car configurations, i.e. estate, fastback, and notchback. All three of these configurations have been experimentally investigated to provide data for numerical comparison [73, 74]. TUM also investigated the fastback configuration

numerically using the SST $k-\omega$ model [75]. They found that although there are good agreements for drag coefficients between experiment and simulation, obvious discrepancies of pressure distributions on the top and bottom of the car exist between simulation and experiment results. A recent work, which presented structured finite difference solutions that are more accurate by using overset grids and NASA's overset grid solver, Overflow [76], also observed similar pressure distribution differences when using the SST $k-\omega$ model. Moreover, several widely used RANS and Hybrid LES/RANS models were also applied to DrivAer model [77, 61, 60, 78]. It was found that RANS models were unable to correctly predict the force coefficients, especially the lift coefficient. In addition, they found while inaccuracies still exist when compared to the experimental data, Hybrid approaches predicted both the force coefficients and flow field with much improved accuracy but at the expense of much higher computational cost. The evaluations of turbulence models on full-car geometries are quite rare. A recent work presented a study of RANS turbulence models on the prediction of aerodynamic characteristics of a NASCAR Gen-6 Cup racecar [79]. Discernible differences of the flow features in the wake of the car was observed between the results of different RANS model in this study.

The goal of the current study is to provide evaluation works of several RANS models and DES variants on a full-scale passenger vehicle to the automotive community. The RANS models investigated are very commonly used in the automotive industry, i.e., the realizable $k-\epsilon$ two-layer, AKN $k-\epsilon$ Low-Reynolds, SST $k-\omega$, and V2F model. The DES variants studied are the DDES and IDDES. The predictions differences on two vehicle configurations between those turbulence models were analyzed in terms of integral forces, pressure and velocity field, and turbulent kinetic energy.

3.3 Simulation Details

3.3.1 Turbulence Models

Four commonly used RANS models and two DES variants were investigated in this study. These include:

- RANS models
  - Realizable $k-\epsilon$ model (RKE) of [21]
  - AKN (Abe-Kondoh-Nagano) Low-Re $k-\epsilon$ model (AKN) of [22]
  - V2F $k-\epsilon$ model (V2F) of [23]
  - SST $k-\omega$ model (SST) of [24, 25]
- DES variants
  - Delayed Detached Eddy Simulation (DDES) of [26]
  - Improved Delayed Detached Eddy Simulation (IDDES) of [27]

RKE, AKN, and V2F are formulated based on the standard $k-\epsilon$ model. One of the main flaws of the standard $k-\epsilon$ model is that it may predict an anomalously large growth of the turbulent kinetic energy (TKE) in stagnation point flows. The usual explanation for the stagnation point anomaly is that the linear eddy viscosity formulation gives an erroneous difference in normal stresses. The stagnation anomaly can be ameliorated by imposing the "realizability" constrain on the normal stresses. [28, 29]. All the three $k-\epsilon$ models investigated in this study have applied the realizability. While AKN and V2F implement the realizability through turbulent time scale, RKE enforces the realizability by damping functions.

One of the main differences between these three $k-\epsilon$ models is the way they are applied in the viscous-affected layer (including the viscous sub-layer and the buffer layer). AKN uses the Low-Reynolds number approach by applying damping functions

to some of the coefficients in the model. RKE adopts a Two-Layer approach [30], which solves for turbulent kinetic energy k but prescribes turbulent dissipation rate ϵ algebraically with distance from the wall in the viscosity dominated near-wall flow regions. On the other hand, the V2F model is valid up to the solid walls. It is designed to handle wall effects in turbulent boundary layers and to accommodate non-local effects [23, 31].

Another widely used two-equation model is the standard $k-\omega$ of Wilcox [32, 33]. However, a well-known flaw of the standard $k-\omega$ model is its sensitivity to free-stream/inlet conditions. Menter [24] addressed this problem in the SST model. The SST model effectively blends a $k-\epsilon$ model in the far-field with a $k-\omega$ model near the wall. Thus, SST does not have the problem of sensitivity to free-stream/inlet conditions and is valid up to the wall. A modification is also made to the definition of the eddy-viscosity, which accounts for the effect of the transport of the principal turbulent shear stress [24].

Besides RANS approaches which model all scales, another approach to model turbulence is called the scale-resolving simulation which resolves the large scales of turbulence and models the small-scale motions. A common scale-resolving simulation is called the Large Eddy Simulation (LES). The problem with LES is that it is still too computationally costly for automotive flows. Detached Eddy Simulation (DES) is a hybrid modeling approach which combines the best of both RANS and LES: a RANS simulation in the boundary layers and a LES in the unsteady separated regions. Two variants of the DES were investigated in this study: DDES and IDDES. The DDES model incorporates a delay factor that enhances the ability of the model to distinguish between the LES and RANS regions on meshes where spatial refinement could give rise to ambiguous behavior. The IDDES approach allows RANS to be used in a much thinner near-wall region, in which the wall distance is much smaller than the boundary-layer thickness. In this study, the base RANS model used in these two DES

variants is SST $k - \omega$.

All models use the all y^+ wall treatment. The all-y^+ wall treatment is a hybrid treatment that emulates the low-y^+ wall treatment for fine meshes, and the high-y^+ wall treatment for coarse meshes. It is also formulated with the desirable characteristic of producing reasonable answers for meshes of intermediate resolution, that is, when the wall-cell centroid falls within the buffer region of the boundary layer ($1 < y^+ < 30$).

3.3.2 Vehicle Model

The vehicle model used in this study is a 2014 Hyundai Veloster with detailed underhood and underbody components as shown in Figure 3.1. The length, width, and height dimensions of this vehicle are 4220, 1800 and 1400 mm respectively. The front ground clearance is kept at 143 mm for all simulations. The geometry preparation process was performed using a commercial pre-processor code ANSA version 15.02. This involves the elimination of unnecessary vehicle components that do not interact with the external airflow, e.g. the vehicle interior parts. Modifications of some lesser important details were also made to further simplify the model, such as removal of bolts and nuts, closure of small holes and gaps, etc. All parts that have any impact on the external flow field were retained. The cleaned geometry was surface meshed in ANSA, and the mesh in NASTRAN format was imported into a commercial CFD code Star-CCM+ version 12.02 by CD-adapco for volume-meshing, simulation, and post-processing.

3.3.3 Cases Investigated

Two cases with different front-end configurations were investigated in this study. Case 1 is the baseline case with a vertical CRFM (an acronym for Condenser, Radiator, and Fan Module) and no air-duct. Case 2 differs from case 1 in two aspects: (1) it has an inclined CRFM and includes an air-duct as shown in Figure 3.2, and

Figure 3.1: Full vehicle model.

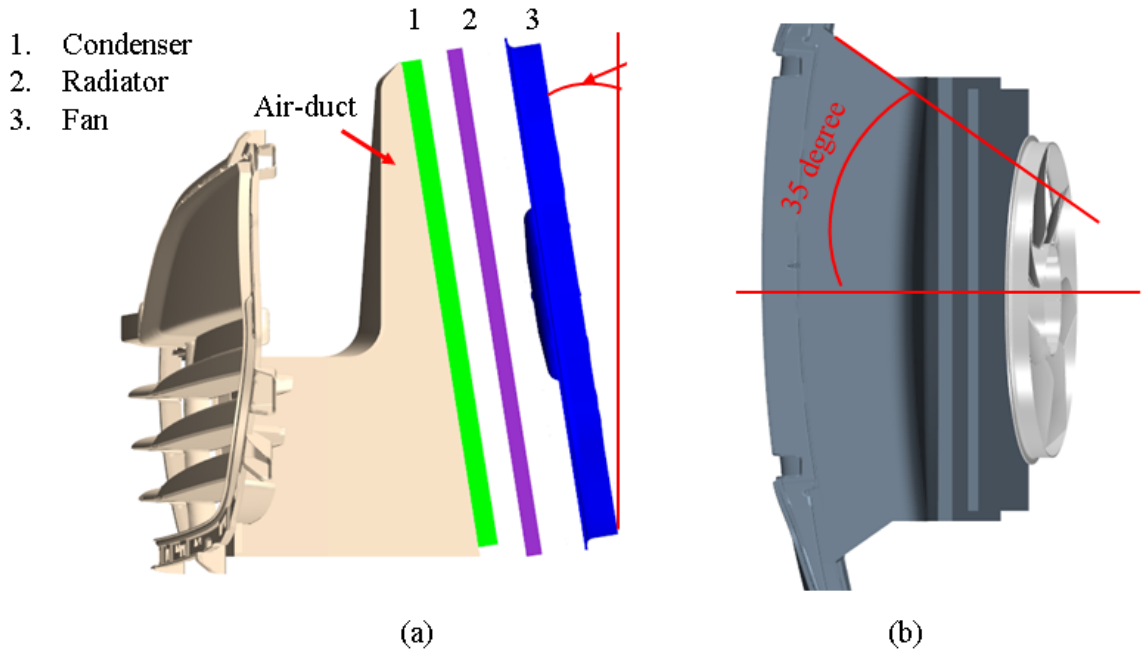

Figure 3.2: Inclined CRFM and air-duct in case 2; (a) side view, (b) top view.

(2) the side-grille-openings on either side of the primary grille–opening were sealed off in this case, see Figure 3.3. The combination of air-duct, inclined CRFM, and side-grille-opening sealing were investigated to achieve a simultaneous improvement of the radiator performance and cooling drag reduction. The benefits of such design changes have been well demonstrated by the authors in a previous study [80].

3.3.4 Boundary and operating conditions

The vehicle model was simulated in a sufficiently large virtual wind tunnel. The diagram of the virtual tunnel is shown in Figure 3.4, where L represents the overall length of the vehicle. Velocity inlet and pressure outlet boundary conditions were applied to the inlet and outlet respectively. A moving wall boundary condition was applied on the ground with a tangential speed same as the inlet air speed. The top and side walls were modeled as symmetry planes. The inlet air speed was set as a typical highway speed at 70 mph.

The condenser and radiator were modeled as a porous medium. The cooling fan

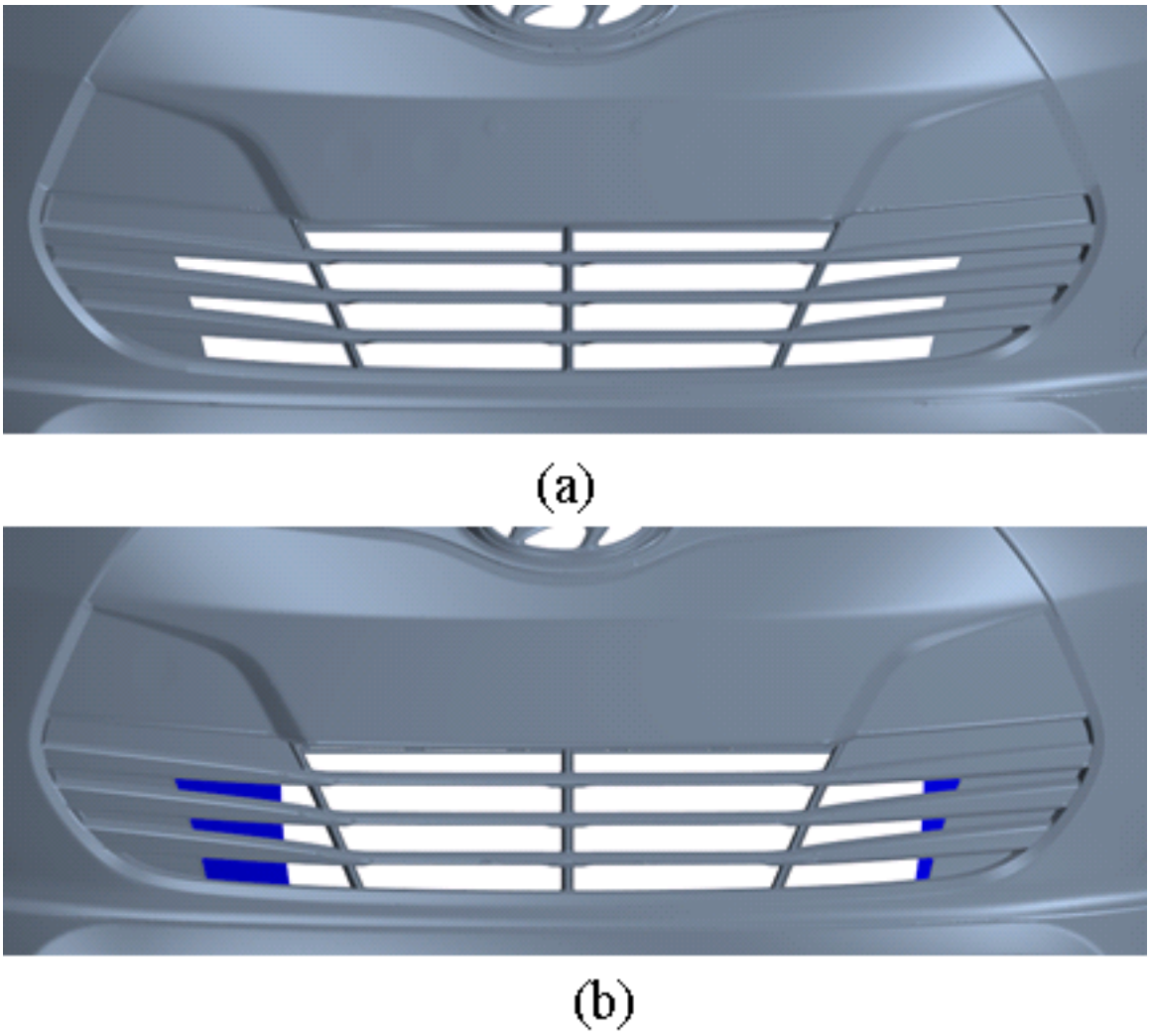

Figure 3.3: Front grille opening; (a) front grille with no side-grille-sealing as used in cases 1, (b) the front grille with both side-grilles sealed off as used in cases 2. The blue colored parts indicate how the side-grills were sealed off.

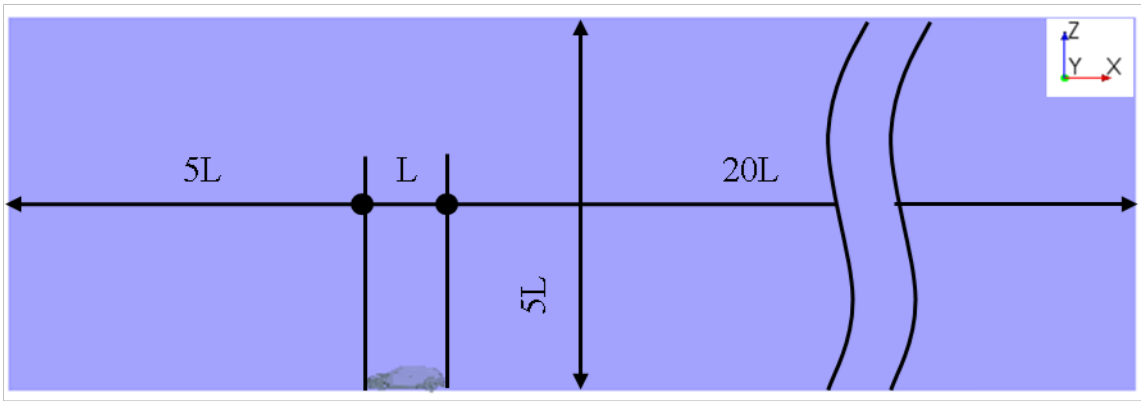

Figure 3.4: The computational domain.

rotation is simulated using the moving reference frame (MRF) method, which can provide reasonable pressure jump across the fan and swirl components downstream without experimental data as input. The wheel rotation is simulated by setting the tangential velocity same as the inlet air speed. In addition, the MRF method is applied to the regions between the spokes to simulate the pumping effect.

3.3.5 Mesh and Solver

The volume mesh primarily consists of hexahedral cells generated by the trimmed mesher. In addition, to properly capture flow features with high velocity gradient close to the solid boundary, 12 prism layers with the first node height of 0.005 mm and the total thickness of 6mm were applied on the external surfaces of the vehicle and the ground. To achieve a good balance between the accuracy and computational cost, mesh refinement was chosen to use volume sources that follow the external shape of the vehicle. This technique can generate a high quality volume mesh with a number of cells much fewer than that of traditional cubic block volume sources. Furthermore, volume mesh refinements were also applied on regions with complex flow patterns or separation, e.g. under-hood, under-body, wheels, and wake region. The cell size of the core mesh around the vehicle is 6 mm. Using the above mesh setting, a high-quality volume mesh with 75 million cells was generated, of which only 0.003% of the cells show volume change less than 1e-4 and 0.003% of the faces have face validity less than 0.95. All the simulations in this study used the same mesh setting. The mesh on the central plane of the vehicle is shown in Figure 3.5. Using the aforementioned prism layer setting, the y^+ values on the external surfaces of the vehicle in all the cases were mostly less than 0.5 as can be seen in Figure 3.6.

The finite volume method is used for the spatial and temporal discretization of the governing equations. The integral form of the conservation equations of mass and momentum are solved by the segregated flow solver in a sequential manner, i.e. the non-linear governing equations are solved iteratively one after the other for the solution

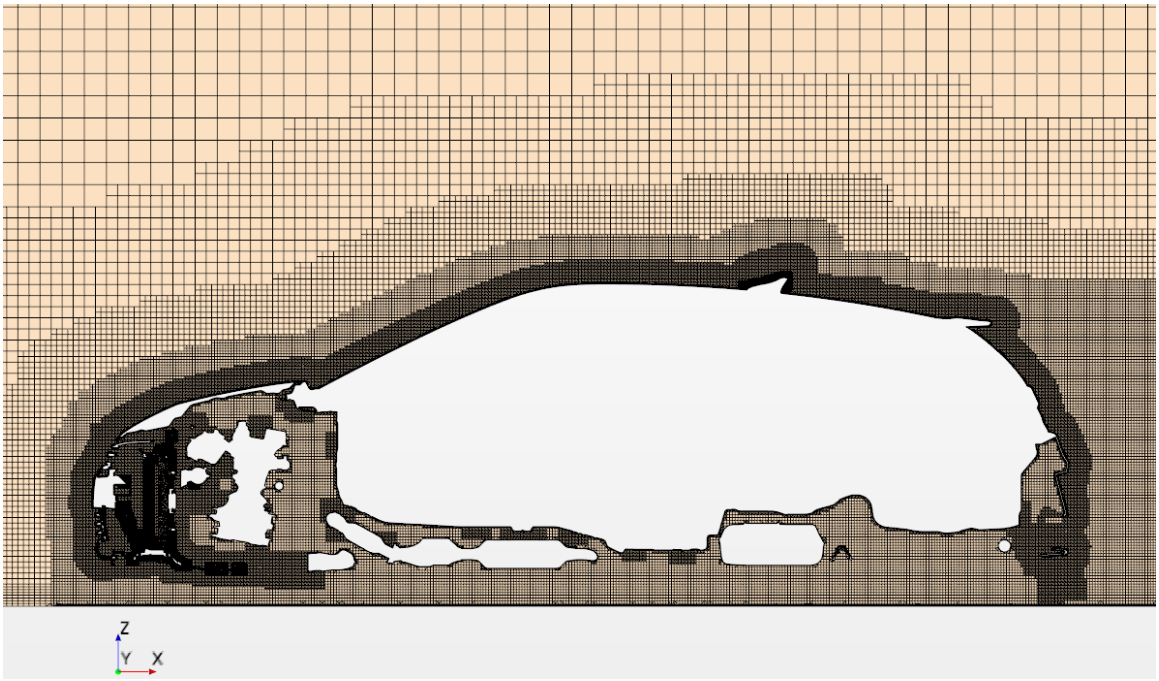

Figure 3.5: The mesh on the central plane of the vehicle.

variables such as the three velocity components and the pressure. The pressure-velocity coupling is achieved with a predictor-corrector approach called SIMPLE (Semi-Implicit Method for Pressure-Linked Equations). For RANS models, the discretization scheme for computing the convection flux on a cell face is Hybrid MUSCL (Monotonic Upwind Scheme for Conservation Laws) third-order/central-differencing; for DES variants, the discretization scheme is Hybrid/BCD (Hybrid second-order upwind/bounded-central). A second-order upwind scheme is used for computing the convection flux on a cell face for each turbulence model solver. An interested reader is directed to the Star-CCM+ user manual for further details.

3.4 Results and discussions

All the simulations were run on a cluster with 96 computing cores. All simulations were run until the flow reached an acceptable convergence judged by two criteria. Firstly, the normalized residuals of all transported quantities are steady, and, secondly, the drag force coefficient, averaged over last 500 iterations and 0.4 seconds

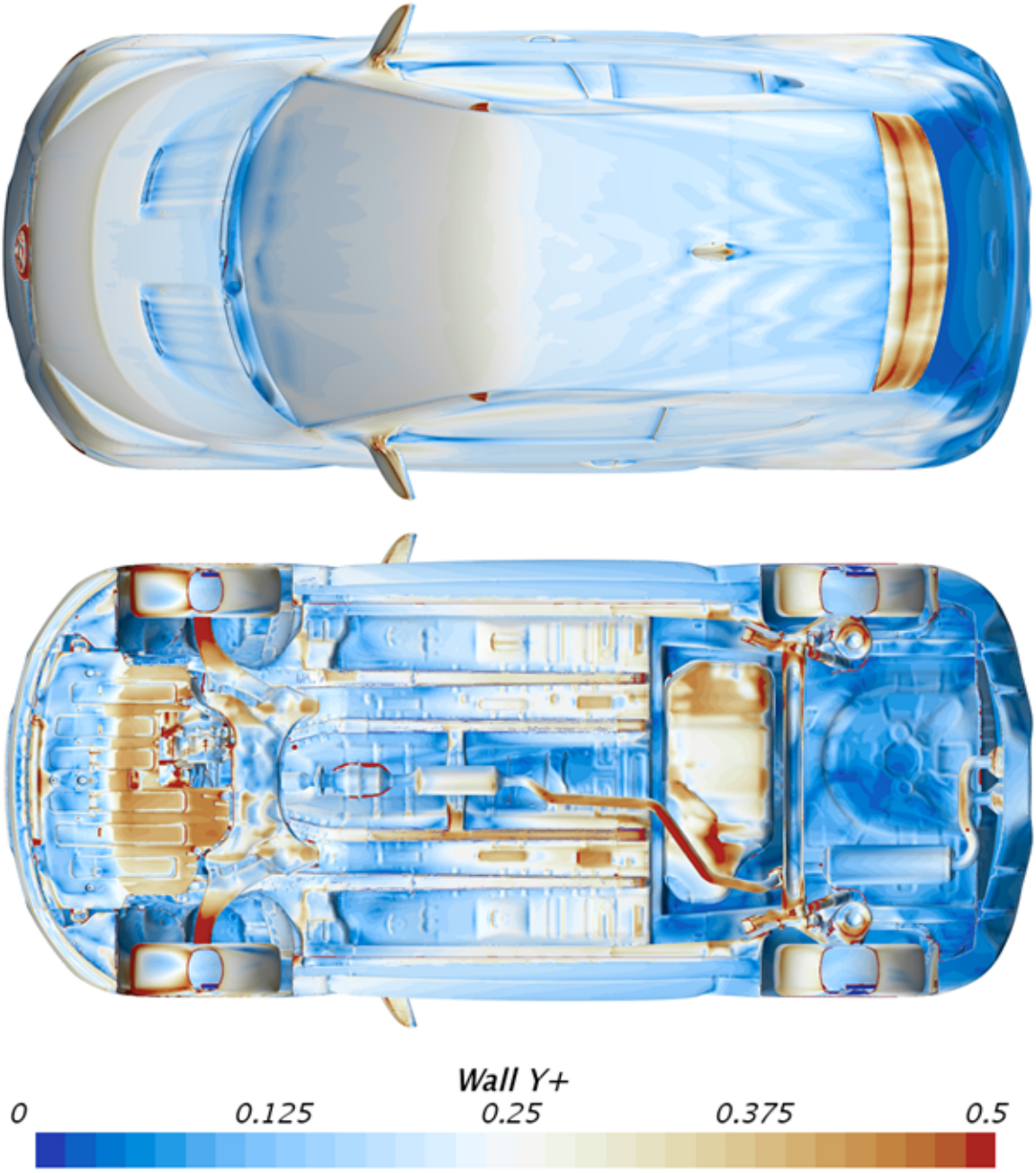

Figure 3.6: The wall y^+ values on the external surfaces of the vehicle.

(3 flow units) for RANS and DES respectively, does not show fluctuations over 3 counts. Based on these two stopping criteria, RANS and DES models took around 28 and 250 hours respectively to be completed. The DES simulations were run with a CFL number of 1 for 15 convective flow units ($T = 15 \times L/U = 2s$, where L is the car length and U is the freestream velocity). For the following sections, to have a comprehensive understanding of the differences between the six models used in this study on predicting the flow around a passenger vehicle, the discussions will cover force coefficients, velocity and pressure field, wake structures, and some other flow fields that are crucial to the flow features, such as the turbulent kinetic energy.

Mesh independence study was conducted for the baseline case with the RKE and the IDDES models to further eliminate the effect of the mesh on simulation results. For the RKE model, the fine mesh contains 100 million cells which are generated by reducing base size from 24 mm to 20 mm. A change of drag coefficient within 1% between 75 and 100 million cells was achieved in this process. However, for the IDDES model, simply reducing base size will increase computational cost dramatically not only due to increased cell number, but also due to the smaller time step resulted from reducing core mesh size close to the vehicle. Thus, a different strategy, where only the cells in the wake region and underbody area were halved, was used to refine the mesh for the IDDES model. As suggested by [81], the recommended mesh size in the detached flow regions for a DES type simulation should be close to the Taylor microscale given by $\lambda = 15^{1/2} A^{-1/2} R_l^{-1/2} l$, where A is an undetermined constant set to be 0.5, l is the bulk integral scale (taken as the vehicle length, L) and R_l the integral scale Reynolds number (here taken as the Reynolds number based off the free-stream velocity and vehicle overall length L, R_e). For the Reynolds number used in this study, the Taylor microscale λ is estimated to be 7.9 mm. Therefore, the mesh strategy used to refine the IDDES case with a mesh size of 6 mm in the wake region and underbody is reasonably fine enough. The fine mesh of the IDDES model

(shorted as IDDES Fine in this study) contains 87 million cells by using this strategy. Further to eliminate the numerical uncertainty, the IDDES fine case was run with a CFL number of 0.5. It was found that the change of drag coefficient is within 1%, thus the coarser mesh with a CFL number of 1 is sufficient enough for performing the intended investigations.

3.4.1 Drag and Lift Forces

Due to the proprietary nature of the data, the drag coefficient values are normalized, using an arbitrary reference area, such that the baseline car C_D obtained from the RKE model matches with the one available in public domain. Data downloaded from the website Edmunds.com,"features & specs 2014 Hyundai Veloster", https://www.edmunds.com/hyundai/veloster/2014/features-specs/, accessed June 19, 2017, indicates that the drag coefficient of 2014 Hyundai Veloster is 0.320. Thus the C_D for the baseline case obtained from the RKE model is set to 0.320, and the predictions from all other approaches are nominalized accordingly.

Table 3.1 shows the percent deviation of the predicted C_D values from the wind-tunnel test data for all investigated models; the data presented in this table corresponds to the baseline vehicle model. Firstly, it can be seen that C_D prediction from the RKE agrees very well with the experimental data. However, all other models predicted significantly higher drag coefficient with the highest C_D value from the AKN model. Unfortunately, while both the DDES and IDDES models, which apply SST model in the boundary layers, predicted slightly better drag coefficient compared with that of the SST model, they failed to predict well correlated C_D values. Furthermore, for the DES models, while the C_D prediction of the IDDES was slightly better than that of the DDES, the IDDES model with fine mesh produced negligible improvement. The fact that even the IDDES Fine case failed to predict well correlated C_D values indicates the monumental challenge that is still encountered by the CFD simulation of automotive flows. Although the RKE model predicted significantly better

Table 3.1: Percent deviation of C_D predictions from the experimental data for the baseline vehicle model.

$\%C_D$ deviation	RKE	AKN	V2F	SST	DDES	IDDES	IDDES Fine
Case 1	1.3%	13.8%	10.0%	12.9%	11.5%	10.9%	10.8%

C_D value than all other investigated models, it should be cautioned that this does not suggest the superior performance of the RKE model. For the RANS and DES models, the drag prediction may contain error cancellation of flow fields in different regions around the vehicle.

Table 3.2 summarizes drag and lift coefficients corresponding to both vehicle configurations as obtained from the studied turbulence models. These include the coefficients of drag, total lift, front and rear lift, and the front to total lift ratio, known as the lift balance or percent front. Data presented in Table 3.2 are graphically summarized in Figure 3.7 - 3.9 to illustrate the predictive differences between all models in terms of drag, lift and percent front. It can be seen that, the RKE model predicted significantly smaller C_D values for both cases compared to the other models. For instance, the RKE predicted 11.1% less C_D value than the AKN for case 1 and 17.1% smaller C_D value than the DDES model for case 2. Moreover, while all models predicted higher C_D value for the baseline case than that for the air-duct case, the two DES variants predicted much smaller differences between these two cases when compared with predictions from all RANS models as can be seen in Table 3.3. For instance, while IDDES predicted a delta C_D of 4 counts between the two car configurations, the RKE model predicted a 30 counts difference. With respect to the total lift, front lift, rear lift, and the front lift ratio, the predictive differences for both cases are much larger than drag for all the models investigated, especially for the front lift ratio. Further, comparing the two IDDES simulations with different mesh strategy for baseline case, while there is no difference in C_D prediction, a noticeable discrepancy can be seen in C_L prediction. In short, for all the turbulence models and

Table 3.2: Drag and lift coefficients for all models.

Case #	Turbulence models	C_D	C_L	C_L/C_D	C_{LF}	C_{LR}	%Front
Case 1	RKE	0.320	0.098	0.305	-0.013	0.111	-13.2%
	AKN	0.360	0.096	0.267	-0.035	0.132	-36.5%
	V2F	0.348	0.129	0.371	-0.015	0.144	-11.4%
	SST	0.357	0.096	0.269	-0.033	0.130	-34.6%
	DDES	0.352	0.084	0.238	-0.041	0.126	-49.5%
	IDDES	0.350	0.060	0.171	-0.045	0.106	-75.4%
	IDDES Fine	0.350	0.072	0.206	-0.058	0.135	-80.8%
Case 2	RKE	0.290	0.073	0.251	-0.021	0.122	-29.1%
	AKN	0.331	0.050	0.150	-0.046	0.126	-92.6%
	V2F	0.322	0.065	0.201	-0.042	0.136	-65.7%
	SST	0.337	0.086	0.255	-0.037	0.152	-43.0%
	DDES	0.350	0.080	0.226	-0.077	0.157	-97.7%
	IDDES	0.347	0.088	0.253	-0.072	0.160	-82.1%

Table 3.3: Delta drag and lift coefficients between case 1 and case 2 for all models.

Turbulence models	C_D	C_L	C_L/C_D	C_{LF}	C_{LR}	%Front
RKE	0.030	0.025	0.055	0.008	-0.011	15.9%
AKN	0.029	0.046	0.116	0.011	0.006	56.1%
V2F	0.026	0.065	0.171	0.028	0.007	54.3%
SST	0.020	0.010	0.014	0.004	-0.022	8.4%
DDES	0.002	0.005	0.012	0.036	-0.030	48.2%
IDDES	0.004	-0.028	-0.082	0.027	-0.053	6.7%

mesh strategies studied, the prediction of drag is more consistent than that of lift. Moreover, even for industrial automotive flows which feature complex geometry and exhibit massive separations, certain model could predict the C_D value that correlates with the experimental data very well.

The accumulated drag coefficient along the vehicle for the baseline case from all turbulence models is shown in Figure 3.10. It can be seen, firstly, that before the airflow passing through the CRFM ($X/L = 0 - 0.06$), all the models predict almost identical results; then, in the underhood region from the CRFM to the cowl area ($X/L = 0.06 - 0.25$), the RKE predicted a significantly lower drag value than that from all other models. Nevertheless, the results from the RKE in this region still follow

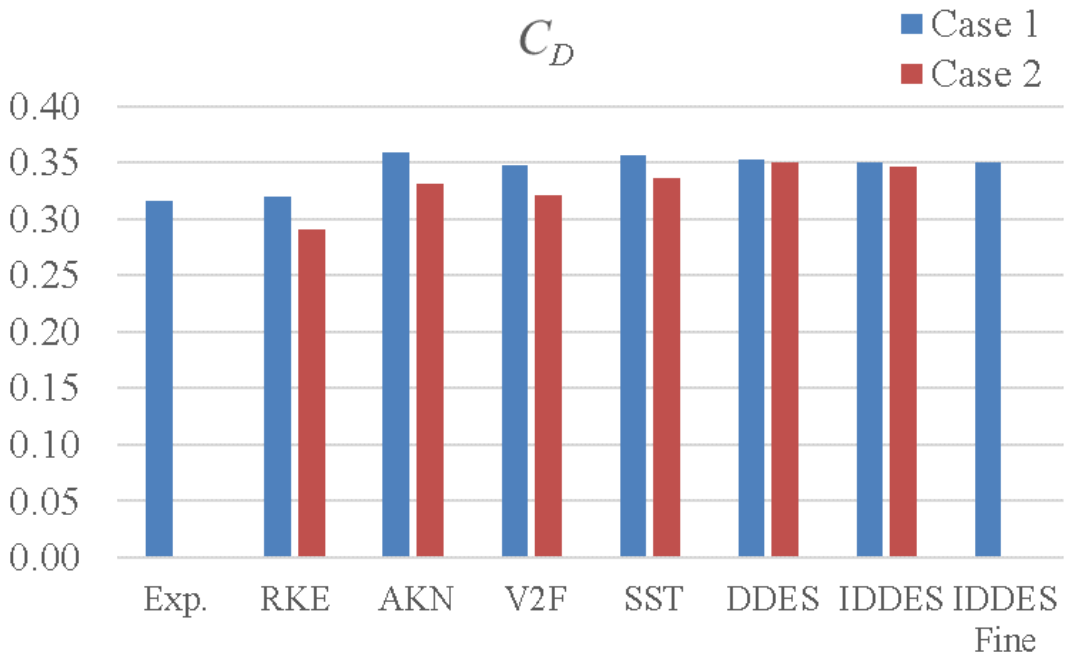

Figure 3.7: C_D for both cases from the predictions of all turbulence models and the experiment.

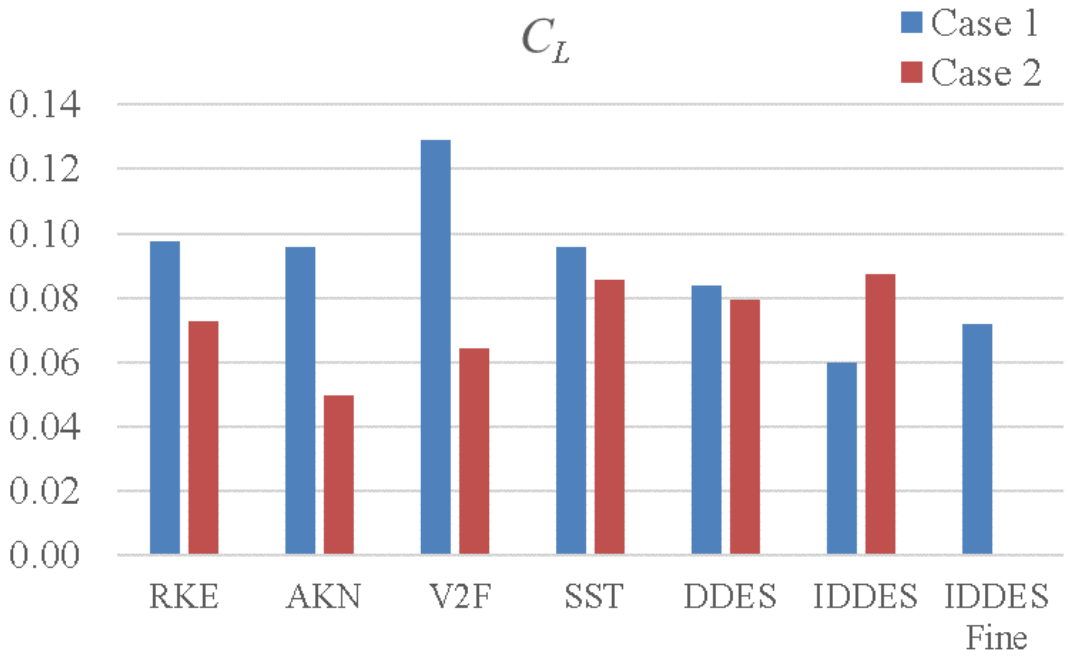

Figure 3.8: C_L for both cases from the predictions of all turbulence models.

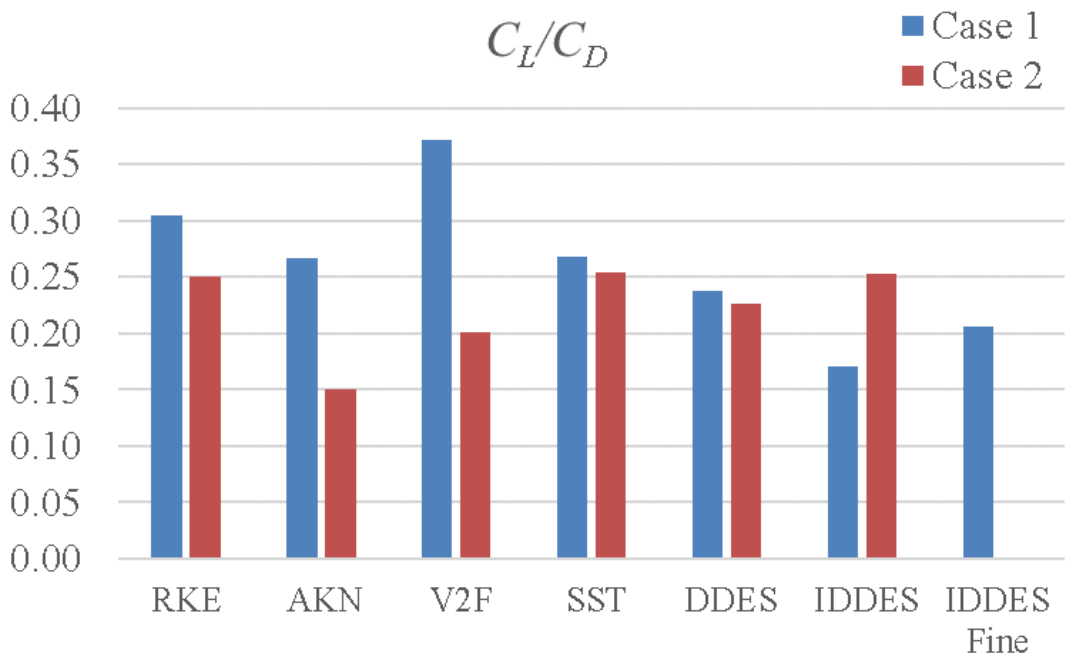

Figure 3.9: C_L/C_D for both cases from the predictions of all turbulence models.

the same trend as all other models. Further, all the models predict almost identical trends, though with different magnitude, in the region between the cowl area and the rear spoiler where the flow is mostly attached ($X/L = 0.25 - 0.85$). However, at the rear end of the vehicle, the predictions from all the models start to diverge from each other significantly, especially that of the DDES and the RKE. In short, for the vehicle model used in this study, all the turbulence models investigated could predict consistent results even in the underhood compartment where the flow is featured with separations and complex interactions between cooling airflow and underbody airflow. However, no consistent results between all the models were observed for the prediction of the wake region where massive separation occurs.

The delta accumulated drag coefficient between case 1 and 2 vehicle configurations for all turbulence models is shown in Figure 3.11. Firstly, it is not surprising to observe significant prediction fluctuations in the front part of the vehicle since the only difference between the two vehicle models is the front end configuration. For this part

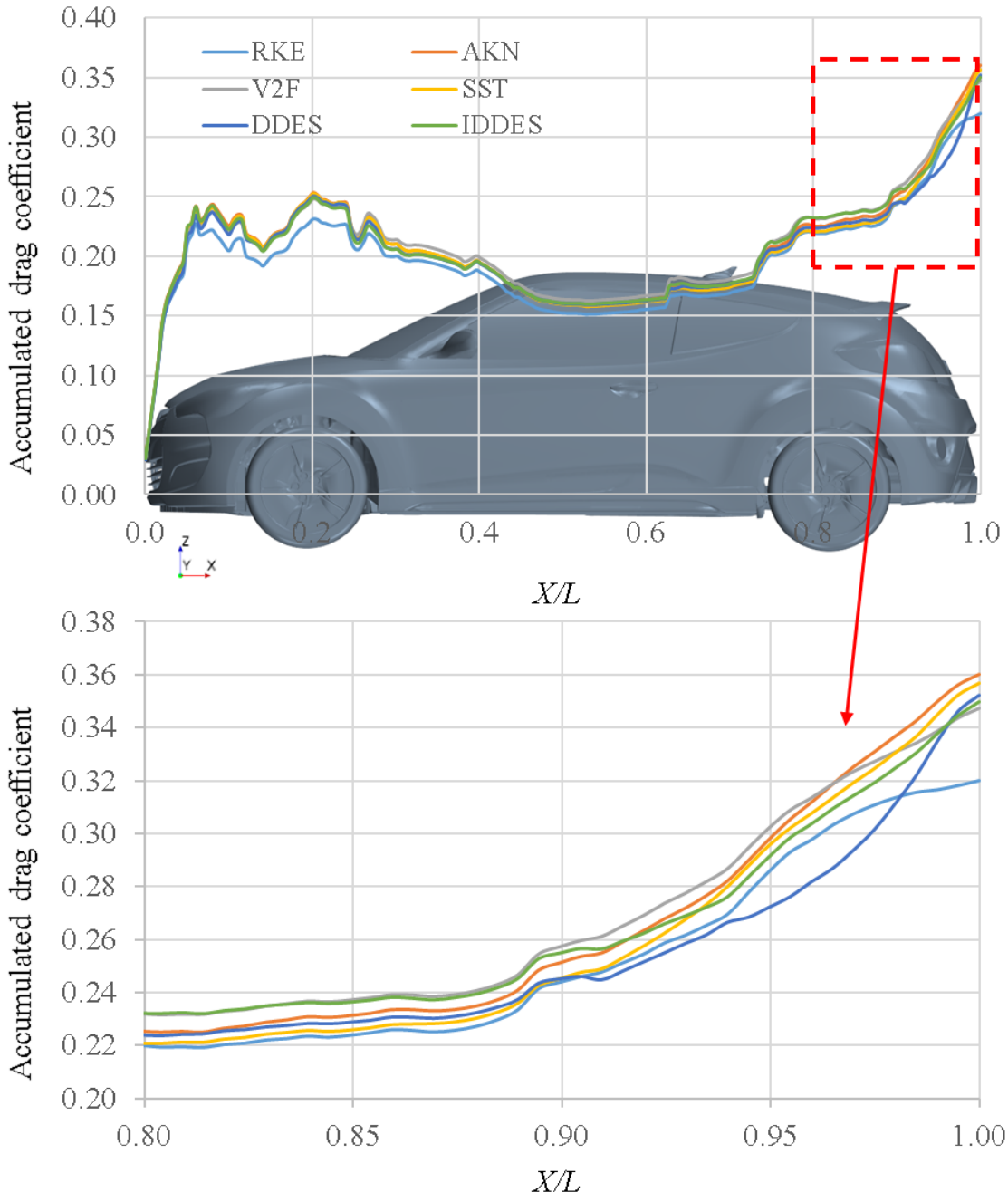

Figure 3.10: Accumulated drag coefficient along the streamwise direction for the baseline case obtained from all turbulence models (L represents the vehicle total length).

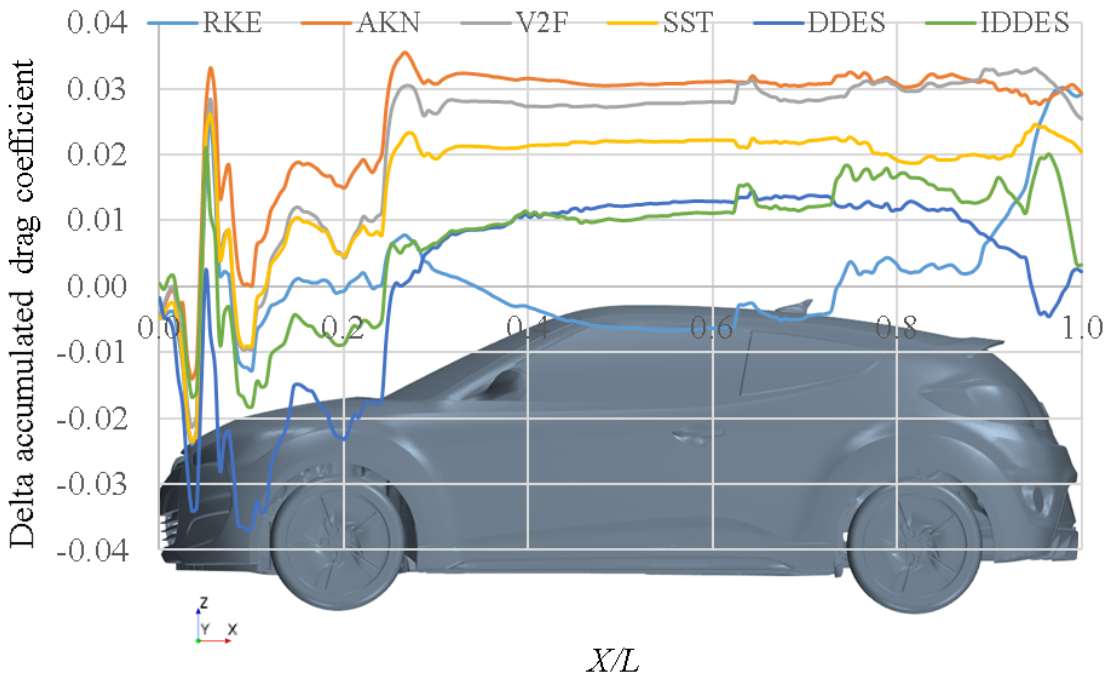

Figure 3.11: Delta accumulated drag coefficient between case 1 and 2 vehicle configurations along the streamwise direction obtained from all turbulence models (L represents the vehicle total length).

of the vehicle, although all turbulence models predicted similar trends, the noticeable differences in magnitude indicate that the high sensitivity of C_D prediction on the choice of turbulence models. Further, the noticeable fluctuations in the rear end, especially for the RKE, DDES and IDDES models, highlight the dramatic influence of predictions of upstream flow on the downstream flow. Moreover, the prediction trend of the RKE model differs significantly from all other models in two areas: the windshield and the rear end. The causes of prediction differences will be qualitatively and quantitatively analyzed in the following sections.

3.4.2 Pressure and Velocity Fields

3.4.2.1 Baseline Case

As stated in the previous section, the front and rear end of the vehicle contributes most to the C_D difference for all the turbulence models studied. To better analyze

the C_D prediction differences for all the models, the pressure and velocity field at the front end and rear end of the vehicle were investigated.

For the baseline case, since the RKE predicts a significantly lower C_D value, the pressure coefficient from RKE model on the back of the vehicle was shown first in Figure 3.12. It can be seen that the most noticeable higher pressure area is right above the exhaust pipe. This area is the saddle of attachment of the wake flow as supported by the streamline structure in Figure 3.14 (RKE). To better illustrate the differences between the RKE and the other models for baseline case, the delta pressure coefficient on the back of the vehicle between the RKE model and all other models is shown in Figure 3.13. Firstly, all other models predict overall lower pressure when compared with that of the RKE, especially the three RANS models. This is consistent with the results of accumulated drag as shown in Figure 3.10. More specifically, comparing to the RKE model, the different pressure distribution predicted by the AKN model might be explained by the key differences between the RKE and the AKN model on their approaches in solving the viscosity dominated near-wall flow regions, i.e., while the RKE model uses the Two-Layer Approach (the implement in Star-CCM+ is the formulation proposed by [30]) which is calibrated based on Couette flow, the AKN model adopted Low-Reynolds Approach with the introduction of the Kolmogorov velocity scale, instead of the friction velocity, to account for the near-wall and low-Reynolds-number effects in both attached and detached flow. On the other hand, both the V2F and SST models can resolve down to the viscosity dominated near-wall regions. Thus, more evident prediction differences in certain areas, such as the area around the right taillight and both sides of the vehicle, against the RKE model are expected. Further, the delta pressure distribution predicted by the two DES variants shows a completely different pattern with that of the other three RANS models. Interestingly, they both predict less discrepancies against that of the RKE model, with slightly higher pressure on the upper part but lower pressure on the lower part.

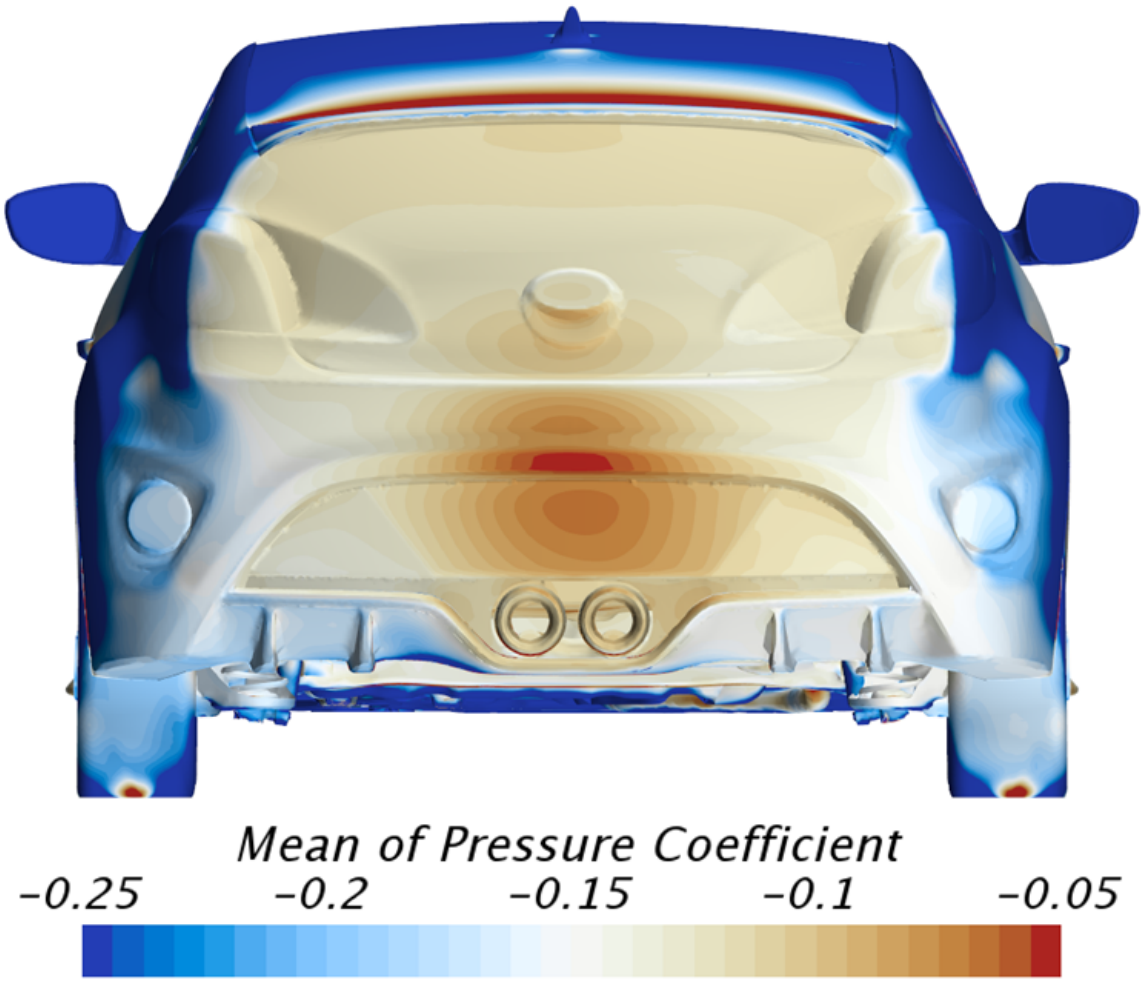

Figure 3.12: The pressure coefficient from the RKE model on the back of the vehicle for the baseline case.

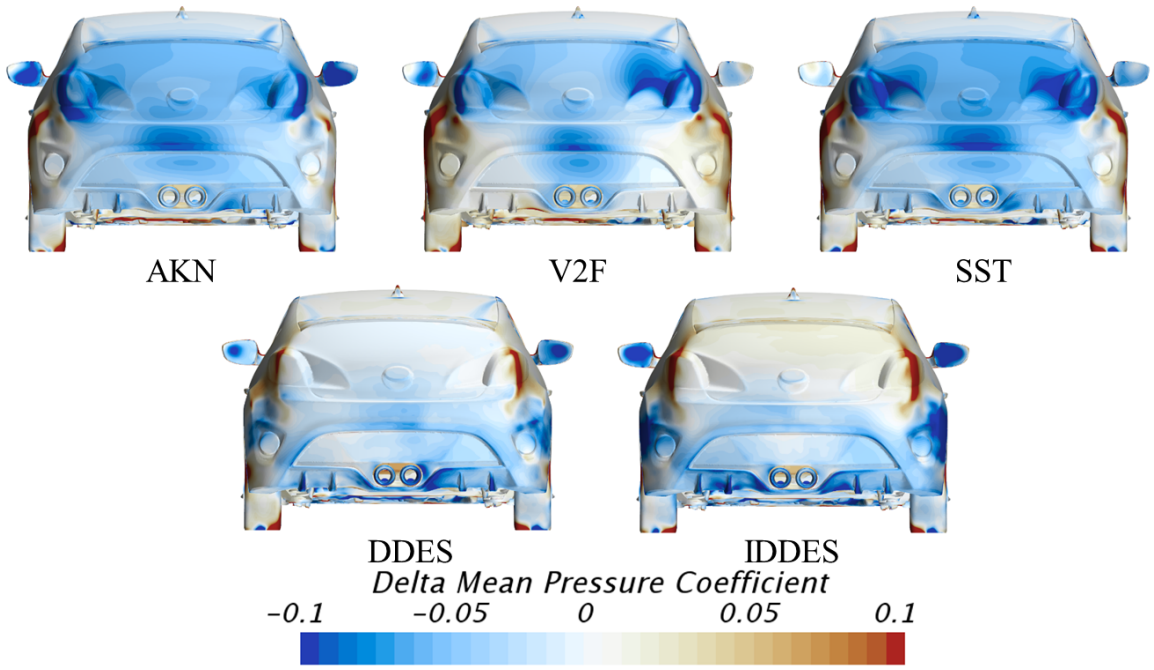

Figure 3.13: The delta pressure coefficient against the RKE model for all other models for the baseline case on the back of the vehicle.

The vector scenes with constrained streamlines present insight information of wake structure as demonstrated in Figure 3.14. Firstly, the RKE model predicts two strong counter-rotating vortices with the saddle of attachment area right above the exhaust pipes (see Figure 3.12). Secondly, comparing with the RKE model, the other three RANS models predict significantly different wake structures: (1) no counter-rotating vortices exist; (2) the lower vortex is much weaker and the saddle of attachment area is at a lower location; (3) wake area is much smaller (see the areas on the right of the red spline line in corresponding images). On the other hand, again interestingly, two DES variants predict mostly similar wake structure as that of the RKE model, e.g. counter-rotating vortices, saddle of attachment location and similar wake area. However, some differences can still be observed: (1) the top vortex core is at a further downstream location; (2) wake structures are more complex, especially that the DDES predicts a tertiary vortex near the exhaust pipes and the IDDES predicts a tertiary vortex under the spoiler.

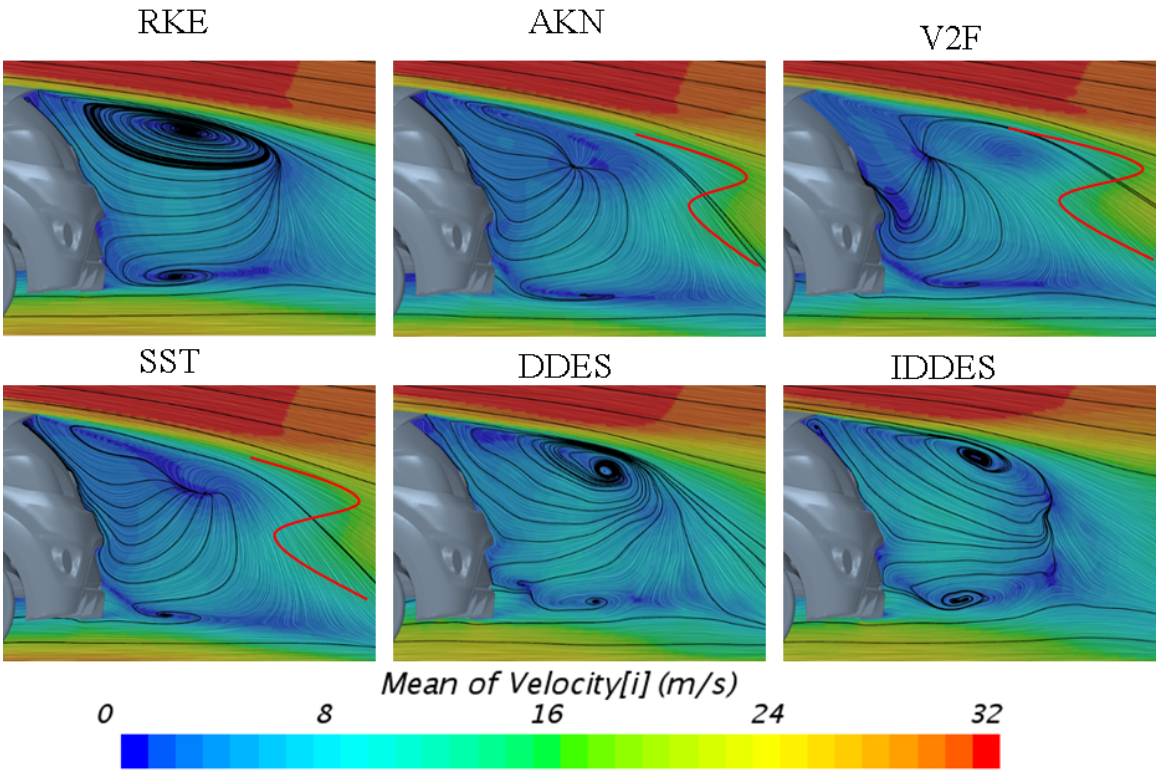

Figure 3.14: Vector scene with constrained streamlines in the wake region (on the central plane of the vehicle) for the baseline case from all models studied.

To further investigate the prediction differences between all the models studied, the streamwise velocity profile inside the boundary layer for baseline case was plotted at four selected lines: (1) on the hood; (2) behind the antenna; (3) on the rear end of the spoiler; (4) on rear glass. It can be seen, for line 1 and line 3 where flow is attached, similar trends can be observed for all the models studied except the AKN model, such as (1) all the models predict same velocity profile at the region very close to the wall (viscosity dominated region), which is mainly due to the fact that wall functions for all the models work well in the attached flow region. (2) above the viscosity dominated region, while the models studied start to show differences in velocity growth, all models predict similar trends except the prediction from the AKN model for line 1. The unexpected streamwise velocity profile of the AKN for line 1 looks quite suspicious, which indicates that the Low-Reynolds number approach implemented in the AKN model may not work well even in the attached flow region. On the other hand, for line 2 and line 4 which are inside wake region, all models studied differ from each other significantly. In short, for the models studied, while consistent streamwise velocity profile can be observed in attached flow regions except for the AKN model, the significant different predictions of streamwise velocity in wake regions further shows the strong dependence of turbulence models on predicting complex automotive flows.

To have a more comprehensive analysis of the flow field, three plane sections (see Figure 3.17) were selected for flow visualization: (1) through the underhood area; (2) at the rear of the vehicle; (3) inside the wake region. The streamwise velocity scenes on these three selected plane sections from all models for the baseline case are shown in Figure 3.18. It can be seen that, on plane $X/L = 0.15$, all models predict similar streamwise velocity distribution. However, comparing with the other three RANS models, the RKE model predicts a larger negative streamwise velocity area in the upper part of the wake region on planes $X/L = 1.0 and 1.1$ (see the black lines).

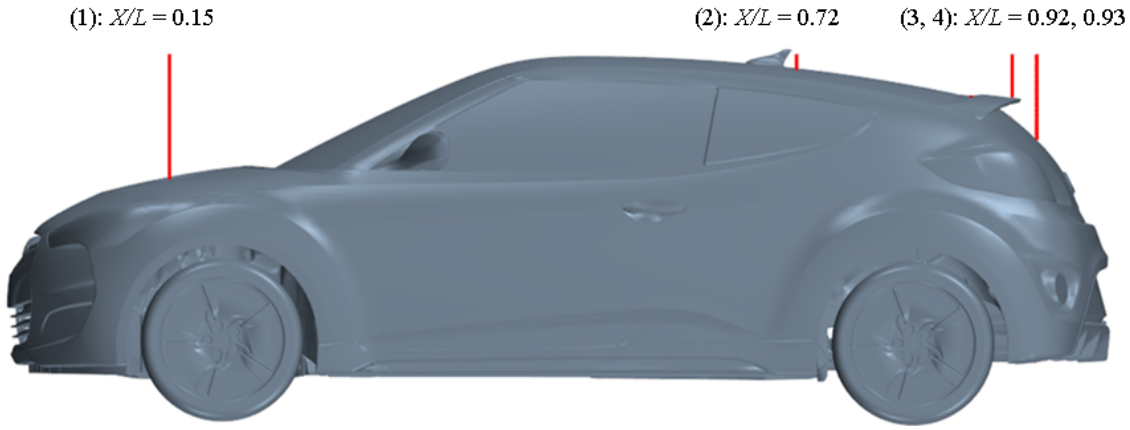

Figure 3.15: Four selected lines (on central plane of the vehicle) for quantitative analysis inside boundary layer. Note the four red lines only represent the location, not the actual length.

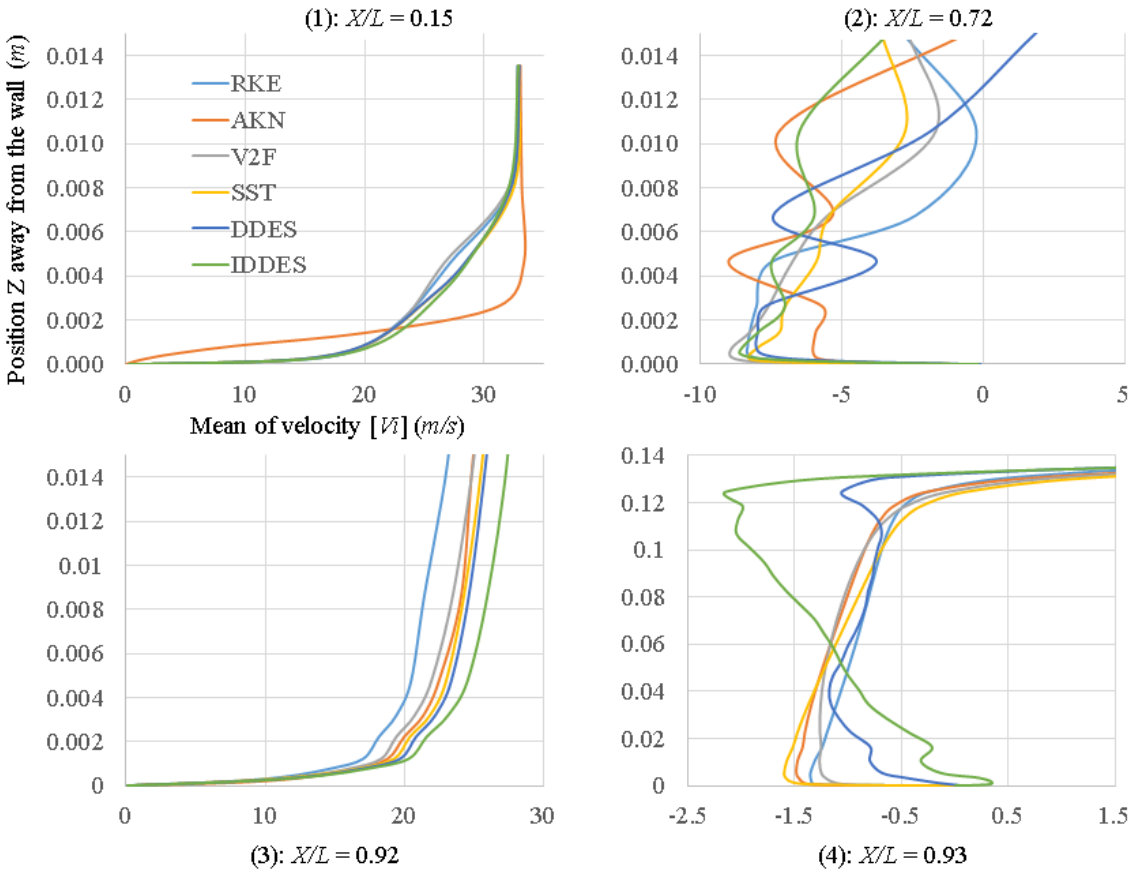

Figure 3.16: Streamwise velocity profile inside boundary layer at four selected lines (on central plane of the vehicle) from all models studied for baseline case.

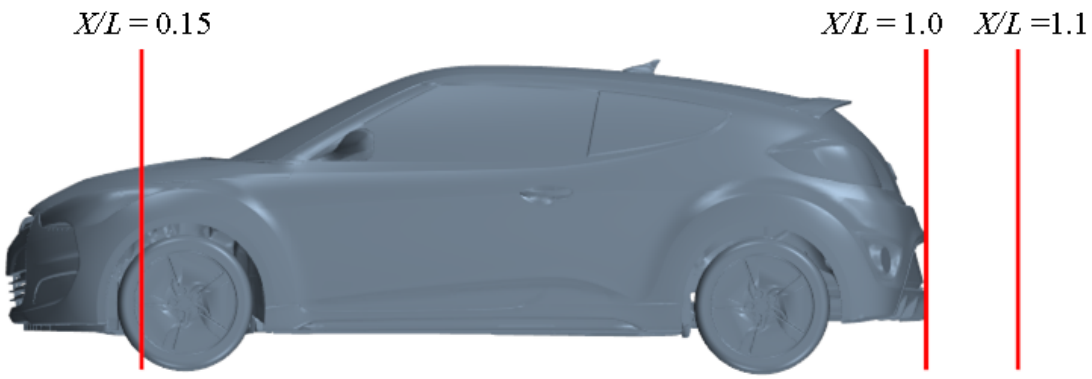

Figure 3.17: Locations of selected plane sections.

Moreover, the RKE model predicts a smaller negative streamwise velocity area in the lower part of the wake region on plane $X/L = 1.1$ (see the yellow dashed lines). Surprisingly, the predictions from the two DES variants are quite similar to that of the RKE model on both selected planes. While the mesh size in the wake region is not fine enough for the DES type simulations, these two DES variants are still expected to predict better large scale flow features due to that they are capable of resolving large scale flow features directly. The similarity of streamwise velocity profile on these two planes between the predictions from the DES variants and the RKE model supports that the RKE model performs better than the other three RANS models for the baseline case. This can be further confirmed by the delta streamwise velocity against the IDDES Fine model on these planes as shown in Figure 3.19. It can be seen that the RKE predicts closer velocity profiles in the wake region to that of the IDDES Fine model than the other three RANS models. Moreover, the IDDES case with the coarse mesh predicts very similar results as that from the fine mesh, which indicates that the coarse mesh is sufficient enough for this study.

3.4.2.2 Comparison Between the Baseline Case and the Air-duct Case

Besides the analysis of the prediction differences between studied models for baseline case, further, this study also presents the comparison of flow field predicted by each model between both cases with different front-end configurations. This is done

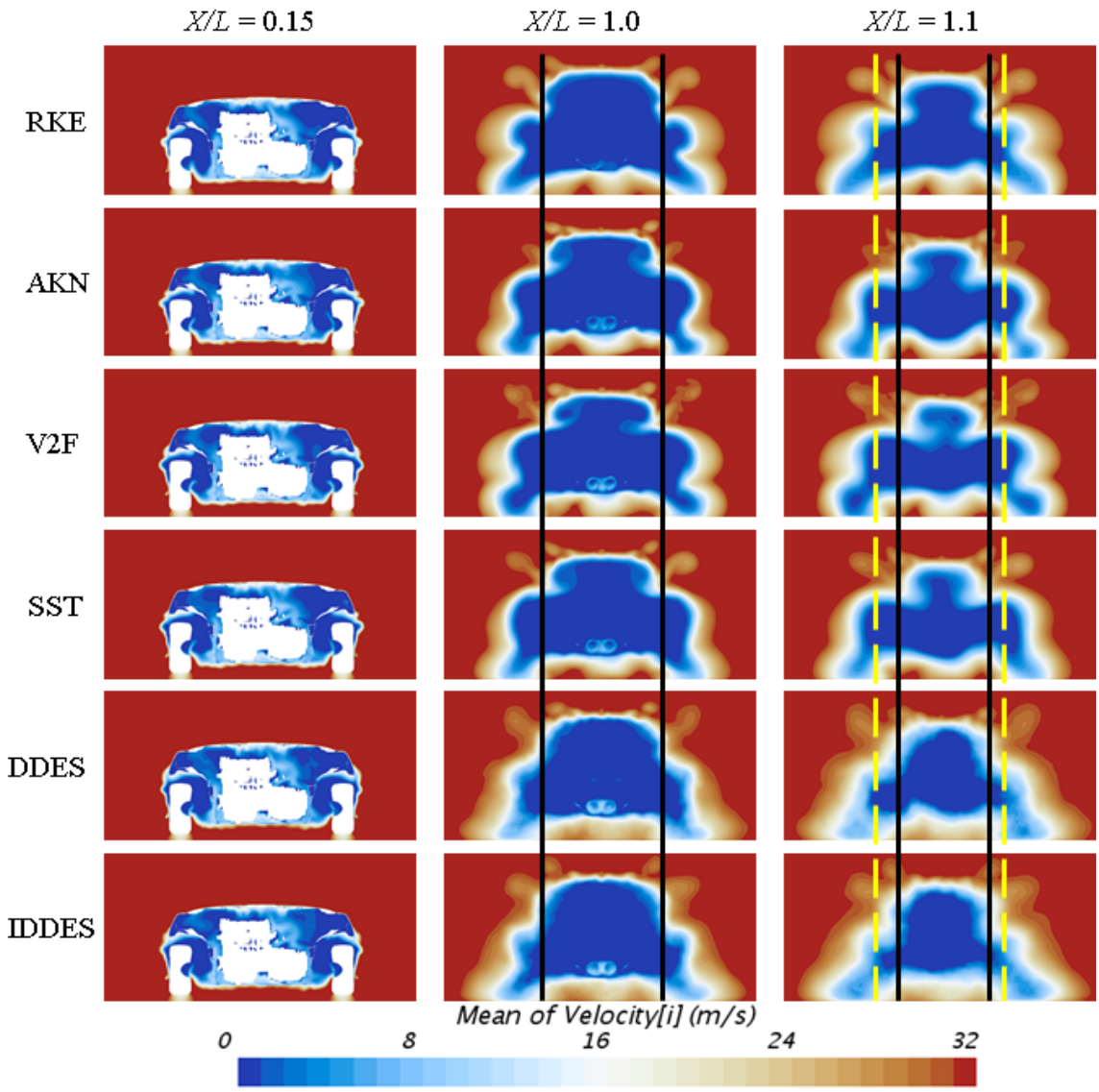

Figure 3.18: Streamwise velocity on selected plane sections from all models for the baseline case.

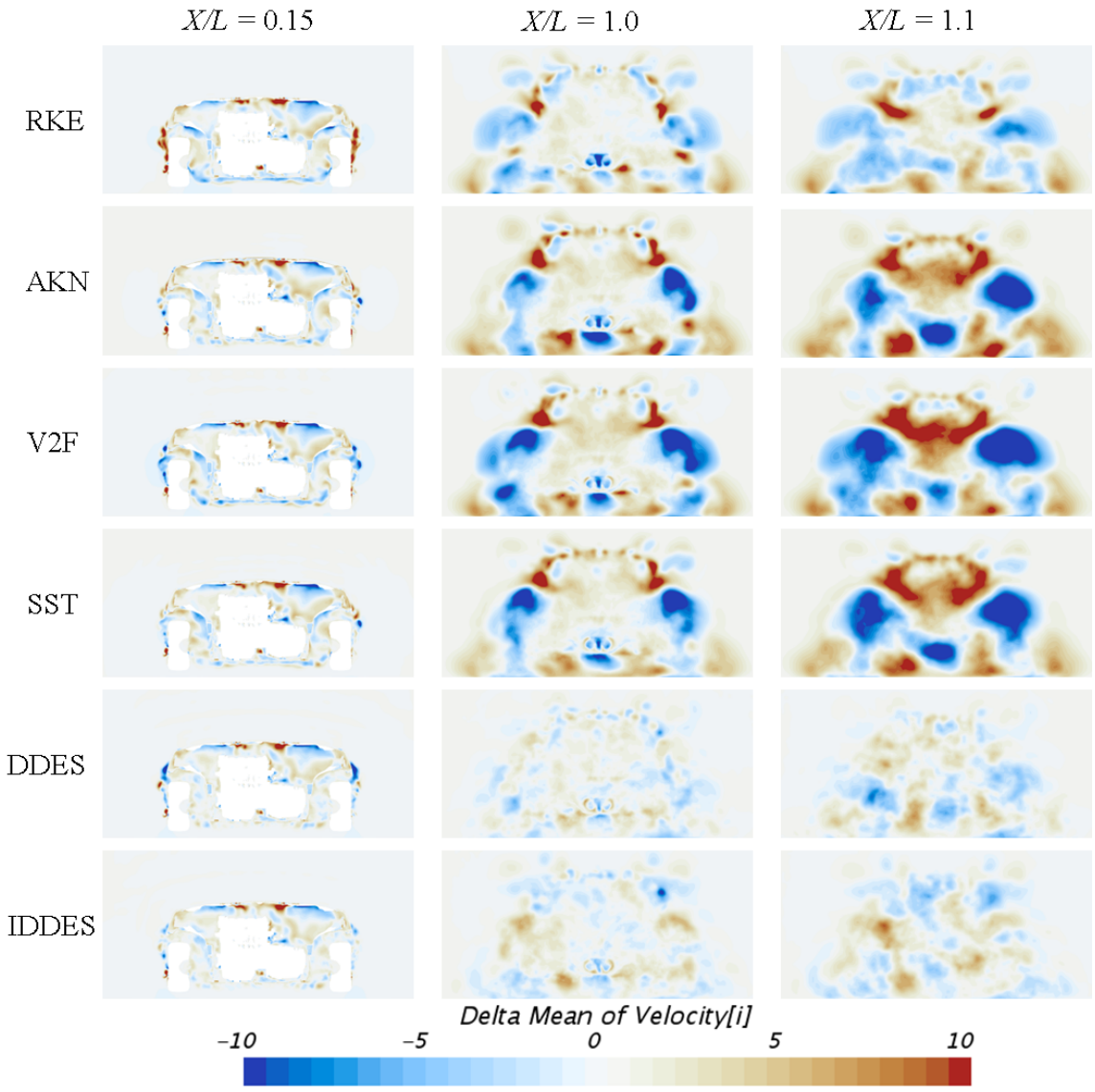

Figure 3.19: Delta streamwise velocity on selected plane sections against the IDDES Fine for all other models for the baseline case.

by presenting delta values, i.e., for a certain parameter, the values from the air-duct case subtracted from that of the baseline case.

The delta pressure coefficient on the external surfaces of the vehicle between the two cases is shown in Figure 3.20. Firstly, as expected, all the models predict higher pressure coefficient in the front-end part of the vehicle for the baseline case, since the larger front grille opening in the baseline configuration will result in more airflow entering the underhood compartment. However, noticeable differences can be observed for the pressure distribution prediction on the rest of the car. Particularly, the prediction from the RKE model differs significantly from that of all other models, i.e. the RKE model predicts noticeable lower pressure on the rest of the car. This is consistent with the delta accumulated drag plot as shown in Figure 3.11. Further, the two DES variants predict lower pressure on the rear bottom part of the vehicle. These observations indicate that the change of upstream geometry may result in noticeably different downstream predictions of flow field depending on the choice of turbulence models.

The delta mean streamwise velocity on the selected planes (see Figure 3.17) between the two cases is shown in Figure 3.21. Firstly, on plane $X/L = 0.15$, it can be seen that the influence of front wheels rotation predicted by the RKE model differs from that of the other three RANS models. Surprisingly, despite that the RKE model predict larger deviation of pressure distribution on most part of the vehicle as shown in Figure 3.20, the streamwise velocity deviation on the two planes in the wake regions predicted by the RKE model is much smaller than that of the other three RANS models. On the other hand, the two DES variants predict slight larger deviation than that of the RKE model but much smaller than that of the other three RANS models.

3.4.3 Turbulence Kinetic Energy

In addition to velocity and pressure field, turbulent kinetic energy is another flow parameter that has an important role in the turbulence mechanism and the formu-

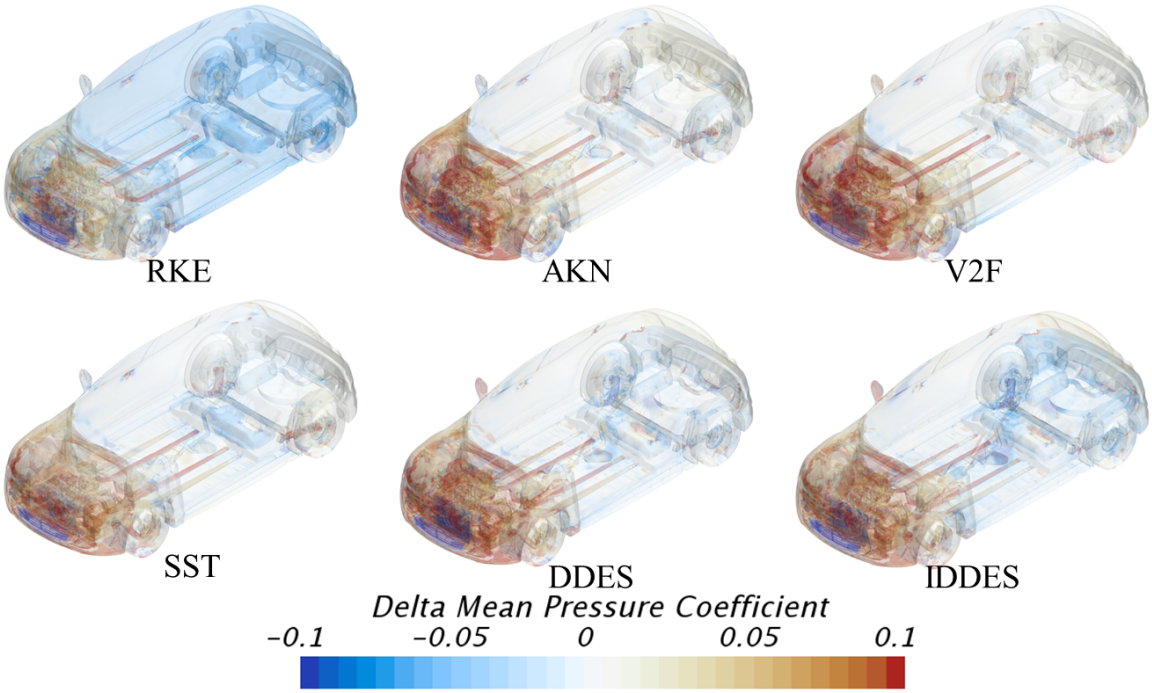

Figure 3.20: The delta pressure coefficient on the external surfaces of the vehicle between the baseline case and the air-duct case for all the studied models.

lation of most turbulence modeling process. The distribution of turbulent kinetic energy on selected plane sections (see Figure 3.17) from all models for baseline case is shown in Figure 3.22. Firstly, it can be seen that the RKE model predicts generally higher turbulent kinetic energy than the other three RANS models on all the selected planes. Further, the two DES variants predict much higher turbulent kinetic energy on all selected planes than that of all the RANS models, which is consistent with the work of [61]. Again, comparing to the other three RANS models, the turbulent kinetic energy distribution predicted by the RKE model is closer to that of the DES variants.

This study also presents the delta turbulent kinetic energy on the selected planes (see Figure 3.17) between the two cases as shown in Figure 3.23. It can be seen again that the RKE model predicts smaller deviation when compared with the other three RANS models. Further, the two DES variants predict larger and more "spotted" deviation than all the RANS models. This may due to that: (1) the DES variants

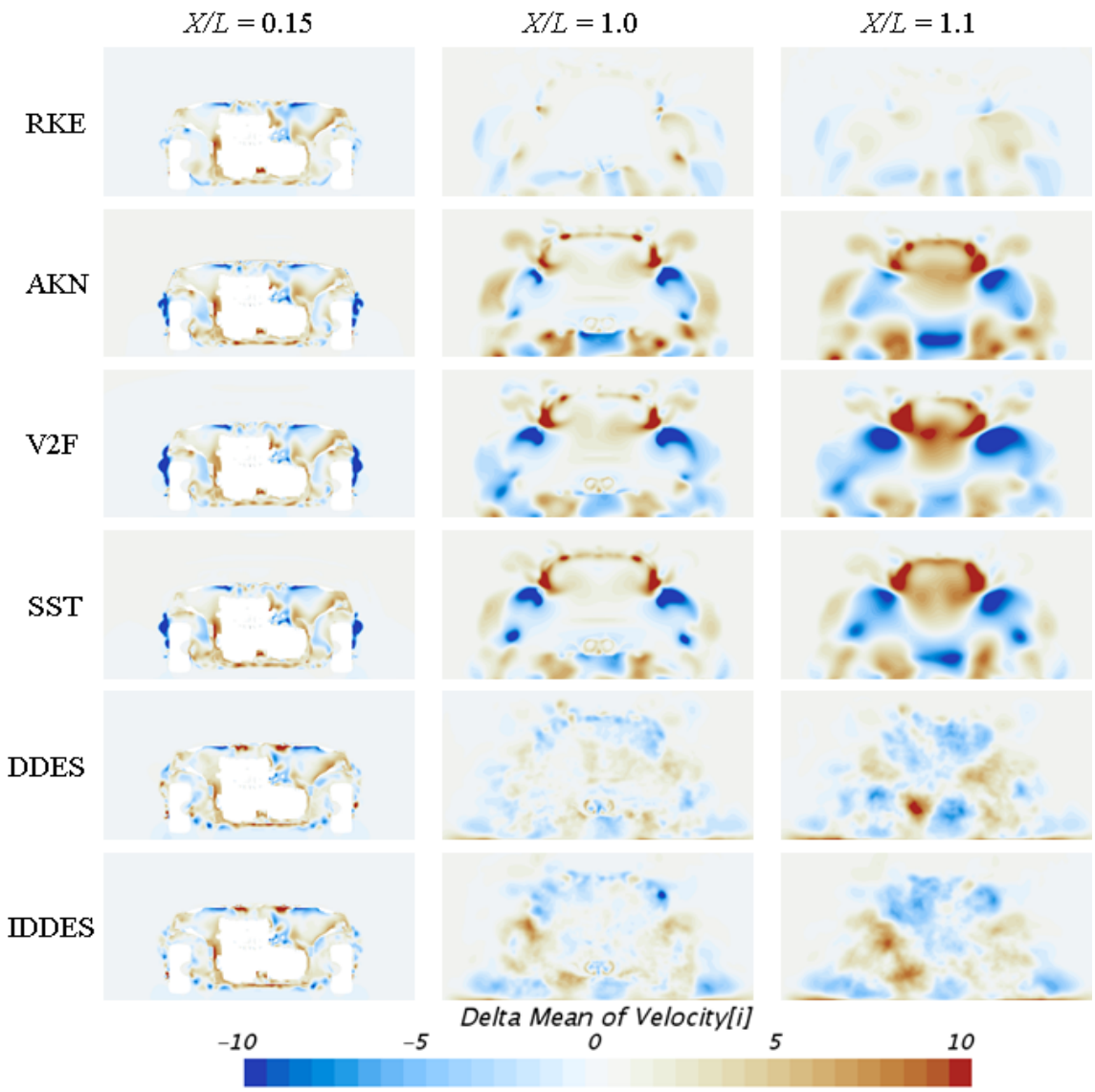

Figure 3.21: Delta streamwise velocity on selected plane sections from all models between case 1 and case 2.

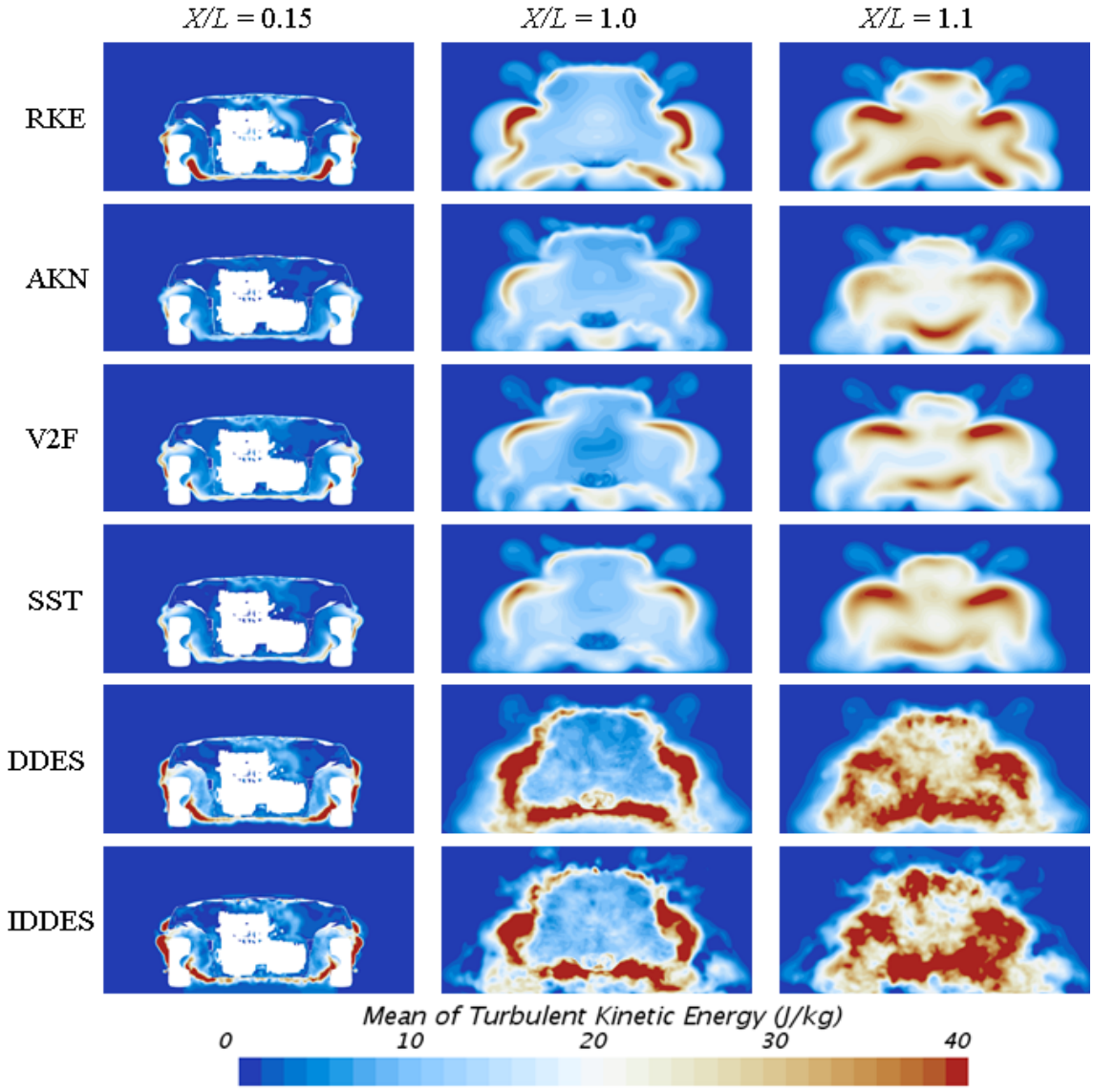

Figure 3.22: Turbulent kinetic energy on selected plane sections from all models for baseline case.

predict a higher level of turbulent kinetic energy; (2) more detailed and complex flow features were resolved by the DES approaches.

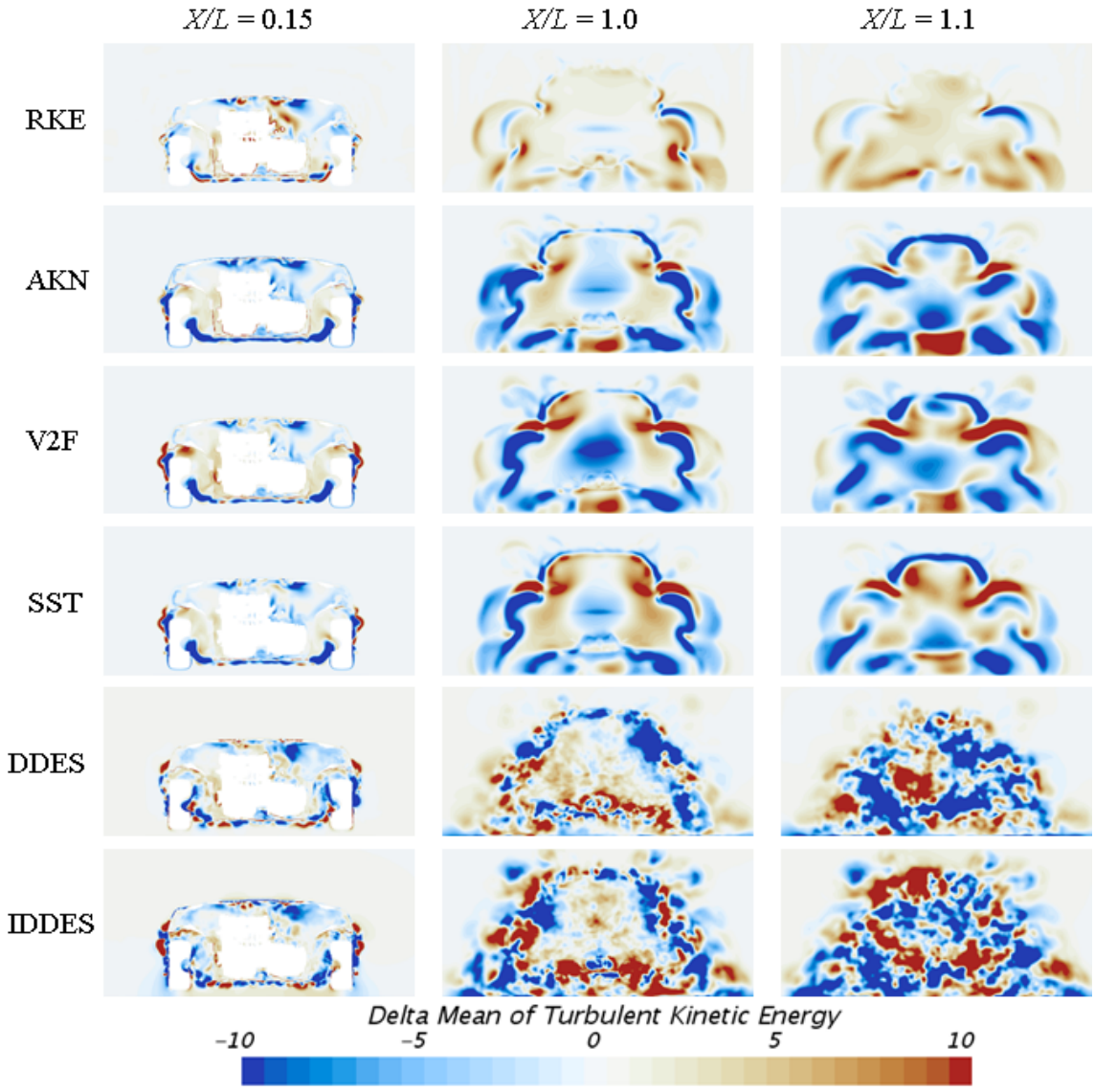

Figure 3.23: Delta turbulent kinetic energy on selected plane sections from all models between case 1 and case 2.

3.5 Conclusion

This study presents a numerical evaluation of various commonly used RANS models and Hybrid RANS/LES models on a full-scale passenger vehicle with two different front-end configurations. The effect of turbulence modeling on the prediction of drag and lift forces, pressure and velocity field, and turbulent kinetic energy were investigated. It was found that, firstly, the RKE model predicted well correlated C_D value for the baseline case, however, all the models investigated still need significant improvement in order to predict the lift values consistently; secondly, despite DES variants not showing superior performance over RANS models for predicting absolute C_D value, they were able to predict more complex flow structures, such as in Figure 3.14 the DDES model predicts a tertiary vortex near the exhaust pipes and the IDDES model predicts a tertiary vortex under the spoiler. Further, the two DES variants are still expected to predict better large scale flow features due to that they are capable of resolving large scale flow features directly. The similarity of the streamwise velocity profile and turbulent kinetic energy distribution on the selected planes between the predictions from the RKE model and the DES variants supports that the RKE model performs better than the other three RANS models for the baseline case.

In summary, for automotive flows which feature complex geometry and exhibit massive separation, the success of CFD simulation still heavily relies on the choice of mesh strategy and turbulent models which in turn depend on the experience of engineers. RANS models might be still a good choice for the prediction of drag values due to their acceptable accuracy, low computational cost and fast turnaround time. However, for applications require predictions of detail flow features, such as aeroacoustic, soiling and water management, the transient DES type approaches would be a better choice.

CHAPTER 4: On Fine Tuning the SST $k-\omega$ Turbulence Model Closure Coefficients for Improved Prediction of Automotive External Flows

4.1 Abstract

Transient Scale Resolved Simulations, such as the Detached Eddy Simulation, are currently seen to be the preferred modeling approach over the steady-state Reynolds Averaged Navier-Stokes (RANS) simulations due to the former's perceived capability of providing more realistic flow field predictions. However, the latter approach is still a widely used methodology in road vehicle aerodynamic developments because of its faster turn-around time and cost-effectiveness. However, RANS models like SST $k-\omega$ generally fail to produce well-correlated predictions. Studies reveal that a good correlation with experiment cannot be achieved by simply refining the mesh when using the SST $k-\omega$ model. As such, this study explores the possibility of improving the prediction veracity by investigating the influence of a few selected model closure coefficients on the CFD prediction. This involves identifying the effect of each individual model parameters on the prediction first, and then formulate the best combination of the model closure coefficient values that yield the best correlation with the experiment. This procedure is applied to four different test objects: NACA 4412 airfoil at 12 degree angle of attack, the 25 and 35 degree slant angle Ahmed body, and a full-scale passenger road vehicle. Although some closure coefficients do not influence the CFD results much, the predictions are very sensitive to the choice of certain model constants irrespective of the test object geometry. The study also shows that it is possible to formulate a combination of closure model coefficients that can produce very well correlated CFD predictions.

4.2 INTRODUCTION

Nowadays, computational fluid dynamics (CFD) has become a very important tool in a wide range of industrial applications. This can partly be attributed to the rapid development of computer technology, making CFD simulations using a highly refined mesh and higher-order turbulence models affordable. For automotive flows, it has become a common practice to run scale resolved (SRS) and scale averaged (SAS) CFD simulations with around 100 million cells during the initial stages of road vehicle design process. A number of recent works evaluating the steady-state Reynolds Averaged Navier-Stokes (RANS) and transient Detached Eddy Simulation (DES) approaches on the prediction of automotive flows have found that DES approaches generally perform better than RANS approaches, in terms of integral flow quantities and flow features. However, the computational cost of DES approaches is an order of magnitude higher than that of RANS approaches [60, 61, 62]. Therefore, RANS models are still widely used in the automotive industry, especially during the early stages of road vehicle design, where hundreds of configurations need to be considered.

Most commonly used RANS approaches in the automotive industry are variants of $k-\epsilon$ and $k-\omega$ models. The standard $k-\epsilon$ model was proposed by Jones and Launder [34] with coefficients suggested by Launder and Sharma [35]. Existing literature suggests that there are two main flaws in the original $k-\epsilon$ model. Firstly, it may predict an anomalously large growth of turbulent kinetic energy in areas near the stagnation point, which is called the stagnation point anomaly. The stagnation point anomaly may be due to the fact that the linear eddy viscosity formulation gives an erroneous difference in normal stress. This anomaly can be ameliorated by imposing the "realizability" constraint on the normal stresses [28, 29]. Secondly, it can not be applied to the viscous-affected layer. This problem is mainly addressed by two common approaches: the Low-Reynolds Number Approach and the Two-Layer Approach [36]. Since the inception of the $k-\epsilon$ model, countless attempts have been

made to improve it. Some of the most significant improvements are the AKN $k-\epsilon$ Low-Reynolds model [22] and the Realizable $k-\epsilon$ [21]. The $k-\omega$ model was first proposed by Wilcox [32] in 1988. The most significant advantage of the $k-\omega$ model is that it may be applied throughout the boundary layer without further modification. However, one of the problems of the original $k-\omega$ model is the sensitivity to free-stream/inlet conditions. This problem was addressed by Menter in his introduction of the SST (shear-stress transport) $k-\omega$ model [24]. The SST $k-\omega$ model, SST for short hereinafter, effectively blends a $k-\epsilon$ model in the far-field with a $k-\omega$ model near the wall. Therefore, it can be applied throughout the boundary layer without encountering the problem of sensitivity to free-stream/inlet conditions.

Both of $k-\epsilon$ and $k-\omega$ models belong to the two-equation eddy-viscosity RANS category. The two-equation models were developed mainly on the basis of dimensional analysis. The postulation of transport equations of the two-equation RANS models involves unknown double and triple correlations. Those unknowns have been replaced with algebraic expressions involving known turbulence and mean-flow properties by introducing closure coefficients. For example, the $k-\omega$ model has six coefficients, viz., α, β_0, β^*, σ, σ^* and σ_{d0}. Therefore, the two-equation RANS models are not exact. Consequently, the values of the closure coefficients were set by assuring agreement with observed properties of turbulence from canonical flows. For instance, the ratio of β^* to β_0 was established by applying the $k-\omega$ model to decaying homogeneous, isotropic turbulence.

Considering the way that the values of closure coefficients of the two-equation RANS models were determined, it is not surprising that the RANS models often fail to correctly predict automotive flows which feature complex geometry and exhibit massive flow separations. Furthermore, even the transient DES models, for computational realizability, adopt the RANS simplification in the regions very close to solid walls. These motivate the authors to investigate the possibility of improving the pre-

diction of automotive flows by tuning the SST model closure coefficients where the sensitivity of five important closure coefficients, viz., β^*, $\sigma_{\omega 1}$, $\sigma_{\omega 2}$, σ_{k1}, and σ_{k2} were investigated. These coefficients, which will be defined later, have a direct influence on some of the most important terms in the transport equations, such as the production, the dissipation, the diffusion and the cross-diffusion terms. The sensitivity of drag and lift forces, and the overall flow fields to the value of these coefficients were analyzed for three test cases, viz. NACA wing 4412 at an angle of attack of 12 degree, the Ahmed body with 25 and 35 degree slant angle, and a full-scale passenger vehicle 2014 Hyundai Veloster. The main goal of this study is to provide general suggestions on how to select a better combination of the SST model coefficients for improved drag and lift force predictions associated with automotive flows.

4.3 GOVERNING EQUATIONS AND CLOSURE COEFFICIENTS

For incompressible low-Mach number flow, two-equation RANS SST approach is based off the continuity, three momentum, and two additional transport equations for the turbulent kinetic energy (k) and specific dissipation rate ω. The steady-state continuity and momentum equations can be written using Einstein notation, as

$$\frac{\partial U_i}{\partial x_i} = 0 \tag{4.1}$$

$$\rho U_j \frac{\partial U_i}{\partial x_j} = \rho \bar{f}_i + \frac{\partial}{\partial x_j}[-P\delta_{ij} + 2\mu S_{ij} - \rho\overline{u_i u_j}] \tag{4.2}$$

where the symbols U, P x, μ and ρ have their usual meanings, δ_{ij} stands for the Kronecker delta, $\bar{f}_i$ is the resultant of the body forces (such as gravity and centrifugal forces), and $S_{ij} \equiv (1/2)(\partial U_i/\partial x_j + \partial U_j/\partial x_i)$ is the mean strain rate tensor. The additional terms $-\rho\overline{u_i u_j}$ in (4.2) are known as the Reynolds stress terms which are due to the fluctuating velocity field. Using the Reynolds decomposition, a time-dependent quantity $\tilde{v}$ can be written as $\tilde{v}(t) = V + v(t)$, where V is the time-averaged

value of $\tilde{v}(t)$ and $v(t)$ is the fluctuating component. The nonlinear Reynolds stress terms require additional modeling for closure which can be achieved using a number of turbulence modeling approaches, for details see [2]. One basic approach is the Eddy Viscosity Model (EVM) which is based on the analogy between the molecular gradient-diffusion process and turbulent motion, and by using the Boussinesq approximation, the Reynolds stress tensor is modeled as a function of mean flow quantities by the concept of turbulent eddy viscosity, ν_t.

The SST model, proposed by Menter and his coworkers [82, 24], has enjoyed a remarkable success in separated flow predictions [83]. The SST model effectively blends a $k-\epsilon$ model in far-field with a $k-\omega$ model near the wall. The expressions for the eddy viscosity, ν_t, and the transport equations of the SST model are given in equations 4.3 through 4.13.

$$\nu_t = \frac{a_1 k}{\max\left(a_1\omega, SF_2\right)} \tag{4.3}$$

$$U_j\frac{\partial k}{\partial x_j} = P_k - \beta^* k\omega + \frac{\partial}{\partial x_j}[(\nu+\sigma_k\nu_t)\frac{\partial k}{\partial x_j}] \tag{4.4}$$

$$U_j\frac{\partial \omega}{\partial x_j} = \gamma S^2 - \beta\omega^2 + \frac{\partial}{\partial x_j}[(\nu+\sigma_\omega\nu_t)\frac{\partial \omega}{\partial x_j}] + 2(1-F_1)\sigma_{\omega 2}\frac{1}{\omega}\frac{\partial k}{\partial x_i}\frac{\partial \omega}{\partial x_i} \tag{4.5}$$

$$P_k = \nu_t S^2 \tag{4.6}$$

$$S = \sqrt{2S_{ij}S_{ij}} \tag{4.7}$$

$$F_1 = \tanh\{\{\min[\max(\frac{\sqrt{k}}{0.09\omega d}, \frac{500\nu}{d^2\omega}), \frac{2k}{CD_{k\omega}d^2}]\}^4\} \tag{4.8}$$

$$F_2 = \tanh[[\max(\frac{2\sqrt{k}}{\beta^*\omega d}, \frac{500\nu}{d^2\omega})]^2] \tag{4.9}$$

$$CD_{k\omega} = \max(\frac{1}{\omega}\frac{\partial k}{\partial x_i}\frac{\partial \omega}{\partial x_i}, 10^{-20}) \tag{4.10}$$

$$\gamma = F_1\gamma_1 + (1-F_1)\gamma_2 \tag{4.11}$$

$$\gamma_1 = \frac{\beta_1}{\beta^*} - \sigma_{\omega 1}\frac{\kappa^2}{\sqrt{\beta^*}} \tag{4.12}$$

$$\gamma_2 = \frac{\beta_2}{\beta^*} - \sigma_{\omega 2}\frac{\kappa^2}{\sqrt{\beta^*}} \tag{4.13}$$

where F_1 and F_2 are blending functions; α, β, β^*, σ_k, σ_ω and $\sigma_{\omega 2}$ are closure coefficients. The blending function F_1 combines the near-wall contribution of a coefficient with its value far away from the wall, e.g. $\sigma_k = F_1 \times \sigma_{k1} + (1 - F_1) \times \sigma_{k2}$. The implementation of this model in STAR-CCM+ uses the values of these closure coefficients as defined by [82].

A total of five SST closure coefficients, β^*, $\sigma_{\omega 1}$, $\sigma_{\omega 2}$, σ_{k1} and σ_{k2}, were selected for investigating their effects on the flow prediction. As listed in Table 4.1, four values for each coefficient were investigated in addition to the case involving the default values of all closure coefficients as used in the commercial code Star-CCM+ (version 12.06) which is used for running all simulations presented in this paper. Also, unless specified otherwise, only one coefficient was changed at a time keeping the other coefficients at their default values. Thus, for each test geometry, a total of 21 simulations were run. In Table 4.1, test cases involving the variations of β^*, $\sigma_{\omega 1}$, $\sigma_{\omega 2}$, σ_{k1}, and σ_{k2} are given a letter-prefix identifications of A, B, C, D and E respectively; the second row of the table indicates this letter ID. Then each of these cases is assigned a "value number ID" with value number ID equal to 3 representing the default case. Using this notation the case with default $\sigma_{\omega 2}$ value will have the case ID of C3. As such, value number ID's less than 3 will have respective coefficient values less than the default value, while those with larger than 3 have coefficient values greater than the default case; this also means that an increasing value number ID implies an increasing value of the closure coefficient.

4.4 TEST CASES AND SIMULATION DETAILS

4.4.1 NACA 4412 Airfoil

The first test geometry is the NACA 4412 airfoil, which has a maximum camber of 4% located 40% (0.4 chords) from the leading edge with a maximum thickness of 12%

Table 4.1: SST $k-\omega$ model coefficients investigated.

Value #	β^*	$\sigma_{\omega 1}$	$\sigma_{\omega 2}$	σ_{k1}	σ_{k2}
	A	**B**	**C**	**D**	**E**
1	0.05	0.4	0.712	0.7	0.8
2	0.07	0.45	0.784	0.775	0.9
3	**0.09**	**0.5**	**0.856**	**0.85**	**1.0**
4	0.11	0.55	0.928	0.925	1.1
5	0.13	0.6	1.0	1.0	1.2

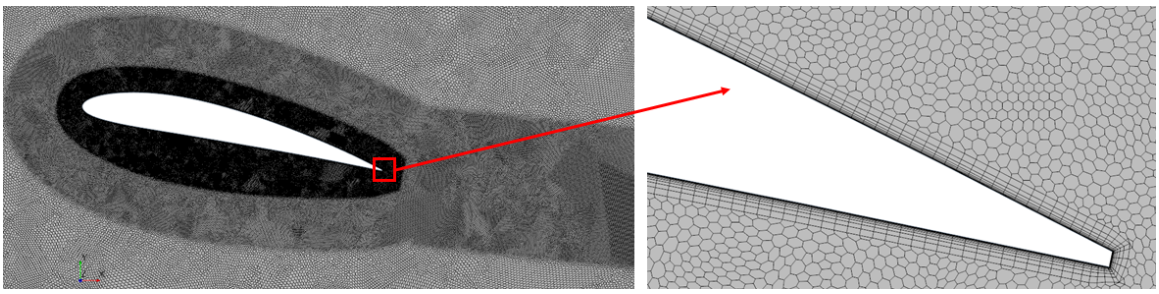

Figure 4.1: 2D mesh of NACA 4412 airfoil at 12 degree angle of attack.

at 40% chord. 2D mesh with polygonal mesher was used to discretize the simulation domain. The core mesh size is 2 mm around the airfoil and 4 mm behind it, up to 10 chord widths downstream (see Figure 4.1). In addition, to properly resolve the flow in the areas of high gradient, close to the airfoil surface, 18 prism layers with the first node height of 0.001 mm and the total thickness of 3 mm were applied to the external surface of the airfoil; this gives a simulation domain with 1.1 million cells. At a Reynolds number of 6×10^6 used in this study, this prism layer setting resulted in wall-node y^+ values less than 0.5 everywhere on the external surface of the airfoil.

4.4.2 Ahmed Body

The Ahmed body, as shown in Figure 4.2, is a commonly used simplified generic car body introduced first in 1984 by Ahmed et al. to analyze the key flow features of ground vehicles [66]. The Ahmed body is comprised of a flat front with rounded corners and a sharply slanted rear upper surface with fixed length at various angles. Despite the overly simplified geometry compared to a full-scale vehicle, some broad aerodynamic features of the Ahmed body resemble a ground vehicle, e.g. the flow separation on the rear glass or the wake structures. The main model variable for the Ahmed body is the angle of rear slant surface. This angle has a strong influence on the flow patterns over the rear slant, the wake structure behind the body, and the integral flow quantities such as drag and lift forces. The influence of the slant angle has been intensively investigated using both experimental and numerical approaches. In his initial work of the Ahmed body, [66] showed that the maximum drag is found at the critical slant angle of 30 degree. Above this angle, the flow fully separates over the slant surface. Below this critical angle, especially at 25 degree, the flow has proven to be very complex and challenging for CFD simulations. At this angle, the flow that partially separates from the upstream part of the slant can reattach further downstream, thus forming a confined recirculation zone over the rear slant. Moreover, the wake structure becomes very complex due to the interaction of the separation zone and streamwise counter-rotating vortices at the lateral slant edges. For this configuration, all RANS and DES investigations in the literature failed to correctly predict the flow field, drag and lift forces [67, 68, 69, 70].

In the present study, the Ahmed body with 25 and 35 degree slant angle were simulated in a large, $60L \times 10L \times 10L$, virtual tunnel, where L represents the length of the Ahmed body. The entrance of the virtual tunnel was placed at $10L$ upstream and defined as a velocity inlet boundary with a speed of 40 m/s; this corresponds to a Reynolds number of 2.784×10^6 based on L and free-stream velocity.

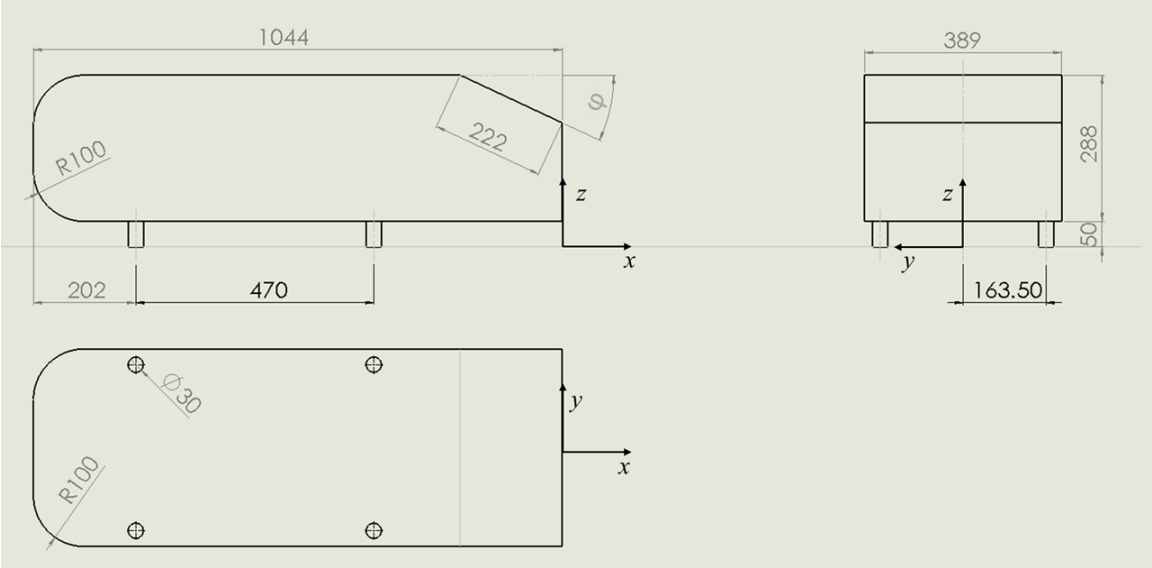

Figure 4.2: Ahmed body dimensions, where $\varphi = 25$ or 35 degree

The volume mesh was composed of primarily hexahedral cells generated by a trim-cell mesher in Star-CCM+. The core mesh size is 2 mm around the Ahmed body (see Figure 4.3). For the Reynolds number used in the current work, the 2 mm core mesh size is smaller than the Taylor microscale ($\lambda_T \approx 5.5 \times Re^{-0.5} = 3.3$ mm [81]) implying that the resultant mesh is suitable for even DES type simulations. In order to properly resolve the flow in areas of high gradient close to the solid surface, 16 prism layers with the first node height of 0.005 mm and a total thickness of 6 mm were applied on the external surface which resulted in a total of 39 million cells. At the operating Reynolds number of 2.784×10^6, the settings used in the mesh generation resulted in wall y^+ values less than 1 over the entire external surface of the Ahmed body.

4.4.3 Full-Scale Real Life Road Vehicle

The real-life road vehicle model investigated in this study is a full-scale 2014 Hyundai Veloster with detailed underhood and underbody components as shown in Figure 4.4. It was simulated in a very large minimal blockage virtual wind tunnel as shown in Figure 4.5. The dimensions of this vehicle are 4220 mm, 1800 mm and

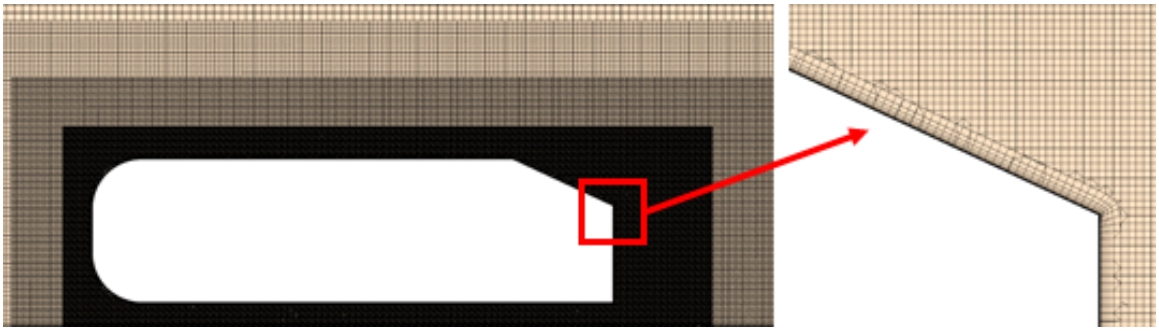

Figure 4.3: The mesh on the central plane through the Ahmed body with 25 degree slant angle.

1400 mm for length (L), width, and height respectively, with a front ground clearance of 143 mm; please see [37] for vehicle details. The airflow inlet was placed at 5 L upstream the vehicle and the outlet was placed at 20 L downstream; the width and height of the tunnel are 10 L and 5 L respectively. While the portion of the ground in green color in Figure 4.5 was specified as slip wall, the floor in orange was applied a moving wall boundary condition with a tangential speed same as the inlet air velocity which was set at a typical highway speed of 70 mph; top and side walls were modeled as symmetry planes.

The volume mesh primarily consists of hexahedral cells generated by the trim-mesher in Star-CCM+. Twelve prism layers with the first node height of 0.005 mm and a total thickness of 6 mm were applied to the external surfaces of the vehicle and the floor. With the object of achieving a good balance between accuracy and computational cost, mesh refinement was chosen to use volume sources that follow the external shape of the vehicle. The core mesh size around the vehicle is 6 mm. These mesh settings resulted in a high-quality volume mesh with 71 million cells. In order to eliminate the influence of mesh size on the simulation results, a mesh independence study was conducted. A fine mesh was generated by reducing base size from 24 mm to 20 mm, resulting in a total of 100 million cells. The change of drag coefficient between the coarse and fine mesh case was within 1%. Thus, the coarse mesh setting was used for all real vehicle simulations. The mesh on the central plane

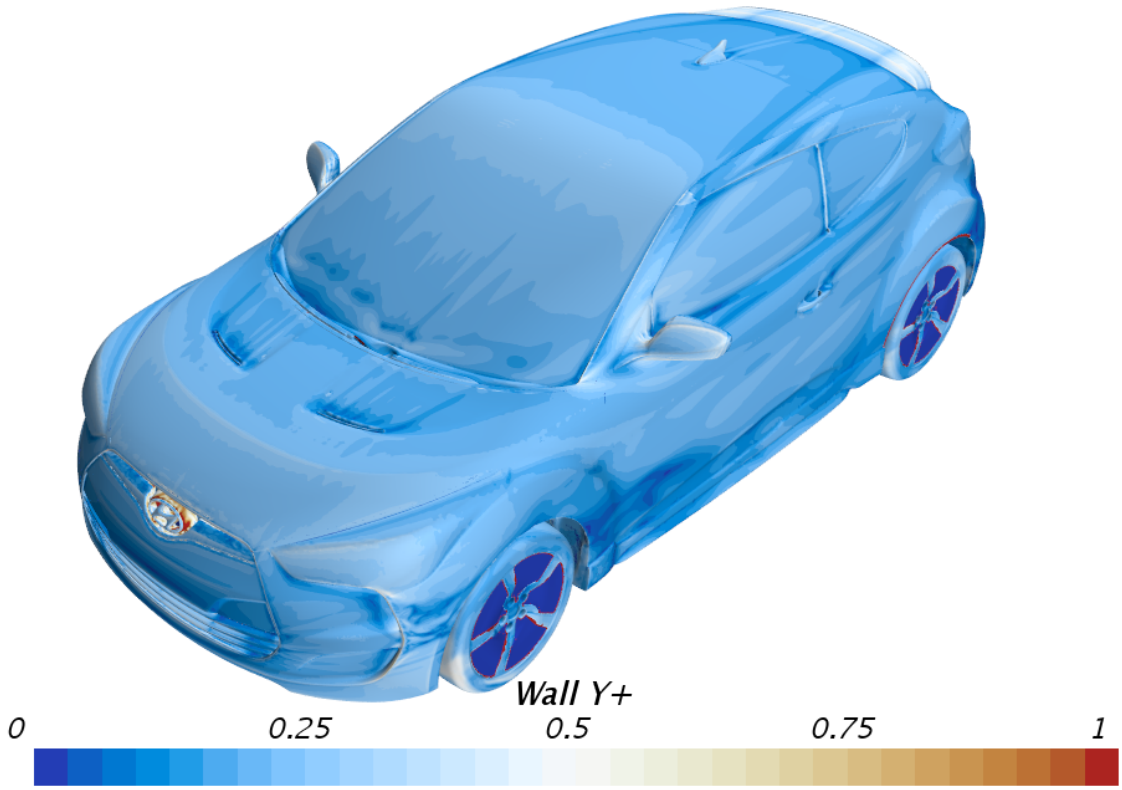

Figure 4.4: The wall y^+ values on the external surfaces of the vehicle.

of the vehicle is shown in Figure 4.6. Using the above settings, the y^+ values on the external surfaces of the vehicle were mostly less than 0.5, as can be seen in Figure 4.4.

For the cooling module, the condenser and radiator were simulated using the porous media model. The cooling fan rotation was modeled using the moving reference frame (MRF) method. The wheel rotation was simulated by a combination of a moving wall boundary on the tire and a MRF method in the regions between the spokes.

4.5 RESULTS AND DISCUSSION

4.5.1 NACA 4412 Airfoil

The CFD predictions and experimental measurements [3] for drag and lift coefficients of NACA 4412 airfoil at various angle of attack are shown in Figures 4.7 and 4.8 respectively. While CFD simulations predict both higher C_D and C_L values than

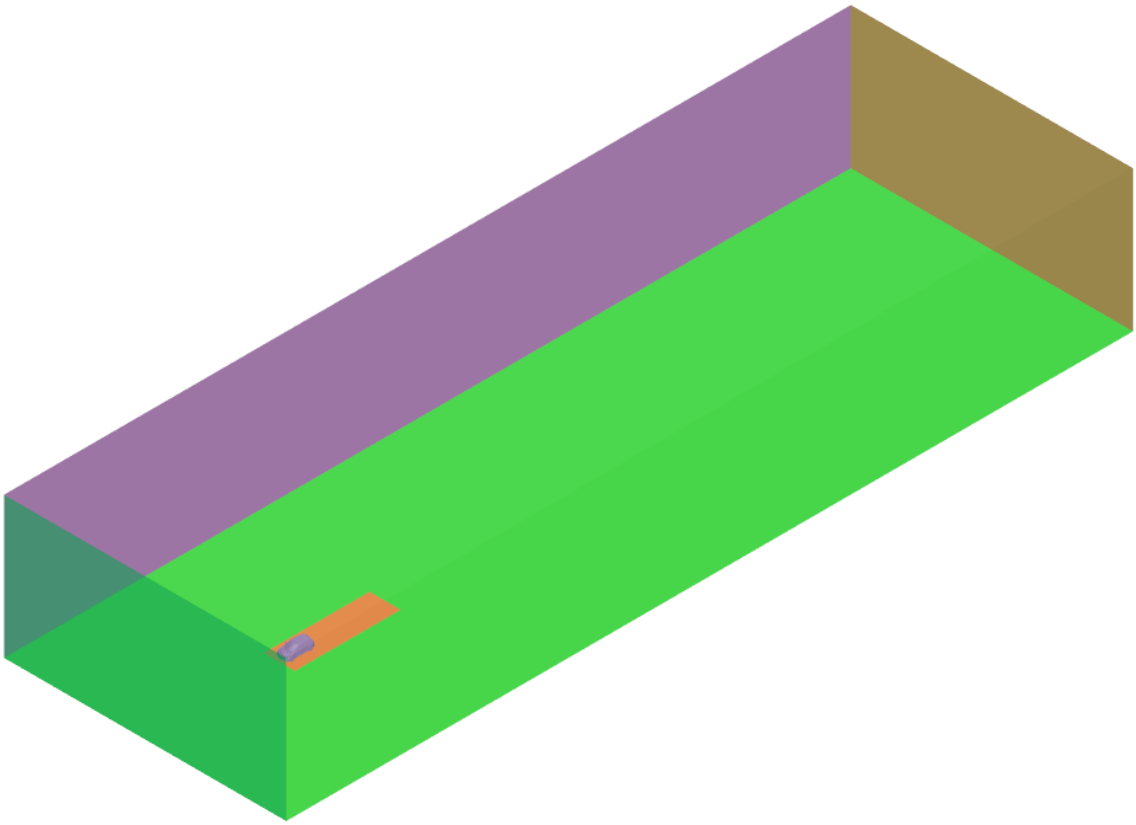

Figure 4.5: Computational domain for the real life full-scale road vehicle model.

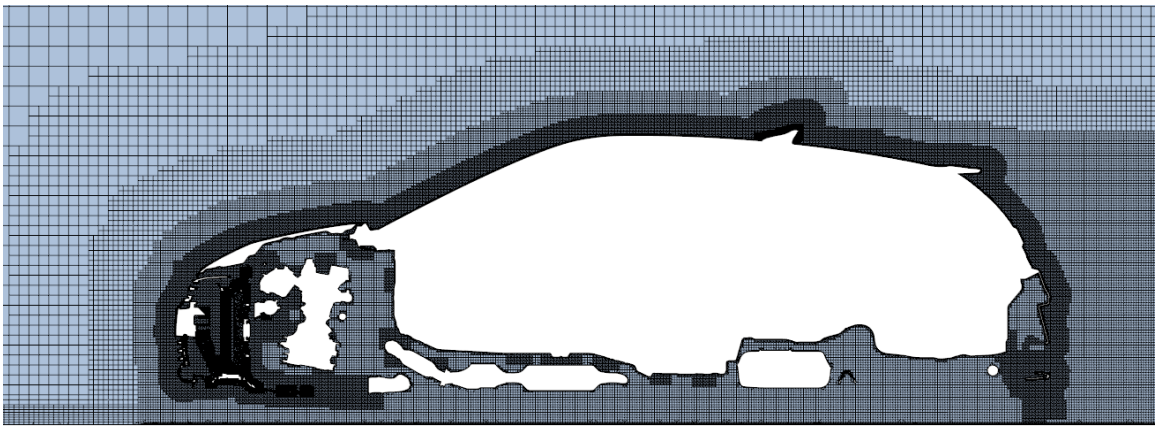

Figure 4.6: Mesh distribution on the central plane of the test road vehicle.

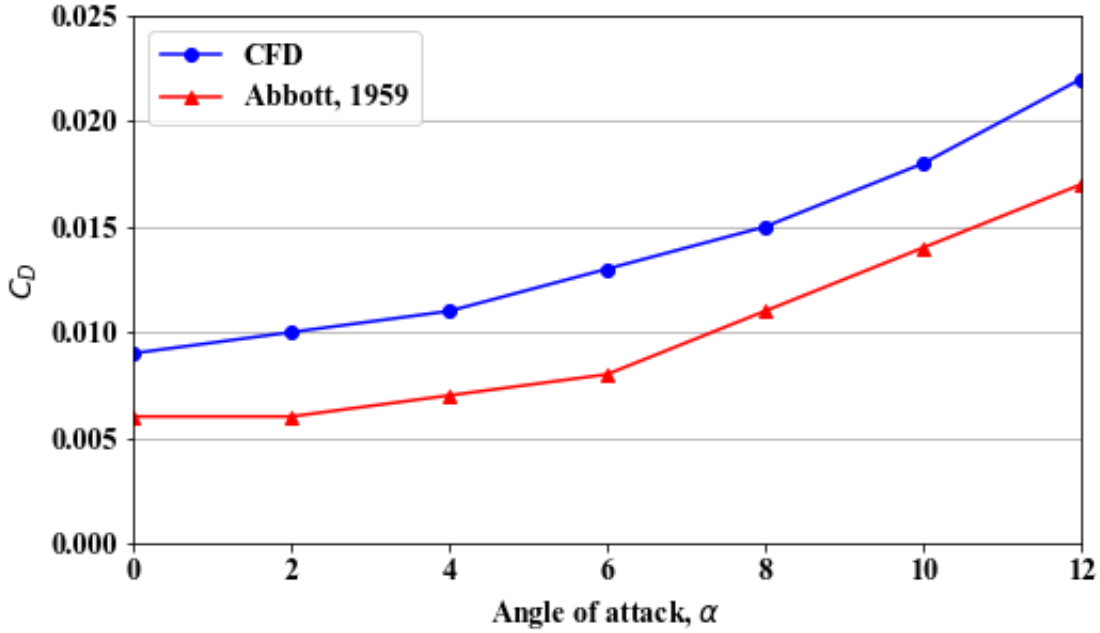

Figure 4.7: C_D Vs. angle of attack for NACA 4412 airfoil; experimental data are from [3].

that of the experiment, the trends agree very well with the experimental data even at higher angles of attack.

The angle of attack at 12 degree was chosen to investigate the influence of the selected SST model coefficients on the prediction of C_D and C_L. At this angle of attack, the experimental C_D and C_L values are 0.017 and 1.543 respectively [3]. The C_D and C_L values from all cases are listed in Table 4.2. It can be seen that all investigated coefficients generally have a stronger influence on the lift prediction than on drag. It appears that C_D is very little sensitive to the model closure coefficient values, except β^*. In general, drag decreases toward the experimental value as β^* increases. Percent relative deviations of the CFD predicted C_L (labeled as Delta C_L on the vertical axis) from the experimental value are graphically summarized in Figure 4.9 where the difference between the CFD predicted and experimental values are normalized by the latter. It can be seen that $\sigma_{\omega 1}$, σ_{k1} and σ_{k2} have little influence on the lift prediction. However, C_L decreases slightly toward the experimental value

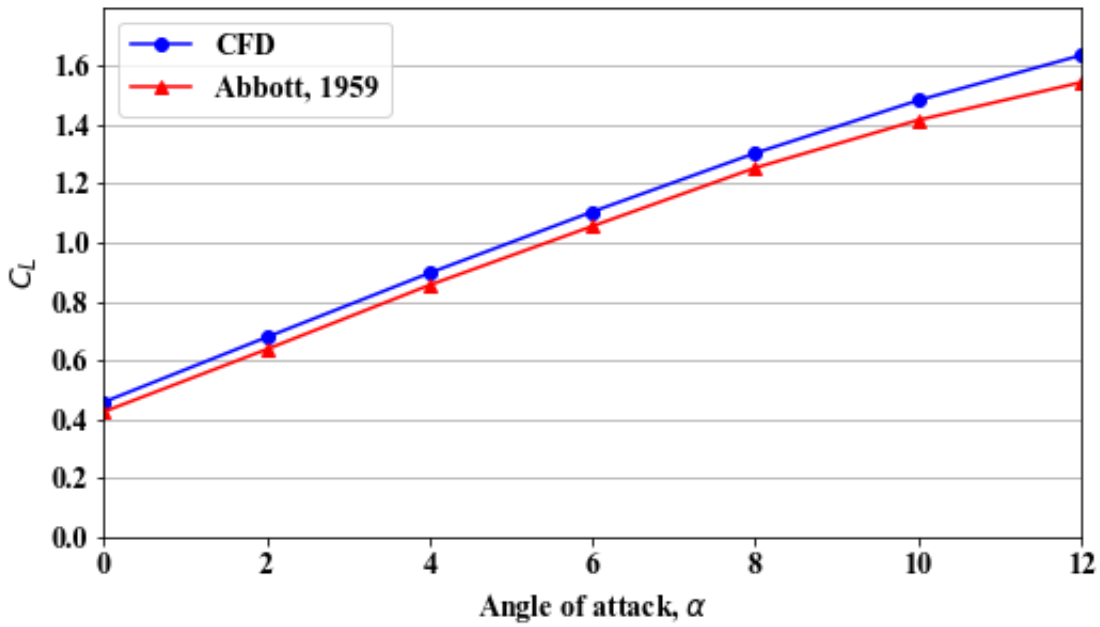

Figure 4.8: C_L Vs. angle of attack for NACA 4412 airfoil; experimental data are from [3]

as $\sigma_{\omega 2}$ decreases. It appears that $\beta^* = 0.07$ produces the highest lift coefficient which decreases with both increasing and decreasing value of β^*.

A change in the value of β^* can cause a drastic change in the flow field prediction. The flow separation predicted by the default case (A3) and $\beta^* = 0.13$ case (A5) are shown in Figure 4.10. It can be seen that, compared to the default case, A5 predicts a significantly larger separation bubble. In short, for the NACA 4412 airfoil at a high angle of attack ($\alpha = 12$), the drag prediction is insensitive to the change of investigated coefficients, except for β^*, i.e. the SST model is quite robust for the drag prediction of streamlined geometry. However, compared to the drag prediction, lift prediction shows a stronger dependence on the value of the closure coefficients, especially β^*. Amongst all β^* has the strongest influence on the prediction of drag, lift and flow field, even for such a simplified streamlined geometry. Therefore, despite increasing β^* leading to a better prediction of both C_D and C_L in this case, it should be cautioned that a change in this coefficient for other applications may lead to

Table 4.2: Turbulence model closure coefficient sensitivity of drag and lift predictions of NACA 4412 airfoil at $\alpha = 12$.

Value #	1	2	3	4	5
β^*	0.05	0.07	0.09	0.11	0.13
C_D	0.022	0.022	0.022	0.02	0.019
C_L	1.637	1.656	1.635	1.6	1.561
$\sigma_{\omega 1}$	0.4	0.45	0.5	0.55	0.6
C_D	0.021	0.021	0.022	0.022	0.022
C_L	1.629	1.632	1.635	1.638	1.64
$\sigma_{\omega 2}$	0.712	0.784	0.856	0.928	1.0
C_D	0.022	0.022	0.022	0.022	0.022
C_L	1.629	1.632	1.635	1.638	1.64
σ_{k1}	0.7	0.775	0.85	0.925	1.0
C_D	0.022	0.022	0.022	0.022	0.022
C_L	1.637	1.636	1.635	1.634	1.633
σ_{k2}	0.8	0.9	1.0	1.1	1.2
C_D	0.022	0.022	0.022	0.022	0.022
C_L	1.635	1.635	1.635	1.635	1.635

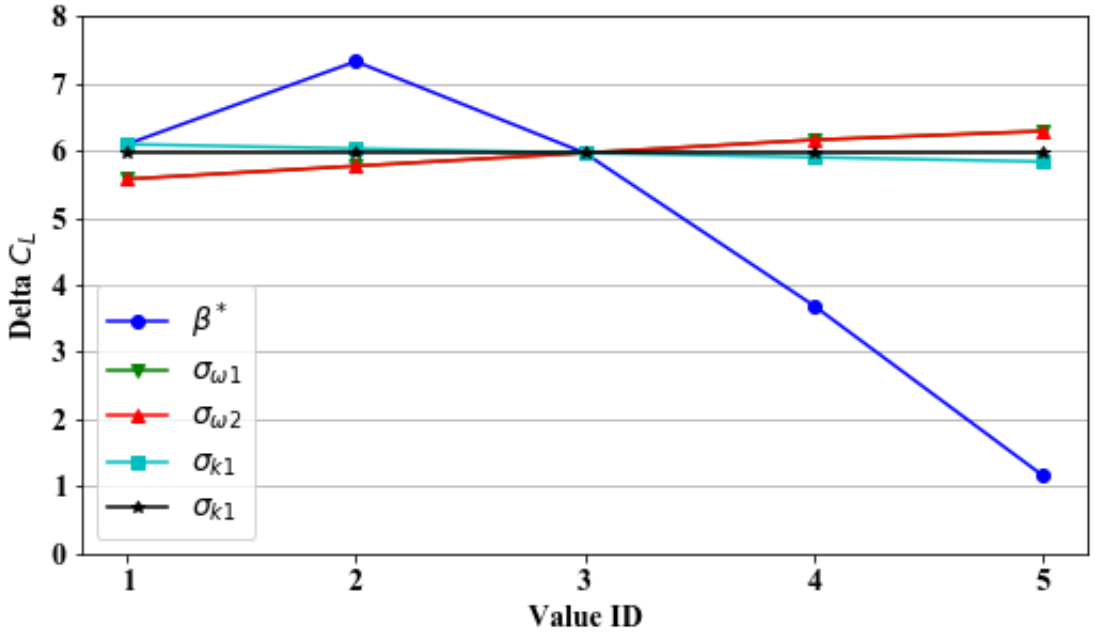

Figure 4.9: Percent relative deviation of the CFD predicted C_L from the experimental value of [3]; see table 4.1 for the actual values of the coefficients corresponding to a case Value ID.

undesirable consequences since RANS models, in general, are often case dependent.

4.5.2 Ahmed Body with 25 Degree Slant Angle

The present study used the same Reynolds number and boundary treatment on the floor as used in [4], therefore the work of [4] will be used as the reference for validation and correlation. The drag and lift force coefficients from the present study, using the default model coefficients, along with the experimental data are presented in Table 4.3. It can be seen that, compared to the experimental data of [4], CFD predicted an 8.7% lower C_D; much worse, the predicted C_L value is an order of magnitude lower.

The C_D and C_L values from all cases are listed in Table 4.4. To better present the data, the deviation of the CFD predicted force coefficient from the respective experimental value [4], normalized by the latter, is graphically summarized in Figure 4.11 for drag and Figure 4.12 for lift. For drag prediction, firstly, the changes of $\sigma_{\omega 1}$, σ_{k1} and σ_{k2} show little influence on the prediction. However, the coefficients β^*

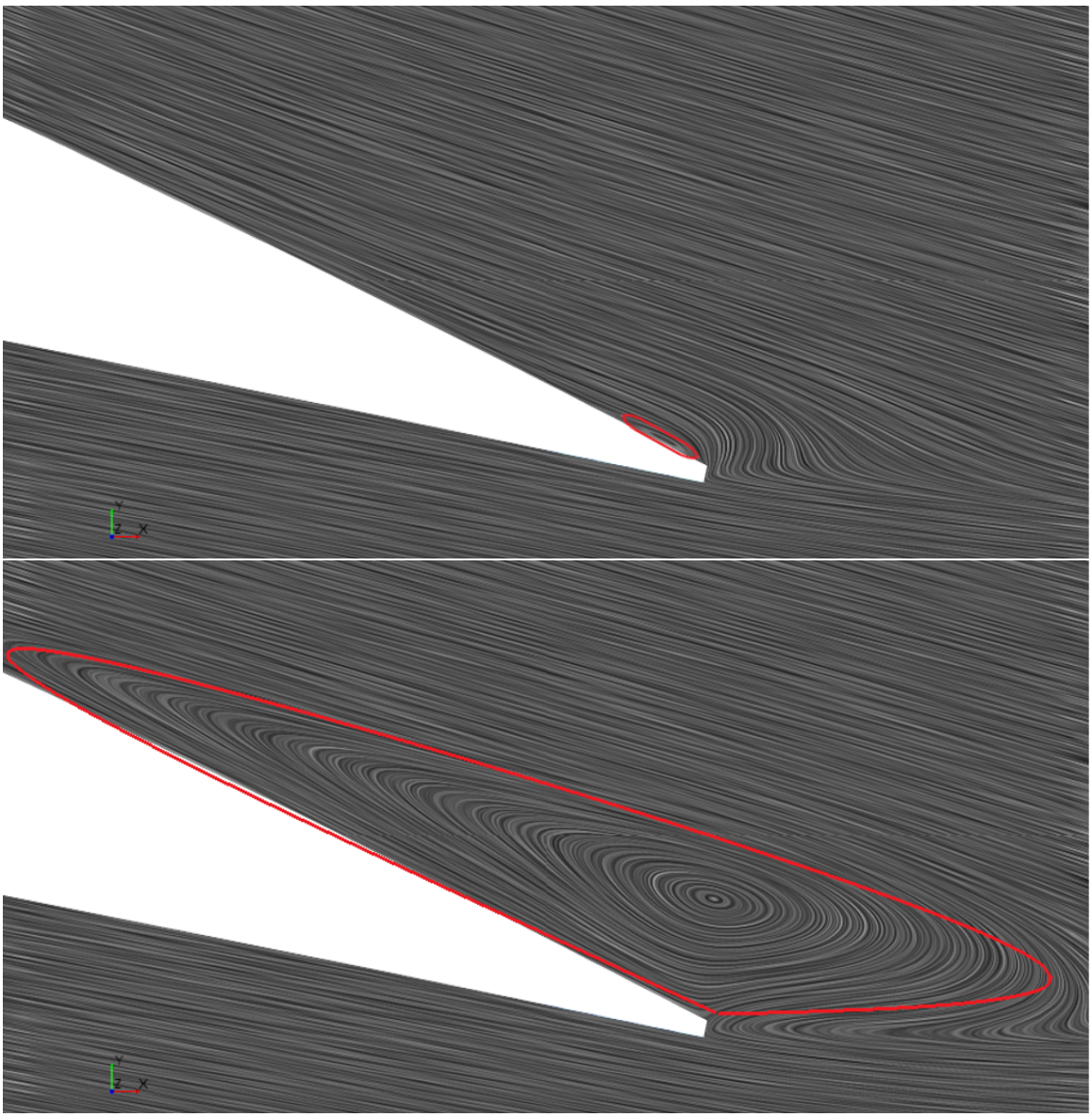

Figure 4.10: Separation bubble (marked by red line) at the rear end of NACA 4412 airfoil at $\alpha = 12$ predicted by SST model using: (Top) default coefficients; (Bottom) $\beta^* = 0.13$.

Table 4.3: C_D and C_L from current CFD simulations with default model coefficients compared against experimental values.

	CFD	Expt. [4]	Difference
C_D	0.273	0.299	-8.7%
C_L	0.038	0.345	-89%

and $\sigma_{\omega 2}$ show noticeable influence on the C_D prediction. While C_D value increases smoothly toward the experimental value as $\sigma_{\omega 2}$ increases, the effect of changing β^* is rather interesting. It appears that in the range $0.07 \leq \beta^* \leq 0.11$, which is around the default value of $\beta^* = 0.09$, there is no appreciable dependence of drag predictions on β^*; although the default value appears to predict the minimum drag in this bound. However, changing β^* blow 0.07 and above 0.11 cause drastic under and over prediction of C_D respectively. For lift predictions, firstly, the changes of $\sigma_{\omega 1}$, σ_{k1} and σ_{k2} show little influence. However, the C_L value increases slightly toward the experimental value as $\sigma_{\omega 1}$ increases. Moreover, while the coefficients β^* and $\sigma_{\omega 2}$ show noticeable effect. Again, while C_L value increases smoothly toward the experimental value as $\sigma_{\omega 2}$ increases, there is no clear trend exists by changing β^*, and the change of β^* shows an erratic influence on the C_L value. Furthermore, from Table 4.4, for $\sigma_{\omega 2} = 0.712$, $\beta^* = 0.05$ and $\beta^* = 0.11$, the predicted C_L values are negative which is unphysical. Therefore, for lift prediction, decreasing $\sigma_{\omega 2}$ may lead to unphysical values and no consistent conclusion can be reached by changing β^*.

It can be seen from the results above that clear trends toward the experimental value exist by increasing $\sigma_{\omega 1}$ and $\sigma_{\omega 2}$. In addition, $\beta^* = 0.07$ gives better C_D and C_L predictions than the one obtained using the default value. Therefore, the authors speculated that continuing to increase $\sigma_{\omega 1}$ and $\sigma_{\omega 2}$ with a combination of $\beta^* = 0.07$

Table 4.4: The C_D and C_L values for Ahmed body with 25 degree slant angle from all cases.

Value #	1	2	3	4	5
β^*	0.05	0.07	0.09	0.11	0.13
C_D	0.249	0.277	0.273	0.285	0.386
C_L	-0.009	0.139	0.038	-0.029	0.332
$\sigma_{\omega 1}$	0.4	0.45	0.5	0.55	0.6
C_D	0.272	0.272	0.273	0.274	0.275
C_L	0.038	0.036	0.038	0.049	0.055
$\sigma_{\omega 2}$	0.712	0.784	0.856	0.928	1
C_D	0.259	0.264	0.273	0.281	0.286
C_L	-0.003	0.012	0.038	0.076	0.112
σ_{k1}	0.7	0.775	0.85	0.925	1
C_D	0.274	0.273	0.273	0.272	0.272
C_L	0.051	0.045	0.038	0.036	0.035
σ_{k2}	0.8	0.9	1	1.1	1.2
C_D	0.272	0.273	0.273	0.273	0.273
C_L	0.033	0.038	0.038	0.043	0.043

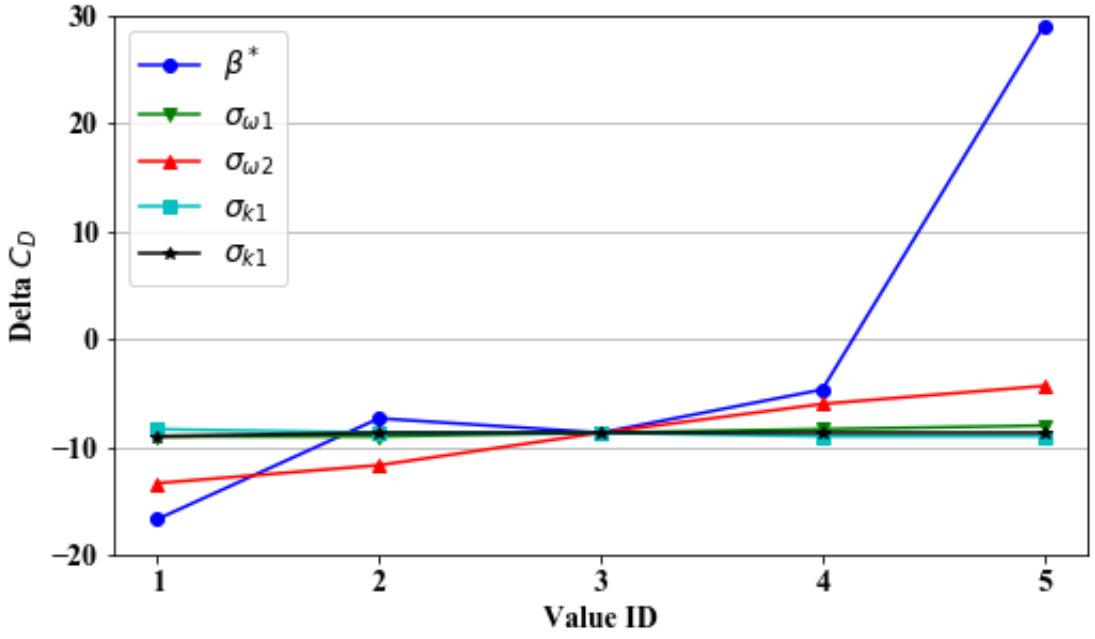

Figure 4.11: Percent relative deviation of the CFD predicted C_D from the experimental value of [4].

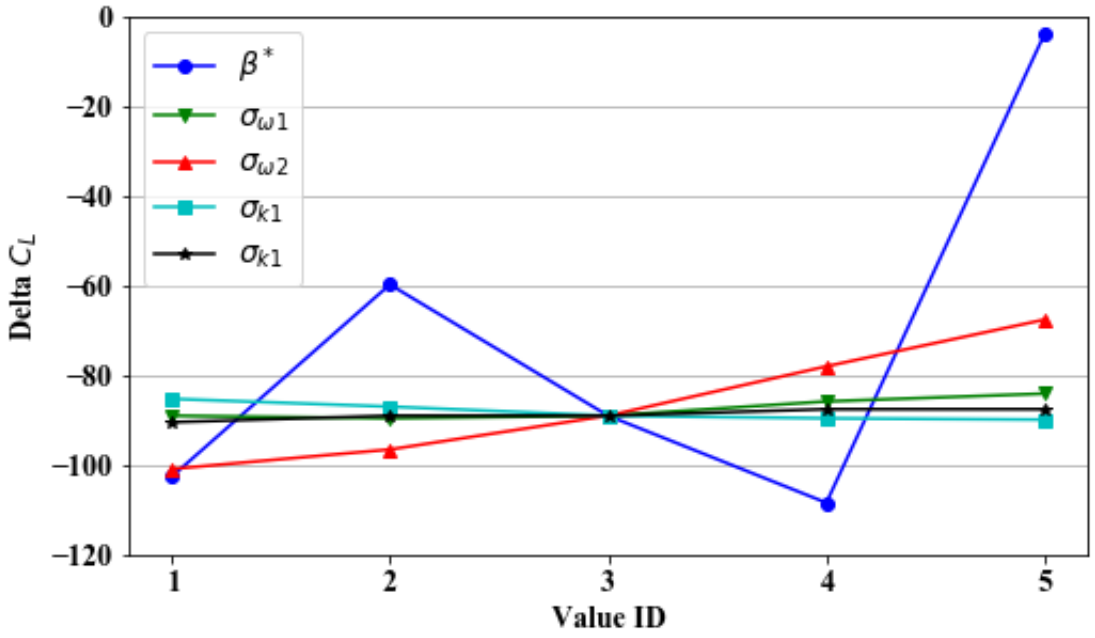

Figure 4.12: Percent relative deviation of the CFD predicted C_L from the experimental value of [4].

Table 4.5: C_D and C_L from current CFD simulation with selected combination of three model coefficients against experimental values

	F1	F2	Expt. [4]
C_D	0.291	0.307	0.299
C_L	0.338	0.358	0.345

can yield improved prediction. Thus, two more cases F1 and F2 were simulated with ($\sigma_{\omega 1} = 0.7$, $\sigma_{\omega 2} = 1.2$, $\beta^* = 0.07$) and ($\sigma_{\omega 1} = 1.0$, $\sigma_{\omega 2} = 1.712$, $\beta^* = 0.07$) respectively. These results are compared with the experimental data of [4] in Table 4.5. Firstly, the increasing trends of C_D and C_L still exist by increasing $\sigma_{\omega 1}$ and $\sigma_{\omega 2}$ up to twice their default values. In addition, combining with $\beta^* = 0.07$, a better correlation with the experiment can be achieved. To further confirm the authors' speculation, one additional case, case F3, was tried with $\sigma_{\omega 1}$ and $\sigma_{\omega 2}$ obtained by linearly interpolating the values used in cases F1 and F2 for the expected drag prediction. This case with ($\sigma_{\omega 1} = 0.85$, $\sigma_{\omega 2} = 1.456$, $\beta^* = 0.07$) predicted a C_D value of 0.298 and a C_L value of 0.358. While the C_L value is still 3.7% higher than the experimental value, the nearly spot-on C_D value is very promising. In the author's opinion, these represent by far the best reported values of CFD predicted drag and lift coefficients for the ever challenging 25 degree slant angle Ahmed body model.

CFD simulations not only need to predict well-correlated drag and lift values, they also should be capable of predicting reasonable flow structures and turbulence quantities, since those are necessary information for better aerodynamic design. Therefore, the three coefficients, i.e. $\sigma_{\omega 1}, \sigma_{\omega 2}$ and β^*, which have pronounced influence on drag and lift predictions, will be further investigated in terms of flow structures and turbulent kinetic energy. In addition, the case with default coefficients and the case F3

(labeled as "Best" in the following figures) will also be analyzed. These 14 cases will be compared with the experimental results by [84]. The Reynolds number used in this study is the same as that used in the experiments [84] which were conducted in a 3/4 open test section with a blockage ratio of 4%.

The streamlines on the central plane through the Ahmed body with 25 degree slant angle are shown in Figure 4.13. Firstly, it can be seen that, only the case F3 successfully predicted a recirculation zone on the slant and similar wake structure as that from the experiment. All other cases, except the case with $\beta^* = 0.13$, predicted a fully separated flow on the slant and thus a much larger wake region. Further, as the drag and lift predictions, the coefficient β^* also has the strongest influence on the wake structure. While lower β^* value led to a larger wake region, higher β^* value ($\beta^* = 0.13$) predicted a fully attached flow on the slant and an unphysical wake structure. Moreover, increasing $\sigma_{\omega 2}$ led to a smaller wake region. In addition, the influence of $\sigma_{\omega 1}$ on wake structure was small.

The turbulent kinetic energy distributions on the central plane of the Ahmed body with 25 degree slant angle are shown in Figure 4.14. Clearly, only the "Best" case predicts similar turbulent kinetic energy distribution as that from the experiment. All other cases predicted noticeably lower turbulent kinetic energy. Further, the case with $\beta^* = 0.13$ predicted an erroneously low turbulent kinetic energy. Again, the influence of $\sigma_{\omega 1}$ was small and increasing $\sigma_{\omega 2}$ led to better prediction.

The streamwise velocity in successive YZ-planes in the wake of the Ahmed body (X = 0 mm, X = 80 mm, X = 200 mm and X = 500 mm) are shown in Figure 4.15 - 4.18. The same conclusion can be reached on the influence of each coefficient. In short, the case F3, which predicts well-correlated drag and lift values, also predicts best flow structures and turbulent kinetic energy distribution. Further, while the case with $\beta^* = 0.13$ leads to unphysical prediction, increasing $\sigma_{\omega 2}$ produces better result.

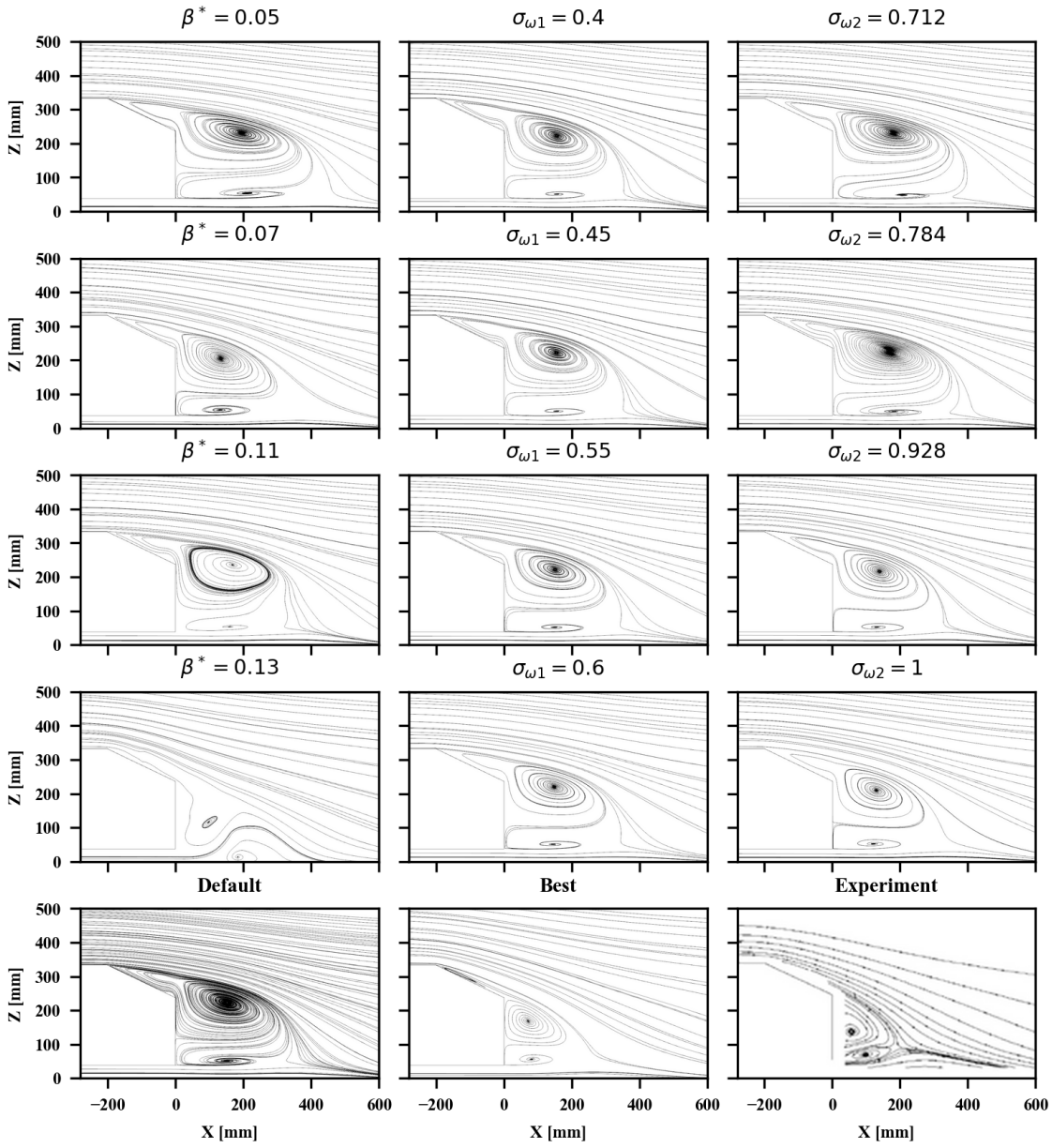

Figure 4.13: Streamlines on the central plane Y = 0 for Ahmed body with 25 degree slant angle.

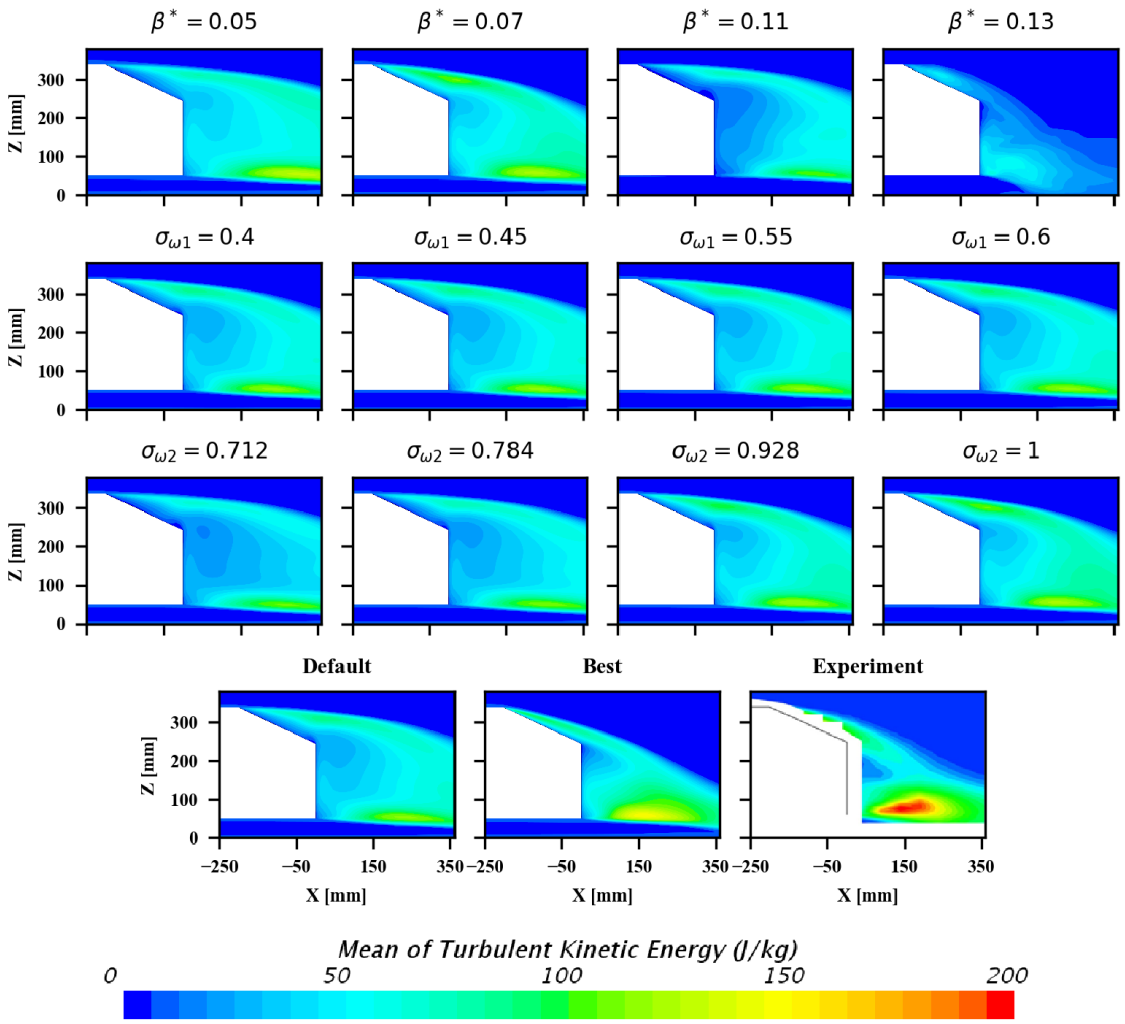

Figure 4.14: Turbulent kinetic energy on the central plane Y = 0 for Ahmed body with 25 degree slant angle.

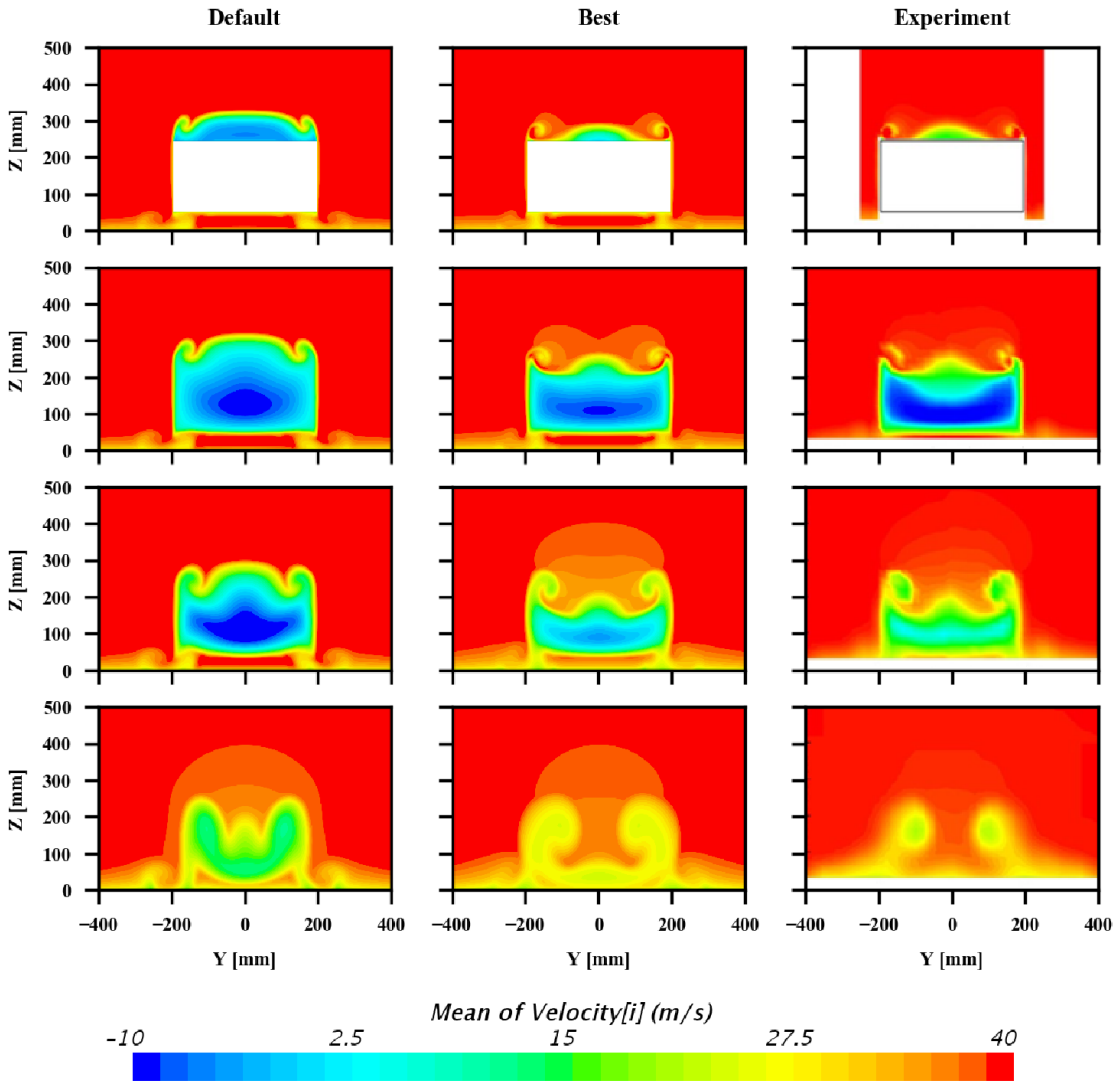

Figure 4.15: The streamwise velocity in successive YZ-planes in the wake of the Ahmed body for the default case, the case F3 and the experiment. From top to bottom, the rows correspond to the location X = 0 mm, X = 80 mm, X = 200 mm and X = 500 mm, respectively.

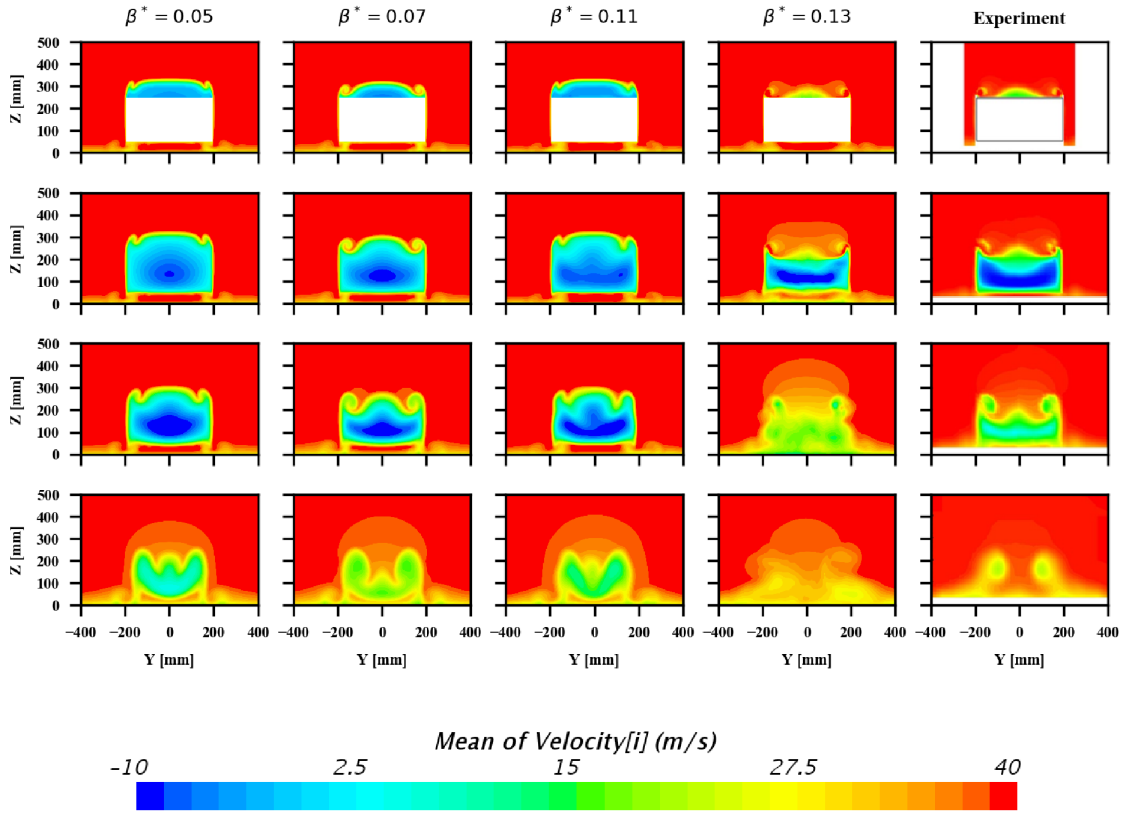

Figure 4.16: The streamwise velocity in successive YZ-planes in the wake of the Ahmed body for the β^* cases and the experiment. From top to bottom, the rows correspond to the location X = 0 mm, X = 80 mm, X = 200 mm and X = 500 mm, respectively.

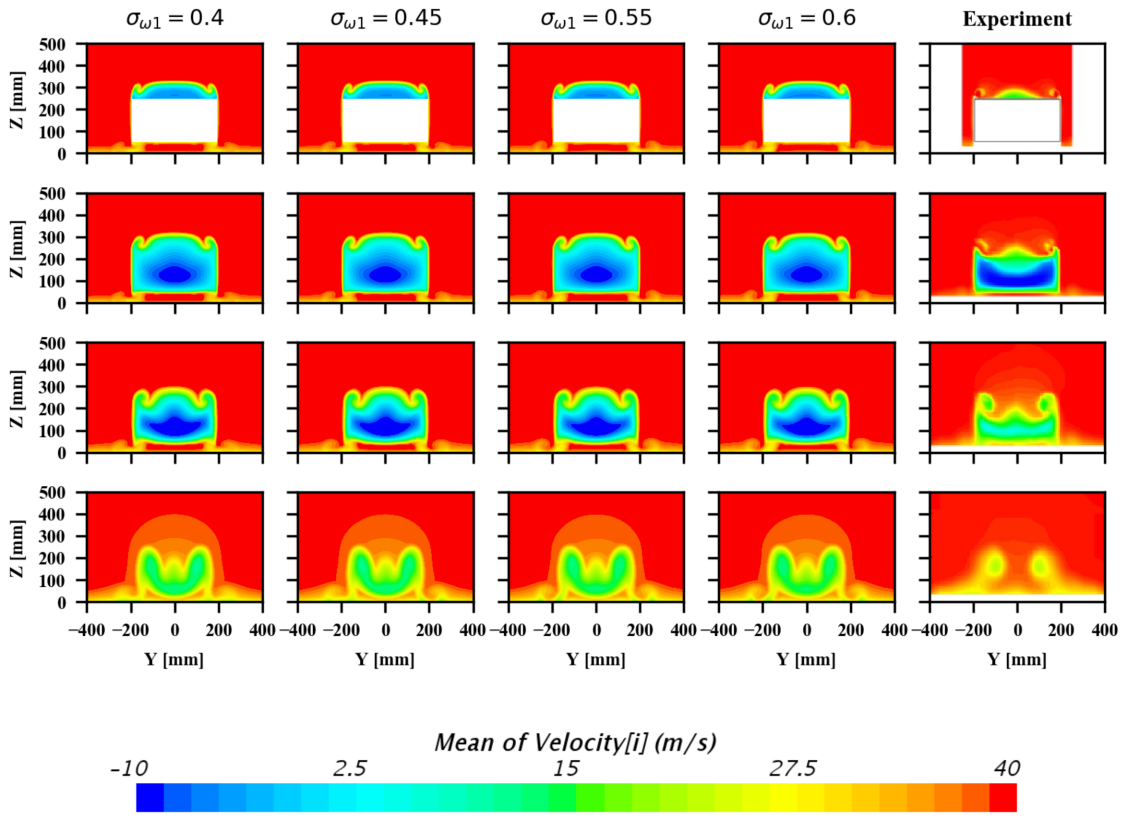

Figure 4.17: The streamwise velocity in successive YZ-planes in the wake of the Ahmed body for the $\sigma_{\omega 1}$ cases and the experiment. From top to bottom, the rows correspond to the location X = 0 mm, X = 80 mm, X = 200 mm and X = 500 mm, respectively.

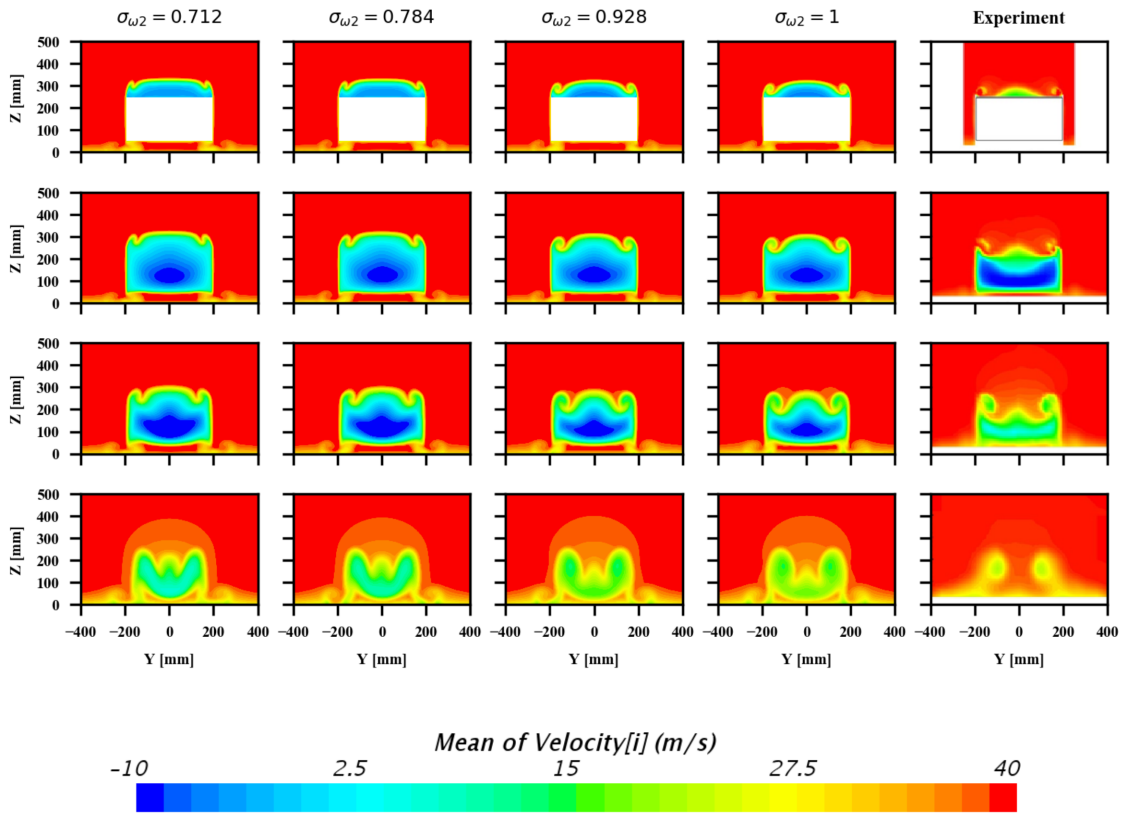

Figure 4.18: The streamwise velocity in successive YZ-planes in the wake of the Ahmed body for the $\sigma_{\omega 2}$ cases and the experiment. From top to bottom, the rows correspond to the location X = 0 mm, X = 80 mm, X = 200 mm and X = 500 mm, respectively.

4.5.3 Full-Scale Real Life Road Vehicle

Due to the proprietary nature of the data, the drag and lift coefficients values for full-scale real-life road vehicle model used in this study are normalized, using an arbitrary reference area. This is done in such a way that the C_D obtained from the experiment matches with the one available in the public domain. Data downloaded from the website Edmunds.com,"features & specs 2014 Hyundai Veloster", https://www.edmunds.com/hyundai/veloster/2014/features-specs/, accessed April 24, 2018, indicates that the drag coefficient of 2014 Hyundai Veloster is 0.320. Note that both the CFD and experimental force coefficient values are normalized.

The normalized C_D and C_L values from all cases are listed in Table 4.6. To better present the C_D data, the delta between the CFD and experimental data, normalized by the experimental data, is also graphically summarized in Figure 4.19; like before this is termed as the "Delta C_D". It can be seen that, compared to the wind tunnel test, the case with default coefficients predicted significantly higher C_D value. Interestingly this trend is different from what was observed in the Ahmed body case, but similar to what was observed with the NACA 4412 airfoil for all angles of attack. For drag prediction, once again, the change of β^* has the strongest influence on the C_D prediction. This is consistent with the observations from the NACA 4412 and Ahmed body cases. In addition, both decreasing σ_{k2} and increasing $\sigma_{\omega1}$ can lead to a noticeable improvement on C_D prediction. However, no clear trend exists by decreasing σ_{k2}. On the other hand, increasing $\sigma_{\omega1}$ may further improve C_D prediction. Since no experimental lift coefficient is available for this car model, the case with the default coefficients was used as the reference to graphically present the delta C_L for all other cases with modified coefficients, as seen in Figure 4.20. It can be seen that, firstly, the only clear trend can be observed is that decreasing σ_{k1} leads to a higher C_L. Once again the change of β^* shows the strongest influence on the lift prediction.

From the above results, it can be seen that for drag prediction, clear trends toward

Table 4.6: CFD predicted C_D and C_L for the real life road vehicle model

Value #	1	2	3	4	5
β^*	0.05	0.07	0.09	0.11	0.13
C_D	0.344	0.346	0.359	0.361	0.357
C_L	0.107	0.12	0.096	0.102	0.088
$\sigma_{\omega 1}$	0.4	0.45	0.5	0.55	0.6
C_D	0.361	0.358	0.359	0.358	0.354
C_L	0.109	0.111	0.096	0.118	0.114
$\sigma_{\omega 2}$	0.712	0.784	0.856	0.928	1
C_D	0.363	0.365	0.359	0.358	0.358
C_L	0.107	0.108	0.096	0.113	0.109
σ_{k1}	0.7	0.775	0.85	0.925	1
C_D	0.359	0.361	0.359	0.363	0.36
C_L	0.104	0.102	0.096	0.112	0.103
σ_{k2}	0.8	0.9	1	1.1	1.2
C_D	0.355	0.355	0.359	0.362	0.361
C_L	0.11	0.109	0.096	0.106	0.102

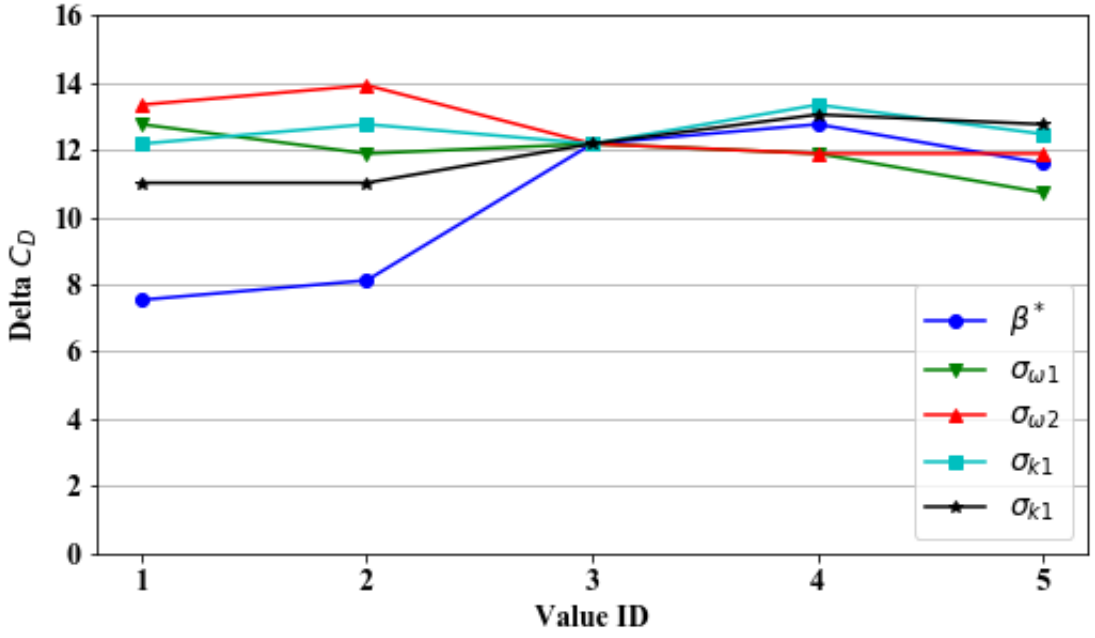

Figure 4.19: Percent relative deviation of the CFD predicted C_D from the experimental value.

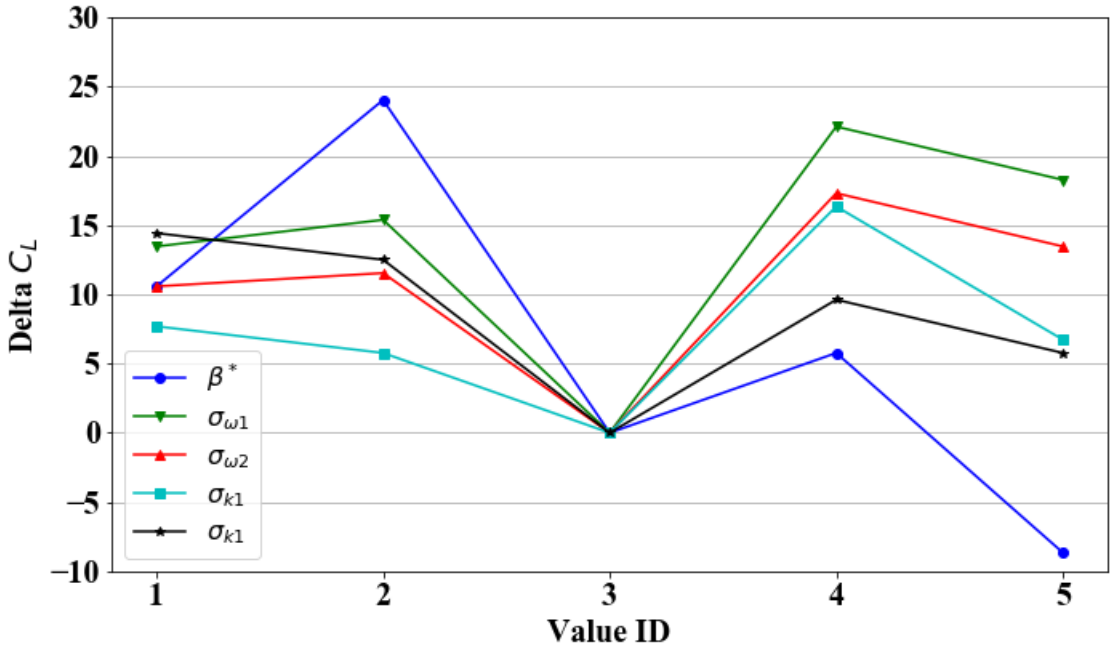

Figure 4.20: Percent relative deviation of the CFD predicted C_L from that of the case with default coefficients

the experimental value exist by both increasing $\sigma_{\omega 1}$ and decreasing β^*. Therefore, the authors speculated that further improvement can be made in predicting the drag value. Considering the nonlinearity in the trend of β^* w.r.t C_D and the very high sensitivity of the prediction to the change of β^*, the authors only increased $\sigma_{\omega 1}$ up to twice of its default value. Thus, two more cases G1 and G2 with ($\sigma_{\omega 1} = 1$, $\beta^* = 0.07$) and ($\sigma_{\omega 1} = 1.0$, $\beta^* = 0.05$) are simulated; when compared to the test data, these two cases show +6.1% and +3.2% prediction errors respectively. Considering that the case with the default values of the model coefficients showed a considerably higher error (+12.2%), this is a promising improvement. However, the authors caution that before deciding on the model closure coefficient combination, the dependences of all force and moment coefficients on the closure coefficient values need to be taken into account. The authors plan to carry out this investigation using the DrivAer model of [85] for which extensive experimental data at different ride-height, yaw and configurations are available.

4.5.4 Ahmed Body with 35 Degree Slant Angle

An additional test case, the Ahmed body with 35 slant angle, was run to provide further verifications. Based on the above results, only two β^* values (0.07 and 0.11) were investigated since further change may lead to undesirable predictions. On the other hands, more values of the coefficients $\sigma_{\omega 1}$ and $\sigma_{\omega 2}$ were analyzed (see Table 4.7). In addition, the coefficients σ_{k1} and σ_{k2} were not investigated due to their negligible influence.

The present study used the same Reynolds number and boundary treatment on the floor as used in [4], therefore the work of [4] will be used as the reference for validation and correlation. The drag and lift force coefficients from the present study, using the default model coefficients, along with the experimental data are presented in Table 4.8. It can be seen that, compared to the experimental data of [4], CFD predicted a 9.3% lower C_D; much worse, the predicted C_L value is negative and significantly

Table 4.7: The values of the coefficients $\sigma_{\omega 1}$ and $\sigma_{\omega 2}$ investigated

Value #	1	2	3	**4**	5	6	7	8
$\sigma_{\omega 1}$ **J**	0.25	0.4	0.45	**0.5**	0.55	0.6	0.75	1.0
$\sigma_{\omega 2}$ **K**	0.428	0.712	0.784	**0.856**	0.928	1.0	1.284	1.712

Table 4.8: C_D and C_L from current CFD simulations with default model coefficients compared against experimental values.

	CFD	Expt. [4]	Difference
C_D	0.253	0.279	-9.3%
C_L	-0.065	0.004	

lower.

The C_D and C_L values from all cases are listed in Table 4.9. Firstly, the two investigated β^* values predict significantly better C_L value but slightly worse C_D value. Secondly, the C_D value generally increases slightly as $\sigma_{\omega 1}$ increases from half of its default value up to twice its default value. Further, changing $\sigma_{\omega 1}$ to either direction regarding to the default value leads to a significantly better C_L prediction, with the case $\sigma_{\omega 1} = 1.0$ predicts best C_L value. Finally, the C_D value increases as $\sigma_{\omega 2}$ increases. However, while the case with $\sigma_{\omega 2} = 1.284$ predicts a well correlated C_L value, the predicted C_D value is significantly higher. In addition, the case with $\sigma_{\omega 2} = 1.712$, which is twice its default value, predicts significantly higher C_D and C_L values.

Table 4.9: Turbulence model closure coefficient sensitivity of drag and lift predictions of Ahmed body with 35 degree slant angle.

Value #	1	2	3	**4**	5	6	7	8
β^*			0.07	**0.09**	0.11			
C_D			0.251	0.253	0.248			
C_L			-0.005	-0.065	-0.008			
$\sigma_{\omega 1}$	0.25	0.4	0.45	**0.5**	0.55	0.6	0.75	1.0
C_D	0.249	0.252	0.253	0.253	0.254	0.255	0.255	0.257
C_L	-0.008	-0.008	-0.008	-0.065	-0.007	-0.007	-0.006	-0.003
$\sigma_{\omega 2}$	0.428	0.712	0.784	**0.856**	0.928	1.0	1.284	1.712
C_D	0.241	0.246	0.25	0.253	0.257	0.264	0.328	0.395
C_L	-0.008	-0.007	-0.007	-0.065	-0.005	-0.004	0.005	0.298

Table 4.10: C_D and C_L from current CFD simulation with selected combination of two model coefficients against experimental values

	M1	Expt. [4]
C_D	0.278	0.279
C_L	-0.011	0.004

Based off the above analysis, one more case, case M1, with the combination of $\sigma_{\omega 1} = 1.0$ and $\sigma_{\omega 2} = 1.1$ was simulation aiming to achieve an improved drag, lift, flow structure and turbulence quantities prediction. The predicted C_D and C_L values from the case M1 are compared with [4] in Table 4.10. It can be seen, while the C_L value is still 15 counts lower than the experimental value, the nearly spot-on C_D value is a pronounced improvement.

Further analysis in terms of flow structures and turbulent kinetic energy was also performed for this test geometry. The results are presented in Figure 4.21 - 4.29. It can be seen that, the case M1, which predicts well-correlated drag and lift values, also predicts best flow structures and turbulent kinetic energy distribution. Further, while the influence of $\sigma_{\omega 1}$ is small, the impact of $\sigma_{\omega 2}$ is rather interesting. Specifically, better predictions can be achieved by increasing $\sigma_{\omega 2}$ up to 1, however, further increasing its values leads to unphysical predictions.

4.5.5 Summary Observations

Three cases associated with automotive flows were investigated to achieve improved drag and lift predictions by tuning several closure coefficients of the SST model. The change of β^* coefficient has a strong influence on the drag and lift predictions. This might be due to the fact that β^* affects some dominating terms in both transport

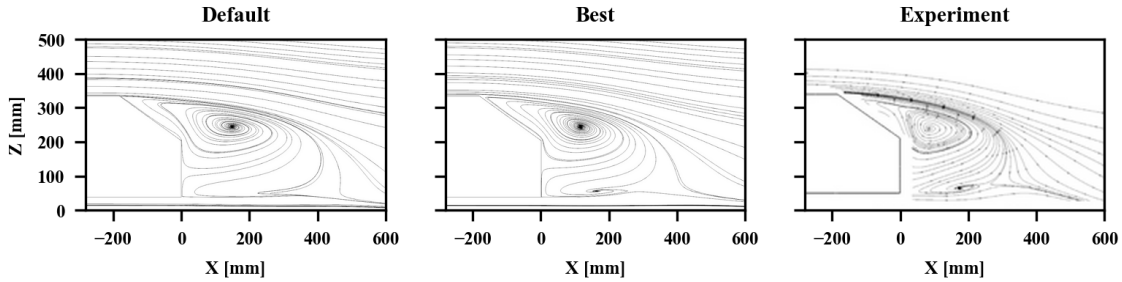

Figure 4.21: Streamlines on the central plane Y = 0 for the default case, the case M1 and the experiment.

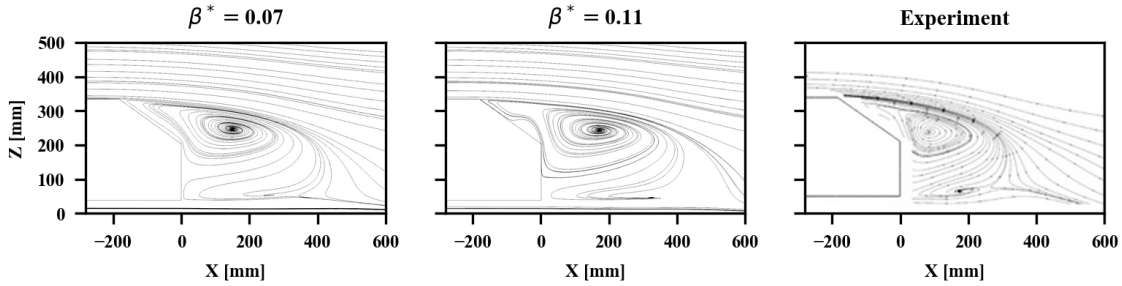

Figure 4.22: Streamlines on the central plane Y = 0 for the β^* cases and the experiment.

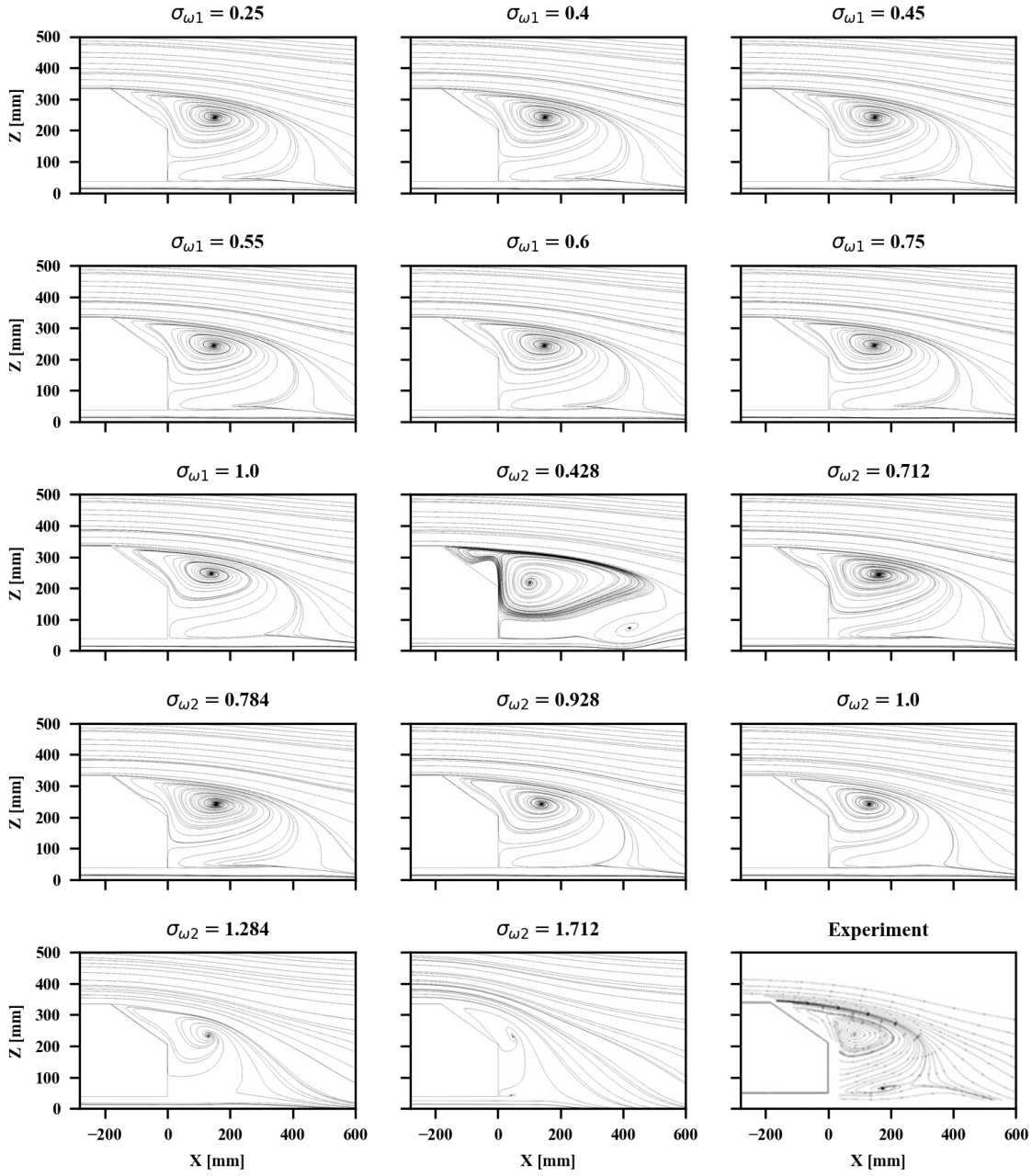

Figure 4.23: Streamlines on the central plane Y = 0 for the $\sigma_{\omega 1}$ and $\sigma_{\omega 2}$ cases and the experiment.

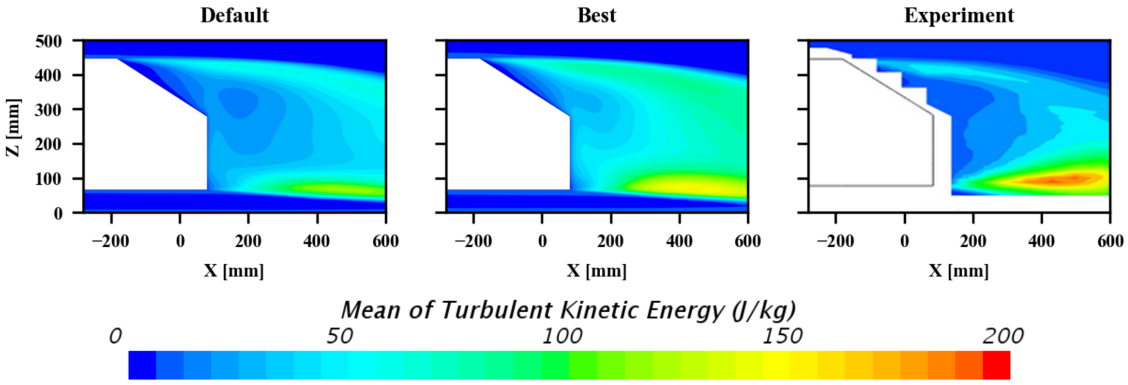

Figure 4.24: Turbulent kinetic energy on the central plane Y = 0 for the default case, the case M1 and the experiment.

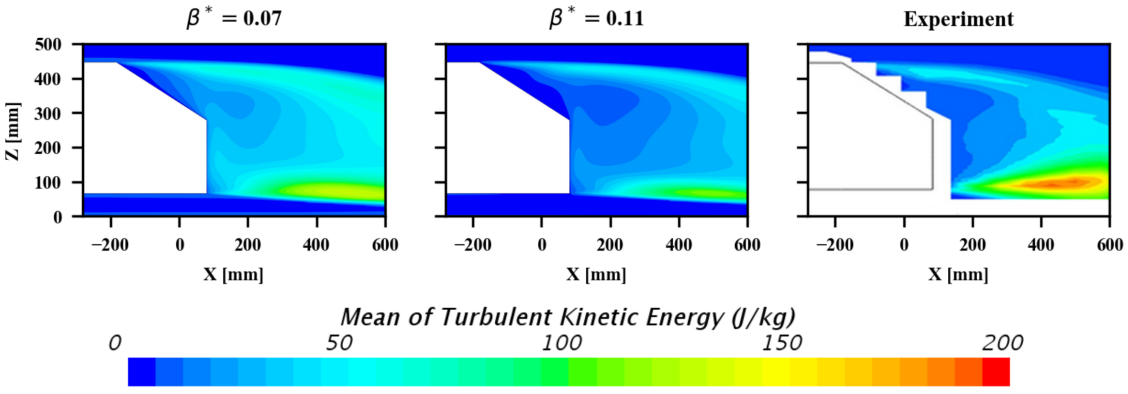

Figure 4.25: Turbulent kinetic energy on the central plane Y = 0 for the β^* cases and the experiment.

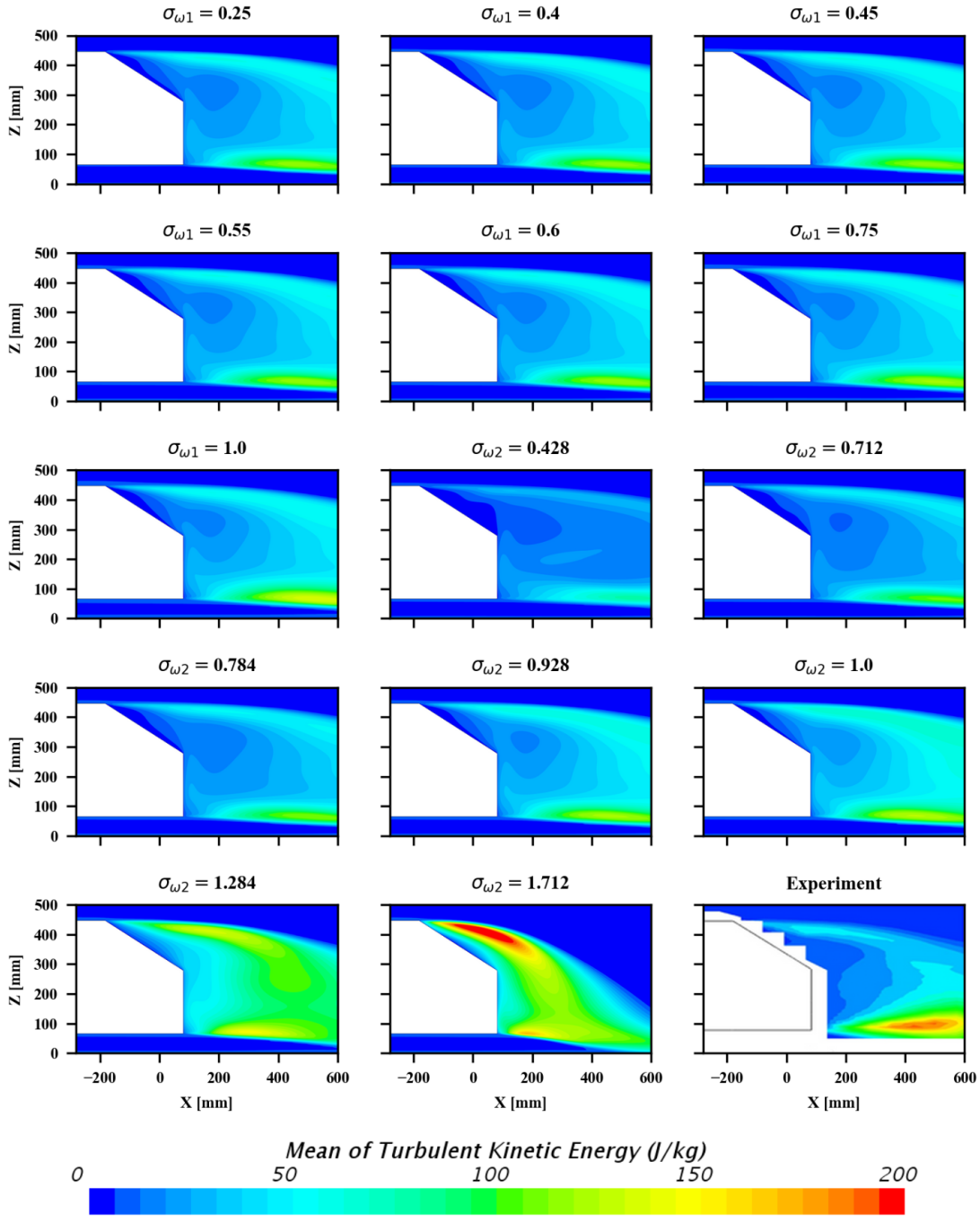

Figure 4.26: Turbulent kinetic energy on the central plane Y = 0 for the $\sigma_{\omega1}$ and $\sigma_{\omega2}$ cases and the experiment.

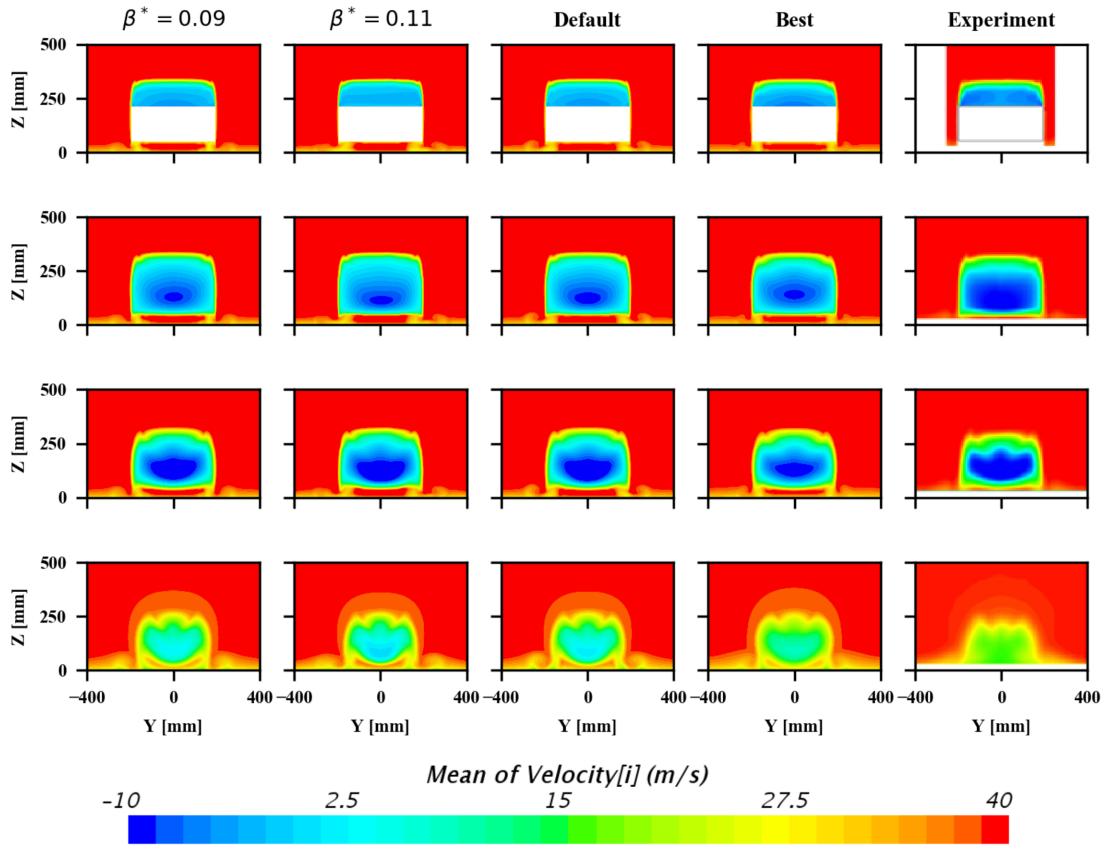

Figure 4.27: The streamwise velocity in successive YZ-planes in the wake of the Ahmed body for the β^* cases, the default case, the case M1 and the experiment. From top to bottom, the rows correspond to the location X = 0 mm, X = 80 mm, X = 200 mm and X = 500 mm, respectively.

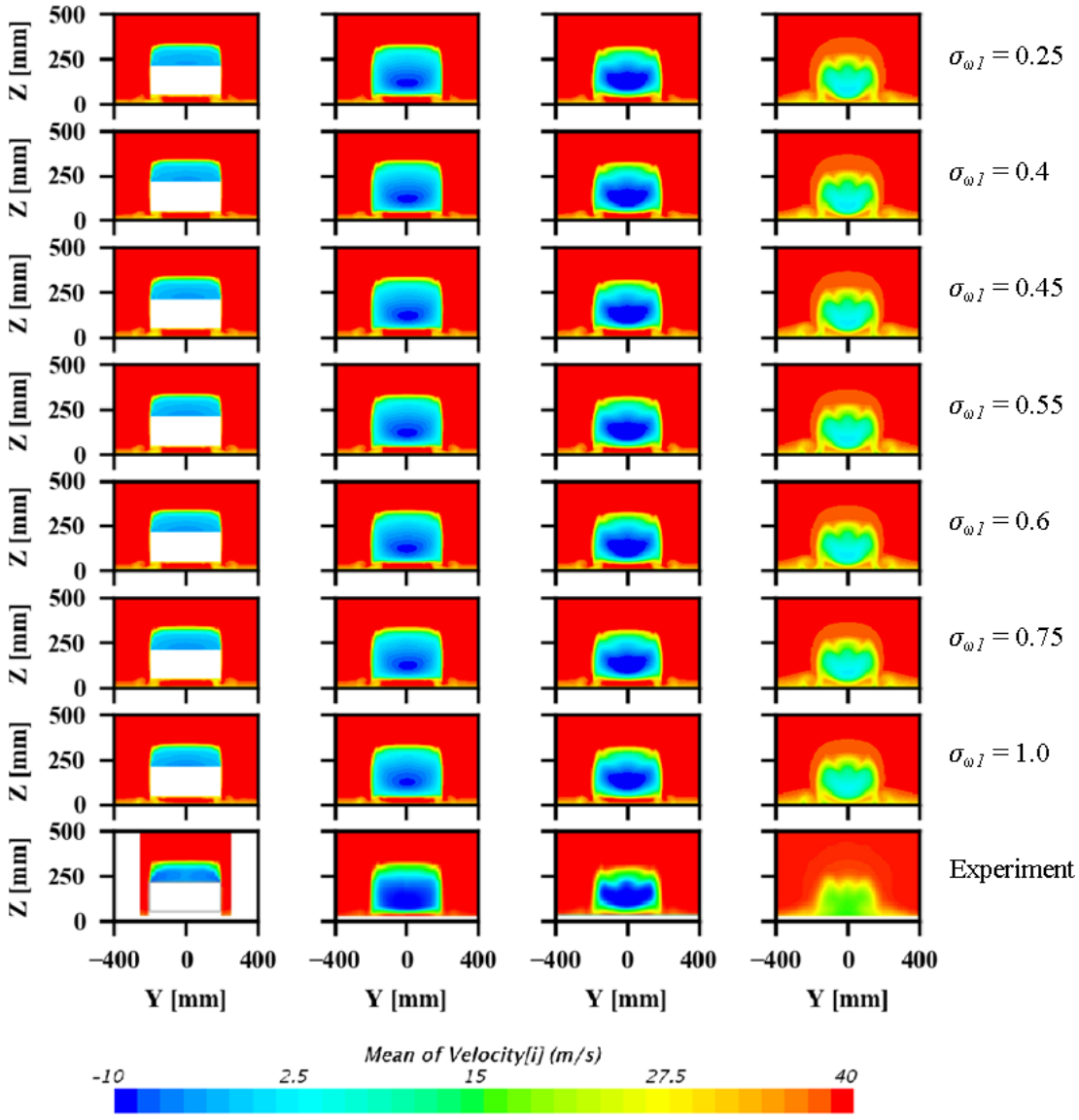

Figure 4.28: The streamwise velocity in successive YZ-planes in the wake of the Ahmed body for the $\sigma_{\omega 1}$ cases and the experiment. From left to right, the columns correspond to the location X = 0 mm, X = 80 mm, X = 200 mm and X = 500 mm, respectively.

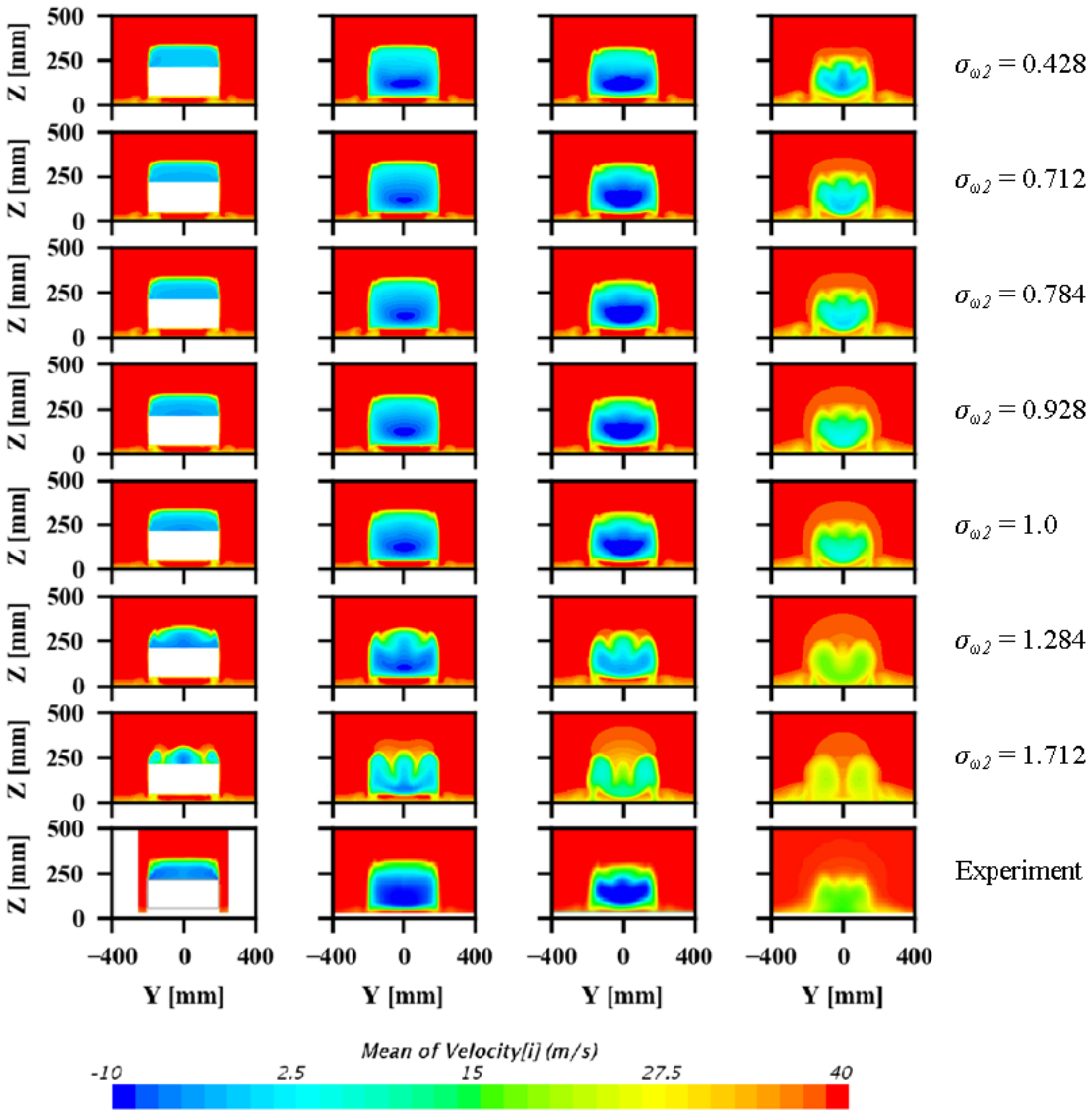

Figure 4.29: The streamwise velocity in successive YZ-planes in the wake of the Ahmed body for the $\sigma_{\omega 2}$ cases and the experiment. From left to right, the columns correspond to the location X = 0 mm, X = 80 mm, X = 200 mm and X = 500 mm, respectively.

equations, e.g. the dissipation term in the k equation ((4.4)), the production term in the ω equation ((4.5), (4.11)), and the F_2 blending function ((4.9)). Similarly, the minor influence of σ_{k1} and σ_{k2} can be explained by the fact that they only affect the diffusion term in the k equation ((4.4)). Further analysis shows that $\sigma_{\omega1}$ and $\sigma_{\omega2}$ affect the diffusion and production term in the ω equation ((4.5), (4.11)). In addition, $\sigma_{\omega2}$ also affects the cross diffusion term in the ω equation ((4.5)). Consequently, on the influence of drag and lift predictions, $\sigma_{\omega1}$ and $\sigma_{\omega2}$ are stronger than σ_{k1} and σ_{k2}, but weaker than β^*.

Considering the complexity of two-equation RANS approaches which are composed of one linear and five non-linear partial differential equations, and the scale-dependent transient nature of turbulence, it is to the authors' surprise that a somewhat linear trend toward better prediction of drag and lift values for the Ahmed body and the full-scale vehicle model used in this study exists by increasing $\sigma_{\omega1}$ or $\sigma_{\omega2}$.

4.6 CONCLUSION

Based on the results presented in this paper, the main findings are:

1. The closure coefficient β^* has a strong influence on the prediction of drag, lift and the flow field.

2. For the streamlined NACA 4412 airfoil, even at a high angle of attack, the influence of closure coefficients $\sigma_{\omega1}, \sigma_{\omega2}, \sigma_{k1}$ and σ_{k2} are quite small on the prediction of drag and lift.

3. The influences of closure coefficients σ_{k1} and σ_{k2} are quite small.

4. A somewhat linear trend toward better prediction of drag and lift exists for the two Ahmed bodies and the real-life road vehicle models by increasing $\sigma_{\omega1}$ or $\sigma_{\omega2}$ from the respective default values.

5. In addition to increasing $\sigma_{\omega1}$ and $\sigma_{\omega2}$, a very good correlation with the exper-

imental drag data can be achieved for the Ahmed body with 25 degree slant angle and the real-life road vehicles by combining a smaller than the default value for β^*.

The main motivation of this study is that the coefficients of the SST model were mainly calibrated using some simple canonical flows. Thus, those coefficients might not work well for complex automotive flows. The authors acknowledge that three cases are far from enough to make a decisive conclusion. However, the results obtained in this study are quite promising for improving drag and lift predictions associated with automotive flows by tuning some of the coefficients of the SST model. The authors acknowledge that more cases are needed to be investigated in order to make a more decisive conclusion. Based on the results obtained in this study, the authors will continue to investigate more cases such as various DrivAer configurations with a focus on β^*, $\sigma_{\omega 1}$ and $\sigma_{\omega 2}$.

CHAPTER 5: CONCLUSION

The main goal of this dissertation is to provide more knowledge for CFD simulation of road vehicle aerodynamics. It was found that CFD can be a cost-effect tool for not only external aerodynamics, but also underhood airflow management which is very complex and crowded. Moreover, by evaluating some most commonly used turbulence models, it was found that the success of CFD simulation still heavily relies on the choice of mesh strategy and turbulent models which in turn depend on the experience of engineers. RANS models might be still a good choice for the prediction of drag values due to their acceptable accuracy, low computational cost and fast turnaround time. However, for applications require predictions of detail flow features, such as aeroacoustic, soiling and water management, the transient DES type approaches would be a better choice. Further, for the SST $k-\omega$ model, the author obtained promising results for improving drag and lift predictions associated with automotive flows by tuning some of its closure coefficients. More detailed conclusions are:

Firstly, it has been shown that a vertical CRFM for the investigated car configuration has a poor radiator performance and high cooling drag. However, we have demonstrated that the underhood airflow can be optimized by introducing an air-duct, in combination with an altered orientation of the CRFM and modified grille openings. This configuration results in a superior performance at both highway speeds and idle conditions. Specifically, at highway speed, an air-duct design can improve the cooling performance of the radiator by increasing the flow rate and airflow uniformity over the upstream surface. In addition, a wider air-duct performs better than a narrow one under this condition. At vehicle idle condition, the air-duct can attenuate the

hot-air recirculation problem significantly, which could result in a notable improvement of heat exchanger performance, primarily that of the condenser. Moreover, the air-duct design also can reduce the cooling drag, hence the total vehicle drag, due to significantly lesser airflow entering the underhood area. Further, by reducing the excessive airflow that does not contribute to the cooling purpose, the sealed-off side-grilles could reduce the cooling drag even more. Consequently, a combination of side-grille sealing with a wide air-duct can achieve a notable improvement of the underhood airflow management, in terms of both the radiator performance and vehicle total drag, and, thus, will improve the overall fuel economy. However, we have recognized that the cold-flow based CFD simulations can be inconclusive for radiator performance as some designs can show an increase in volume flow rate, but a decrease in flow uniformity and vice versa implying that aerodynamic analysis with heat transfer needs to be carried out before making the final design call.

Further, the author presents a numerical evaluation of various commonly used RANS models and Hybrid RANS/LES models on a full-scale passenger vehicle with two different front-end configurations. The effect of turbulence modeling on the prediction of drag and lift forces, pressure and velocity field, and turbulent kinetic energy were investigated. It was found that, firstly, the RKE model predicted well correlated C_D value for the baseline case, however, all the models investigated still need significant improvement in order to predict the lift values consistently; secondly, despite DES variants not showing superior performance over RANS models for predicting absolute C_D value, they were able to predict more complex flow structures, such as in Figure 3.14 the DDES model predicts a tertiary vortex near the exhaust pipes and the IDDES model predicts a tertiary vortex under the spoiler. Further, the two DES variants are still expected to predict better large scale flow features due to that they are capable of resolving large scale flow features directly. The similarity of the streamwise velocity profile and turbulent kinetic energy distribution on the selected planes

between the predictions from the RKE model and the DES variants supports that the RKE model performs better than the other three RANS models for the baseline case.

Finally, for the fine-tuning of the SST $k-\omega$ model closure coefficients, the main findings are:

1. The closure coefficient β^* has a strong influence on the prediction of drag, lift and the flow field.

2. For the streamlined NACA 4412 airfoil, even at a high angle of attack, the influence of closure coefficients $\sigma_{\omega 1}, \sigma_{\omega 2}, \sigma_{k1}$ and σ_{k2} are quite small on the prediction of drag and lift.

3. The influences of closure coefficients σ_{k1} and σ_{k2} are quite small.

4. A somewhat linear trend toward better prediction of drag and lift exists for the two Ahmed bodies and the real-life road vehicle models by increasing $\sigma_{\omega 1}$ or $\sigma_{\omega 2}$ from the respective default values.

5. In addition to increasing $\sigma_{\omega 1}$ and $\sigma_{\omega 2}$, a very good correlation with the experimental drag data can be achieved for the Ahmed body with 25 degree slant angle and the real-life road vehicles by combining a smaller than the default value for β^*.

REFERENCES

[1] "2016 mercedes glc wind tunnel testing unveiled press images." https://indianautosblog.com/2015/06/mercedes-glc-unveiled-181666/2016-mercedes-glc-wind-tunnel-testing-unveiled-press-images, 2015. Accessed: 2018-07-01.

[2] C. Argyropoulos and N. Markatos, "Recent advances on the numerical modelling of turbulent flows," *Applied Mathematical Modelling*, vol. 39, no. 2, pp. 693 – 732, 2015.

[3] I. H. Abbott and A. E. Von Doenhoff, *Theory of wing sections, including a summary of airfoil data*. Courier Corporation, 1959.

[4] W. Meile, G. Brenn, A. Reppenhagen, and A. Fuchs, "Experiments and numerical simulations on the aerodynamics of the ahmed body," *CFD letters*, vol. 3, no. 1, pp. 32–39, 2011.

[5] R. Littlewood, *Novel methods of drag reduction for squareback road vehicles*. PhD thesis, © Rob Littlewood, 2013.

[6] S. R. Sawyer, *Experimental investigation of drag reduction by trailing edge tabs on a square based bluff body in ground effect*. PhD thesis, California Polytechnic State University, San Luis Obispo, 2015.

[7] A. Altaf, A. A. Omar, and W. Asrar, "Review of passive drag reduction techniques for bluff road vehicles," *IIUM Engineering Journal*, vol. 15, no. 1, 2014.

[8] J. Patten, B. McAuliffe, W. Mayda, and B. Tanguay, "Review of aerodynamic drag reduction devices for heavy trucks and buses," *NRC-CNRC Technical Report*, p. 3, 2012.

[9] X. Song, R. Fortier, and S. Sarnia, "Underhood air duct design to improve a/c system performance by minimizing hot air recirculation," *SAE International Journal of Passenger Cars-Mechanical Systems*, vol. 8, no. 1, pp. 338–345, 2015.

[10] A. Alajbegovic, B. Xu, A. Konstantinov, J. Amodeo, and W. Jansen, "Simulation of cooling airflow under different driving conditions," tech. rep., SAE Technical Paper, 2007.

[11] T. Kubokura, T. Uno, N. Evans, H. Kuroda, F. Shindo, and S. Nagahama, "Study of cooling drag reduction method by controlling cooling flow," tech. rep., SAE Technical Paper, 2014.

[12] G. D. Mathur, "Performance enhancement of mobile air conditioning system with improved air management for front end," tech. rep., SAE Technical Paper, 2005.

[13] S. Saab, J.-F. Hetet, A. Maiboom, and F. Charbonnelle, "Impact of the underhood opening area on the drag coefficient and the thermal performance of a vehicle," tech. rep., SAE Technical Paper, 2013.

[14] M. T. Landahl, M. Landahl, and E. Mollo-Christensen, *Turbulence and random processes in fluid mechanics*. Cambridge University Press, 1992.

[15] H. Tennekes, J. L. Lumley, J. Lumley, *et al.*, *A first course in turbulence*. MIT press, 1972.

[16] B. E. Launder and N. D. Sandham, *Closure strategies for turbulent and transitional flows*. Cambridge University Press, 2002.

[17] M. Lee and R. D. Moser, "Direct numerical simulation of turbulent channel flow up to $re_\tau \approx 5200$," *Journal of Fluid Mechanics*, vol. 774, pp. 395–415, 2015.

[18] D. C. Wilcox *et al.*, *Turbulence Modeling for CFD, third ed.*, vol. 2. DCW industries La Canada, CA, 2006.

[19] N. Markatos, "The mathematical modelling of turbulent flows," *Applied Mathematical Modelling*, vol. 10, no. 3, pp. 190–220, 1986.

[20] P. R. Spalart, "Comments on the feasibility of les for wings, and on a hybrid rans/les approach," in *Proceedings of first AFOSR international conference on DNS/LES*, Greyden Press, 1997.

[21] T.-H. Shih, W. W. Liou, A. Shabbir, Z. Yang, and J. Zhu, "A new k-e eddy viscosity model for high reynolds number turbulent flows," *Computers & Fluids*, vol. 24, no. 3, pp. 227–238, 1995.

[22] K. Abe, T. Kondoh, and Y. Nagano, "A new turbulence model for predicting fluid flow and heat transfer in separating and reattaching flows—i. flow field calculations," *International journal of heat and mass transfer*, vol. 37, no. 1, pp. 139–151, 1994.

[23] P. A. Durbin, "Near-wall turbulence closure modeling without "damping functions"," *Theoretical and Computational Fluid Dynamics*, vol. 3, no. 1, pp. 1–13, 1991.

[24] F. R. Menter, "Two-equation eddy-viscosity turbulence models for engineering applications," *AIAA journal*, vol. 32, no. 8, pp. 1598–1605, 1994.

[25] F. R. Menter, "Review of the shear-stress transport turbulence model experience from an industrial perspective," *International Journal of Computational Fluid Dynamics*, vol. 23, no. 4, pp. 305–316, 2009.

[26] F. R. Menter and M. Kuntz, "Adaptation of eddy-viscosity turbulence models to unsteady separated flow behind vehicles," in *The Aerodynamics of Heavy Vehicles: Trucks, Buses, and Trains* (R. McCallen, F. Browand, and J. Ross, eds.), (Berlin, Heidelberg), pp. 339–352, Springer Berlin Heidelberg, 2004.

[27] M. L. Shur, P. R. Spalart, M. K. Strelets, and A. K. Travin, "A hybrid rans-les approach with delayed-des and wall-modelled les capabilities," *International Journal of Heat and Fluid Flow*, vol. 29, no. 6, pp. 1638 – 1649, 2008.

[28] P. Durbin, "On the $k-\epsilon$ stagnation point anomaly," *International journal of heat and fluid flow*, vol. 17, no. 1, pp. 89–90, 1996.

[29] B. E. Launder and M. Kato, "Modeling flow-induced oscillations in turbulent flow around a square cylinder," in *ASME Fluid Eng. Conference*, vol. 20, 1993.

[30] M. Wolfshtein, "The velocity and temperature distribution in one-dimensional flow with turbulence augmentation and pressure gradient," *International Journal of Heat and Mass Transfer*, vol. 12, no. 3, pp. 301–318, 1969.

[31] L. Davidson, P. V. Nielsen, and A. Sveningsson, "Modifications of the v2 model for computing the flow in a 3d wall jet," *Modifications of the Model for Computing the Flow in a 3D Wall Jet*, 2003.

[32] D. C. Wilcox, "Reassessment of the scale-determining equation for advanced turbulence models," *AIAA journal*, vol. 26, no. 11, pp. 1299–1310, 1988.

[33] D. C. Wilcox, "Formulation of the kw turbulence model revisited," *AIAA journal*, vol. 46, no. 11, pp. 2823–2838, 2008.

[34] W. Jones and B. Launder, "The prediction of laminarization with a two-equation model of turbulence," *International journal of heat and mass transfer*, vol. 15, no. 2, pp. 301–314, 1972.

[35] B. Launder and B. Sharma, "Application of the energy-dissipation model of turbulence to the calculation of flow near a spinning disc," *Letters in heat and mass transfer*, vol. 1, no. 2, pp. 131–137, 1974.

[36] W. Rodi, "Experience with two-layer models combining the k-epsilon model with a one-equation model near the wall," in *29th Aerospace sciences meeting*, p. 216, 1991.

[37] C. Zhang, M. Uddin, A. C. Robinson, and L. Foster, "Full vehicle cfd investigations on the influence of front-end configuration on radiator performance and cooling drag," *Applied Thermal Engineering*, vol. 130, pp. 1328–1340, 2018.

[38] R. Barnard, "Theoretical and experimental investigation of the aerodynamic drag due to automotive cooling systems," *Proceedings of the Institution of Mechanical Engineers, Part D: Journal of Automobile Engineering*, vol. 214, no. 8, pp. 919–927, 2000.

[39] F. Chometon and P. Gilliéron, "Assessment of engine cooling performance by measurement of cooling airflow drag in aerodynamic wind tunnels," tech. rep., SAE Technical Paper, 1998.

[40] P. Gilliéron and F. Chometon, "Reduction of cooling air drag of road vehicles: an analytical approach," tech. rep., SAE Technical Paper, 2001.

[41] T. Ivanić and P. Gilliéron, "Reduction of the aerodynamic drag due to cooling systems: an analytical and experimental approach," tech. rep., SAE Technical Paper, 2005.

[42] G. Tesch, R. Demuth, and N. Adams, "A new approach to analyzing cooling and interference drag," *SAE International Journal of Passenger Cars-Mechanical Systems*, vol. 3, no. 1, pp. 339–351, 2010.

[43] J. Williams, D. Karanth, and W. Oler, "Cooling inlet aerodynamic performance and system resistance," tech. rep., SAE Technical Paper, 2002.

[44] J. Williams, "Aerodynamic drag of engine-cooling airflow with external interference," *SAE transactions*, vol. 112, no. 6, pp. 1092–1102, 2003.

[45] G. Wickern, A. Wagner, and C. Zoerner, "Cooling drag of ground vehicles and its interaction with ground simulation," tech. rep., SAE Technical Paper, 2006.

[46] D. Baeder, T. Indinger, N. Adams, and P. Unterlechner, "Aerodynamic investigation of vehicle cooling-drag," tech. rep., SAE Technical Paper, 2012.

[47] L. Christoffersen, L. Löfdahl, and A. Jönson, "Interference between engine bay flow and external aerodynamics of road vehicles," tech. rep., SAE Technical Paper, 2010.

[48] M. D'Hondt, P. Gilliéron, and P. Devinant, "Aerodynamic drag and flow rate through engine compartments of motor vehicles," in *28th AIAA Applied Aerodynamics Conference*, vol. 28, 2010.

[49] T. Kuthada and J. Wiedemann, "Investigations in a cooling air flow system under the influence of road simulation," tech. rep., SAE Technical Paper, 2008.

[50] F. Wittmeier and T. Kuthada, "Open grille drivaer model-first results," *SAE International Journal of Passenger Cars-Mechanical Systems*, vol. 8, no. 1, pp. 252–260, 2015.

[51] S. Manna and Y. S. Kushwah, "Optimization of a vehicle under hood airflow using 3d cfd analysis," tech. rep., SAE Technical Paper, 2015.

[52] K. Jahani and S. Beigmoradi, "Under-hood air flow evaluation of pedestrian-friendly front-end style using cfd simulation," *SAE International Journal of Passenger Cars-Mechanical Systems*, vol. 7, no. 2, pp. 787–792, 2014.

[53] F. Regin, "A numerical analysis on air-cooling performance of passenger cars," tech. rep., SAE Technical Paper, 2010.

[54] M. Khaled, F. Harambat, and H. Peerhossaini, "Temperature and heat flux behavior of complex flows in car underhood compartment," *Heat Transfer Engineering*, vol. 31, no. 13, pp. 1057–1067, 2010.

[55] M. Khaled, F. Harambat, and H. Peerhossaini, "Towards the control of car underhood thermal conditions," *Applied Thermal Engineering*, vol. 31, no. 5, pp. 902–910, 2011.

[56] M. Khaled, F. Harambat, and H. Peerhossaini, "Underhood thermal management: temperature and heat flux measurements and physical analysis," *Applied Thermal Engineering*, vol. 30, no. 6, pp. 590–598, 2010.

[57] M. Khaled, M. Ramadan, H. El-Hage, A. Elmarakbi, F. Harambat, and H. Peerhossaini, "Review of underhood aerothermal management: Towards vehicle simplified models," *Applied Thermal Engineering*, vol. 73, no. 1, pp. 842–858, 2014.

[58] S. Mao, Z. Feng, and E. Michaelides, "Off-highway heavy-duty truck under-hood thermal analysis," *Applied Thermal Engineering*, vol. 30, no. 13, pp. 1726–1733, 2010.

[59] H. J. Kim and C.-J. Kim, "A numerical analysis for the cooling module related to automobile air-conditioning system," *Applied Thermal Engineering*, vol. 28, no. 14, pp. 1896–1905, 2008.

[60] N. Ashton and A. Revell, "Comparison of rans and des methods for the drivaer automotive body," tech. rep., SAE Technical Paper, 2015.

[61] N. Ashton, A. West, S. Lardeau, and A. Revell, "Assessment of rans and des methods for realistic automotive models," *Computers & Fluids*, vol. 128, pp. 1–15, 2016.

[62] E. Guilmineau, G. Deng, A. Leroyer, P. Queutey, M. Visonneau, and J. Wackers, "Assessment of hybrid rans-les formulations for flow simulation around the ahmed body," *Computers & Fluids*, 2017.

[63] M. Shur, P. Spalart, M. Strelets, and A. Travin, "Detached-eddy simulation of an airfoil at high angle of attack," in *Engineering Turbulence Modelling and Experiments 4*, pp. 669–678, Elsevier, 1999.

[64] P. R. Spalart and C. Streett, "Young-person's guide to detached-eddy simulation grids," 2001.

[65] P. R. Spalart, S. Deck, M. L. Shur, K. D. Squires, M. K. Strelets, and A. Travin, "A new version of detached-eddy simulation, resistant to ambiguous grid densities," *Theoretical and computational fluid dynamics*, vol. 20, no. 3, p. 181, 2006.

[66] S. Ahmed, G. Ramm, and G. Faltin, "Some salient features of the time-averaged ground vehicle wake," tech. rep., SAE Technical Paper, 1984.

[67] T. Han, "Computational analysis of three-dimensional turbulent flow around a bluff body in ground proximity," *AIAA journal*, vol. 27, no. 9, pp. 1213–1219, 1989.

[68] P. Gilliéron and F. Chometon, "Modelling of stationary three-dimensional separated air flows around an ahmed reference model," in *ESAIM: Proceedings*, vol. 7, pp. 173–182, EDP Sciences, 1999.

[69] E. Guilmineau, "Computational study of flow around a simplified car body," *Journal of wind engineering and industrial aerodynamics*, vol. 96, no. 6, pp. 1207–1217, 2008.

[70] N. Ashton and A. Revell, "Key factors in the use of ddes for the flow around a simplified car," *International Journal of Heat and Fluid Flow*, vol. 54, pp. 236–249, 2015.

[71] S. Krajnović and L. Davidson, "Large-eddy simulation of the flow around simplified car model," tech. rep., SAE Technical Paper, 2004.

[72] M. Minguez, R. Pasquetti, and E. Serre, "High-order large-eddy simulation of flow over the "ahmed body" car model," *Physics of fluids*, vol. 20, no. 9, p. 095101, 2008.

[73] A. I. Heft, T. Indinger, and N. A. Adams, "Introduction of a new realistic generic car model for aerodynamic investigations," tech. rep., SAE Technical Paper, 2012.

[74] A. Heft, T. Indinger, and N. Adams, "Investigation of unsteady flow structures in the wake of a realistic generic car model," in *29th AIAA Applied Aerodynamics Conference*, p. 3669, 2011.

[75] A. I. Heft, T. Indinger, and N. A. Adams, "Experimental and numerical investigation of the drivaer model," in *ASME 2012 Fluids Engineering Division Summer Meeting collocated with the ASME 2012 Heat Transfer Summer Conference and the ASME 2012 10th International Conference on Nanochannels, Microchannels, and Minichannels*, pp. 41–51, American Society of Mechanical Engineers, 2012.

[76] B. C. Peters, M. Uddin, J. Bain, A. Curley, and M. Henry, "Simulating drivaer with structured finite difference overset grids," tech. rep., SAE Technical Paper, 2015.

[77] E. Guilmineau, "Numerical simulations of flow around a realistic generic car model," *SAE International Journal of Passenger Cars-Mechanical Systems*, vol. 7, no. 2014-01-0607, pp. 646–653, 2014.

[78] S. Jakirlic, L. Kutej, B. Basara, and C. Tropea, "Computational study of the aerodynamics of a realistic car model by means of rans and hybrid rans/les approaches," *SAE International Journal of Passenger Cars-Mechanical Systems*, vol. 7, no. 2014-01-0594, pp. 559–574, 2014.

[79] C. Fu, M. Uddin, C. Robinson, A. Guzman, and D. Bailey, "Turbulence models and model closure coefficients sensitivity of nascar racecar rans cfd aerodynamic predictions," *SAE International Journal of Passenger Cars-Mechanical Systems*, vol. 10, no. 2017-01-1547, pp. 330–344, 2017.

[80] C. Zhang, M. Uddin, X. Song, C. Fu, and L. Foster, "Simultaneous improvement of vehicle under-hood airflow and cooling drag using 3d cfd simulation," in *SAE 2016 World Congress and Exhibition*, SAE International, apr 2016.

[81] R. Howard and M. Pourquie, "Large eddy simulation of an ahmed reference model," *Journal of Turbulence*, vol. 3, no. 012, pp. 1–18, 2002.

[82] F. Menter, "Zonal two equation kw turbulence models for aerodynamic flows," in *23rd fluid dynamics, plasmadynamics, and lasers conference*, p. 2906, 1993.

[83] F. R. Menter, M. Kuntz, and R. Langtry, "Ten years of industrial experience with the sst turbulence model," *Turbulence, heat and mass transfer*, vol. 4, no. 1, pp. 625–632, 2003.

[84] H. Lienhart and S. Becker, "Flow and turbulence structure in the wake of a simplified car model," tech. rep., SAE Technical Paper, 2003.

[85] A. I. Heft, T. Indinger, and N. A. Adams, "Experimental and numerical investigation of the drivaer model," in *ASME 2012 Fluids Engineering Division Summer Meeting collocated with the ASME 2012 Heat Transfer Summer Conference and the ASME 2012 10th International Conference on Nanochannels, Microchannels, and Minichannels*, pp. 41–51, American Society of Mechanical Engineers, 2012.